A low-noise front-end for an X-band particle deflector at DESY

Vom Promotionsausschuss der
Technischen Universität Hamburg
zur Erlangung des akademischen Grades
Doktor-Ingenieur (Dr.-Ing.)
genehmigte Dissertation

von
Matthias Reukauff

aus
Elmshorn

2022

Gutachter : Prof. Dr.-Ing. A. Jacob
Prof. Dr. H. Werner
Dr. F. Ludwig

Vorsitzender des Prüfungsausschusses : Prof. Dr.-Ing. G. Fey

Tag der mündlichen Prüfung : 03.03.2022

DOI : 10.15480/882.4402
ORCID : 0000-0002-5189-3908

Acknowledgement

This work would not have been possible without the support of all the people I have been working with and I want to take this opportunity to thank all of them. First of all, I want to thank Prof. Dr.-Ing. A. Jacob for allowing me to work on this very challenging topic at DESY and for the trust he put into my abilities.

I also want to thank my supervisor Dr. M. Hoffmann and mentor Dr. F. Ludwig for all the support they gave me during my work at DESY. Without them I would not have been able to finish my work. Also, I want to thank Dr. H. Schlarb for giving me the opportunity to work on this topic. Additionally, I am grateful for all the support my colleagues at DESY have given me during my work. These are namely: L. Springer, U. Mavric, S. Pfeiffer, H. Pryschelski, B. Marchetti, R. D'Arcy, J. Branlard, M. Fenner, S. Jablonski, D. Kühn, A. Rosner, C. Schmidt, B. Szczepanski, J. Szymanski, R. Wedel as well as the other colleagues from the MIN-group and the PolariX team.

Finally, I want to thank my family and especially my parents, who supported me all the way to the finish of my Ph.D. with great understanding and patience.

Abbreviations

AC	Alternating Current
ADC	Analog-To-Digital Converter
AMC	Advanced Mezzanine Card
ARES	Accelerator Research Experiment at SINBAD
ATCA	Advanced Telecommunication Computing Architecture
BOC	Barrel-Open Cavity
BPM	Beam Position Monitor
CERN	European Organization for Nuclear Research
CLK	Clock
CW	Continuous Wave
DAC	Digital-To-Analog Converter
DC	Direct Current
DESY	Deutsches Elektronen-Synchrotron
DUT	Device Under Test
EIA	Electronic Industries Alliance
EMI	Electromagnetic Interference
ENIG	Electroless Nickel Immersion Gold
EuXFEL	European X-ray Free-Electron Laser
FEL	Free-Electron Laser
FFT	Fast Fourier Transformation
FGB	Frequency Generation Box
FLASH	Free-Electron Laser in Hamburg
FMC	FPGA Mezzanine Card
FPGA	Field Programmable Gate Array
FRED	Fuse-Relay-Board
HASL	Hot Air Solder Leveling
HFSS	High-Frequency Structure Simulator
HPF	High-Pass Filter
IF	Intermediate Frequency
IIPn	nth-Order Input Intercept Point
IPn	nth-Order Intercept Point

IPAC	International Particle Accelerator Conference
LLRF	Low-Level Radio Frequency
LO	Local Oscillator
LSF	Least-Squares Fit
MO	Master Oscillator
MicroTCA	Micro Telecommunications Computing Architecture
NF	Noise Figure
OCXO	Oven Controlled Crystal Oscillator
OIPn	n-th Order Output Intercept Point
OSP	Organic Solderability Preservative
P1dB	1 dB Compression Point
PA	Pre-Amplifier
PCB	Printed Circuit Board
PCC	Pearson Correlation Coefficient
PSD	Power Spectral Density
PSI	Paul-Scherrer Institut
PolariX	Polarizable X-band
REGAE	Relativistic Electron Gun for Atomic Exploration
RF	Radio Frequency
RMS	Root Mean Square
RTM	Rear-transition Module
RoHS	Restriction of Hazardous Substances
SINBAD	Short Innovative Bunches and Accelerators at DESY
SNR	Signal-To-Noise Ratio
SWS	Standing Wave Structure
TDS	Transverse Deflecting Structure
TE	Transverse Electric
TESLA	TeV-Energy Superconducting Linear Accelerator
TMCB	Temperature Monitor And Control Board
TWS	Traveling Wave Structure
UniLOGM	Universal Local Oscillator And Clock Generation Module
VM	Vector Modulator
XDWC	X-band Down-converter PCB
XDWCM	X-band Down-converter Module
XDWCM_UPC	X-band Down-conveter Module With Up-conversion
XLOG	X-band LO generation PCB
XLOGM	X-band Local Oscillator Generation Module
XUPC	X-band Up-converter PCB

Contents

Chapter 1

Introduction

With modern technology, the requirements for machines become stricter and stricter. For particle accelerators and specifically pulsed machines, one aspect of the stricter requirements is that the pulses become shorter and shorter. This in return also increases the requirements for diagnosis tools. A commonly used tool is a transverse deflecting structure (*TDS*) which allows analysis of the beam along the longitudinal axis. To fulfill the requirements at the Free-Electron Laser in Hamburg (*FLASH*) and Short Innovative Bunches and Accelerators at DESY (*SINBAD*) facilities for ultra-short pulses and achieve the required resolution for beam analysis, a collaboration between DESY, Paul-Scherrer-Insitut PSI, and CERN has successfully developed and built a modular X-band transverse deflecting structure system. The prototype of the polarizable X-band (*PolariX*) TDS, which offers the novelty of providing variable polarization to the deflecting force, was installed at the FLASHForward beamline at FLASH. The radio frequency (*RF*) field within the system is measured and controlled by a digital low-level RF (*LLRF*) system. Alongside FLASHForward, the FLASH2 beamline and the SINBAD facility will also use the PolariX TDS in the near future. At FLASH, the fundamental frequency of the RF is 1.3 GHz and at SINBAD it is 3 GHz while the PolariX TDS is build with 12 GHz as resonance frequency. The advantage of using 12 GHz compared to lower frequencies is a better timing resolution without a drastic increase in power of the RF field, as the deflecting force scales linearly with frequency but only with the square-root of the power. The downside of using different frequencies is that LLRF systems for 12 GHz do not exist yet at DESY and need to be developed. Utilizing the digital domain for controls, this can either be done by developing completely new hardware which directly processes the 12 GHz signals or by developing new hardware that converts the 12 GHz signals to a frequency that can be processed by already existing LLRF systems. The former approach requires a lot more investment and new developments which is why the latter approach of building conversion hardware has been chosen. This however adds a certain level of noise to the measured and driven signals, which may lead to disturbances too large to be acceptable. For LLRF systems and especially TDSs, the phase noise is critical and needs to be carefully treated.

The subject of this thesis is the development of said conversion hardware between 3 GHz and 12 GHz with a minimum of phase noise added to the signals. For the prototype setup at FLASH, the 1.3 GHz are converted to 3 GHz before being used in the newly developed hardware. Chapter 2 introduces the basics of this thesis. These are the fundamentals of RF electronics in general with a focus on (phase) noise as well as an introduction to the types of cavities, the use of TDSs in general, and the novelties of the PolariX TDS.

Following up in Chapter 3 is the concept of the whole LLRF system used at FLASHForward and the design and development process of the conversion hardware. This includes an explanation of the already existing hardware that is re-used and a detailed description of the setup of the conversion process. Measurement results from the laboratory are shown and analyzed and are related to the specifications given to the overall setup at FLASHForward.

Chapter 4 covers the installation and commissioning at FLASHFoward with a thorough analysis of the measured signals with the LLRF system built before. Feasible means of analyzing the measured data are presented and compared followed by interpreting these data and relating them to observed behavior and specifications.

Chapter 5 presents an outlook on the planned setup at the other facilities at DESY, namely FLASH2 and SINBAD and their differences to the prototype setup at FLASHForward. The pulse compressing principle with a barrel-open cavity that is planned to be installed at all facilities is also explained here. In the end, an overview of control algorithms is given. This covers already used controls as well as observed difficulties with the current setup and means to correct them are proposed.

Chapter 2

Basics

Goal of this thesis is to build a LLRF system to control the novel structure PolariX TDS. The name PolariX TDS is derived from Polarizable X-band TDS. In this chapter, the basics needed for a general understanding of this thesis are described. An introduction to the fundamentals of RF electronics is given in Section 2.1, with a focus on the important parameters since the LLRF system is heavily dependent on these. Section 2.2 gives an overview of the different types of structures used in particle accelerators. The differences between normal- and superconducting and standing wave (SWS) and traveling wave structures (TWS) are explained as well as the differences between accelerating and transverse deflecting structures.

2.1 RF Electronics

In this section, the fundamentals of RF electronics needed for this thesis are explained. A general overview can be found in [1]. Mixers in Subsection 2.1.1 and amplifiers in Subsection 2.1.2 are the main components needed. Since the most important property for the LLRF system is noise, the fundamentals are explained at the end of Subsection 2.1.3.

2.1.1 Mixers

RF *mixers* (also known as *modulator*, *synchronous detector* or *phase detector*) are usually passive, non-linear three-port electronic circuits used for mixing two independent input frequencies by multiplication.

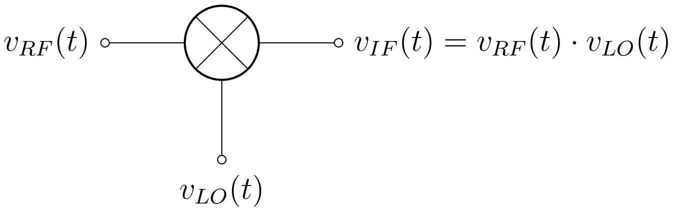

Figure 2.1: Circuit symbol of a mixer.

Fig. 2.1 shows the circuit symbol of a mixer, the signals are called radio frequency (RF), local oscillator (LO) and intermediate frequency (IF). Usually, the LO signal is a constant input and functions as a driving signal in the conversion process. Which signal is the second input depends on the mixer being used as up- or down-converter. The IF signal usually has the lowest frequency, therefore in up-conversion it is the second input, and output signal in down-conversion, vice versa for the RF signal.

Assume a sinusoidal signal in the form of

$$v_x(t) = \cos(\omega_x \cdot t). \tag{2.1}$$

Multiplying two of them as shown in Fig. 2.1 yields

$$\begin{aligned} v_{IF}(t) &= v_{RF}(t) \cdot v_{LO}(t) \\ &= \cos(\omega_{RF} t) \cdot \cos(\omega_{LO} t) \\ &= \frac{1}{2}[\cos((\omega_{RF} - \omega_{LO})t) + \cos((\omega_{RF} + \omega_{LO})t)]. \end{aligned} \tag{2.2}$$

This shows that both the sum and the difference of the input frequencies are created in the process, independently on positive or negative sign of the difference as $\cos(-x) = \cos(x)$. Furthermore, as mixers are non-linear components, harmonics (integer multiples of the resulting frequencies) of the individual signals are also created. The theory behind this can be found in [2]. By filtering out the unwanted frequencies, such a circuit can be used for up- or down-conversion.

There are various types of mixers available on the market, the most common ones being unbalanced, single-balanced and double-balanced mixers. The difference between these types can be seen in the frequency spectrum at the output port. While unbalanced mixers do not only yield the desired mixed frequency, both input frequencies and various harmonics can also be seen, which then need to be filtered out. Single- and double-balanced mixers suppress more of the unwanted spurious signals but in return need a higher LO drive to function properly. Further in-depth details about mixers can be found in [3] and [4].

When selecting RF mixers for the LLRF system, the most important parameters are the following:

- *Frequency*: The RF and LO signal must obviously fit the specification.
- *Mixer level*: The power at which the LO signal switches the internal diode(s).
- *Conversion loss*: Power loss of the signal in the conversion process.
- *1 dB compression point (P1dB)*: Describes the mixers linearity defined by the point where the gain is reduced by 1 dB compared to full linear increasing signal. (See Fig. 2.2)
- *Third-order intercept point (IP3)*: The IP3 is another quantity to measure the linearity of mixers. It is determined by the intercept point of the theoretical fundamental signal and that of the third-order intermodulation product. (See Fig. 2.2)
- *Isolation*: Describes how much power of one signal leaks directly to the other ports.
- *Noise figure*: How much the signal-to-noise ratio reduces in the conversion process.

Obvious is the frequency. Knowing the desired signal frequencies, the mixers specification must fit into it. Another critical point is the mixer level, which usually means the LO signal power. Besides the frequency, the power levels of the signals are also important and need to fit the mixer parameters.

Usually a power plan can be made to specify the power levels at each point in the circuit. From that, the given and required power levels at the inputs and output respectively can be read. Combined with the conversion loss of the mixer, a fitting component can be selected. Isolation parameters are usually given in terms of two ports and describe how much power leaks between these ports by giving the attenuation. E.g. an *LO-IF Isolation* of 30 dB means that the LO signal can be seen at the IF port reduced by 30 dB. Depending on the frequencies, this parameter can become less important since filters could easily handle a frequency far away from the desired one. The noise figure describes how much noise is added to a signal by a component. It is defined as the ratio of input and output signal-to-noise ratio (*SNR*). Since this is usually given in dB, the noise figure is defined as $\mathrm{NF} = \mathrm{SNR}_{\mathrm{input}} - \mathrm{SNR}_{\mathrm{output}}$. A smaller noise figure thus means less added noise and is in most cases desired.

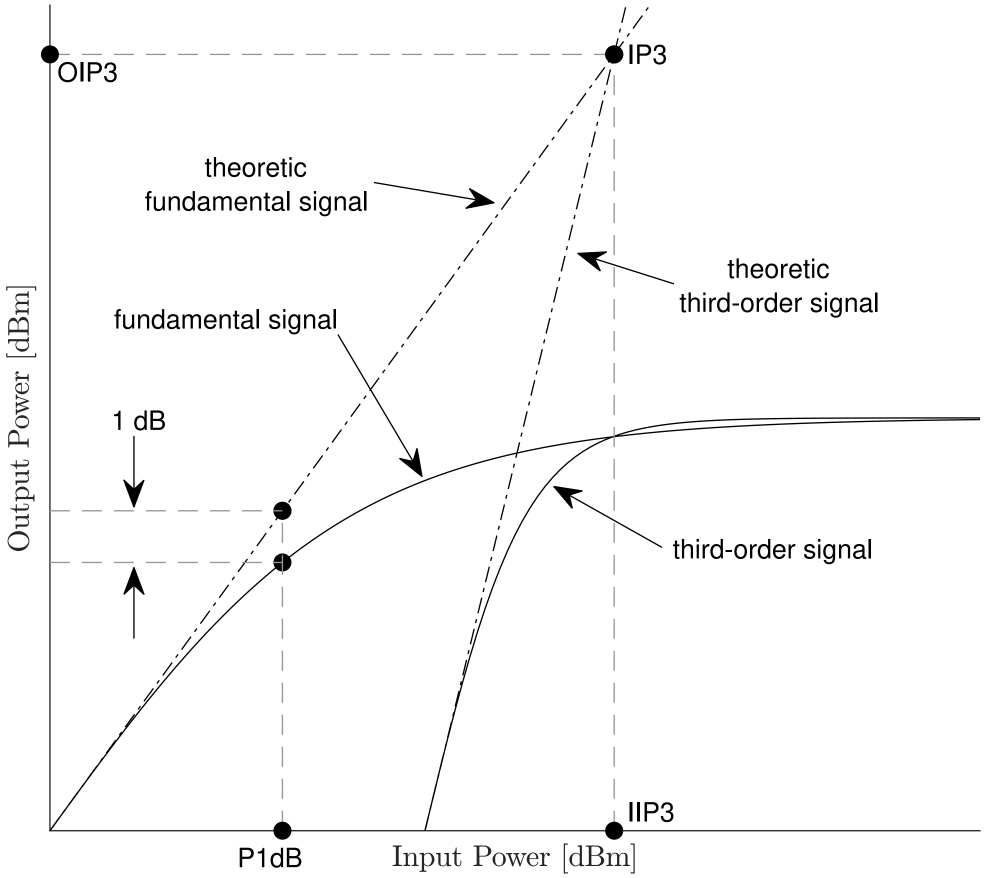

Figure 2.2: The 1 dB compression and third-order intercept point, [5].

Fig. 2.2 visualizes how the P1dB and IP3 are determined graphically, both are means to determine the linearity of RF components. With increasing input power, most components become more and more saturated until they reach full saturation where the output power does not change at all anymore or even decreases when increasing the input power. The P1dB describes the input power at which the components theoretical full-linear fundamental signal is 1 dB higher than the actual fundamental signal. In other words, it describes the point at which a component starts going into saturation. For the IP3, the harmonics and intermodulation products need to be considered. A well written explanation can be found in [6]. With a sinusoidal signal $x(t) = A\cos(\omega t + \varphi)$ with amplitude A, frequency ω and phase φ, a fully linear signal would yield the response $y(t)_{linear} = a_0 + a_1 x(t)$. But since real components are never fully linear, non-linear parts need to be added to that response, which is also better known as the Taylor series expansion of a transfer function

$$y(t) = a_0 + a_1 x(t) + a_2 x(t)^2 + a_3 x(t)^3 + a_4 x(t)^4 + ... + a_n x(t)^n. \tag{2.3}$$

Analyzing the first terms with trigonometric identities shows that the term of n-th order produces a result containing n times the input frequency

$$\begin{array}{rrr}
a_0 & & \text{DC offset} \\
a_1 x(t) & \cos(x) & \text{contains } \omega \\
a_2 x(t)^2 & \cos^2(x) = \dfrac{1}{2}(1 + \cos(2x)) & \text{contains } 2\omega \\
a_3 x(t)^3 & \cos^3(x) = \dfrac{1}{4}(3\cos(x) + \cos(3x)) & \text{contains } \omega \text{ and } 3\omega \\
... & ... & ...
\end{array}$$

These harmonics can usually easily be filtered out and do not interfere with the desired result, as the gap between them is relatively large. However, $\cos^3(x)$ does not only contain the third harmonic but also contributes to the fundamental signal which is then composed of $a_1 A\cos(\omega t)$, the wanted fundamental, and $\frac{3}{4} a_3 A^3 \cos(\omega t)$, the disturbing part of the third-order term leading to compression when a_3 is negative [7].

When the signal is composed of two (or more) inputs $x(t) = x_1(t) + x_2(t)$ with frequencies ω_1 and ω_2 and amplitudes A_1 and A_2, these interfere with each other which is called *intermodulation*. Analyzing the higher-order terms again shows that especially the third-order intermodulation can cause problems (dependency on t is dropped for visual clarity)

$$
\begin{aligned}
&a_2x^2 = a_2(x_1+x_2)^2 = a_2(x_1^2+x_2^2+2x_1x_2)\\
&a_3x^3 = a_3(x_1+x_2)^3 = a_3(x_1^3+x_2^3+3x_1^2x_2+3x_2^2x_1)\\
&\ldots
\end{aligned}
$$

As shown in 2.2, multiplying two different frequencies yields their sum as well as their difference. As such, the term $x_1^2x_2$ and $x_2^2x_1$ generates among others the frequencies $2\omega_1-\omega_2$ and $2\omega_2-\omega_1$, which, dependent on the two frequencies, can be very close to the original ones ω_1 and ω_2 and may prove problematic to be efficiently filtered out. This holds true for all odd-order terms of the response, although the third-order term is the most critical one. From 2.3 and Fig. 2.2 also follows, the higher the order of the term, the higher is its slope. Hence when doubling the input power, the output power of the linear term a_1x also doubles, the output of the second-order term a_2x^2 quadruples and that of the third-order term a_3x^3 is multiplied by $2^3 = 8$. Or more generally, the output power is multiplied by 2^n for the n-th order term. It follows that all non-linear terms will at some point cross the line of the linear term. These points are called *n-th order intercept points* or short *IPn*, in case of the third-order term it is the *third-order intercept point* or *IP3*. The corresponding values are called *input* and *output intercept points of n-th order*, or short *IIPn* or *OIPn*, respectively, and usually give the actual input or output power of the theoretical intercept point. For a component this means, the more a device goes into saturation, the less the differences between the wanted linear and unwanted non-linear terms become. On the other hand, higher IPn values means that it takes longer for the higher-order terms to become relevant in comparison to the linear term. For real components, usually only the IP3 is relevant and considered in the selection process.

With the fundamentals of P1dB and IP3 explained, it becomes clear that the mixer level is connected to both of these values. With some exceptions, RF components are usually operated in the linear region and depending on the expected RF input power, the mixer level needs to be chosen accordingly to not operate in saturation.

2.1.2 Amplifiers

Amplifiers exist in various forms and types as seen in [8]. It is an active RF component taking a DC voltage to amplify an input signal by a certain gain when the signal power is not sufficient for further processing. Fig. 2.3 shows the circuit symbol of an RF power amplifier and also its simpler form, since one usually is not interested in the actual DC power supply when showing the RF circuit.

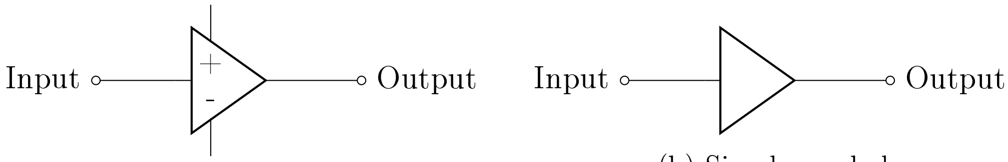

(a) Full symbol.

(b) Simple symbol.

Figure 2.3: Full and simple form of the circuit symbol of an RF power amplifier.

Amplifiers in general have the same criteria as mixers. Therefore, the relevant parameters when selecting one are the following:

- *Frequency*: The amplifier must be suitable for the desired operating frequency.
- *Conversion gain*: Instead of the loss, amplifiers are components that add power to a signal. As such, the gain is usually mentioned.
- *Saturated output power*: The maximum output power the amplifier can deliver in full saturation.
- *1 dB compression point (P1dB)*: Same as for mixers.
- *Third-order intercept point (IP3)*: Same as for mixers.
- *Noise figure*: Same as for mixers.

Most obviously, the operating frequency must be suitable for the selected amplifier. Also, the required output and available input power must be known to select an appropriate gain. Depending on how critical higher-order terms are, the amplifier should only be used in the linear region or can use its full saturated output power. The linearity measures P1dB and IP3 are the same as for mixers, but the IP3 is often not as critical when only a single frequency signal is processed through the amplifier and harmonics can be filtered out. The P1dB then is only important to see from which input power on the amplifier begins to saturate.

2.1.3 Noise

So far, this thesis has only mentioned noise in terms of the noise figure analysis of mixers and amplifiers. For a better understanding of noise and the different types of noise, a small explanation based on [9] and [10] is done here. Equation 2.1 given above describes a perfect sinusoidal wave. A real RF wave would have the form of

$$v(t) = V_0(1 + \alpha(t)) \cos(\omega t + \varphi(t)) \tag{2.4}$$

with

- V_0 : Desired peak amplitude
- $\alpha(t)$: Amplitude instability (amplitude noise)
- ω : Angular frequency of the signal $\omega = 2\pi f$
- f : Frequency
- t : Time
- $\varphi(t)$: Phase instability (phase noise)

From this, we can see that amplitude and phase have certain instabilities that vary with time, that can disturb the signal. Fig. 2.4 shows a sinusoidal signal with only amplitude noise (Fig. 2.4a), only phase noise (Fig. 2.4b) and amplitude and phase noise combined (Fig. 2.4c). The details are explained in the following sections.

Amplitude and phase noise Assuming a signal has only amplitude noise ($\varphi(t) = 0$), 2.4 is reduced to

$$\begin{aligned} v(t) &= V_0(1 + \alpha(t)) \cos(\omega t) \\ &= V_0 \cos(\omega t) + V_0 \alpha(t) \cos(\omega t). \end{aligned} \tag{2.5}$$

$\alpha(t)$ usually is randomly distributed noise that is added to the amplitude of the undisturbed signal. Since according to 2.5 the noise is also scaled by the actual amplitude, its impact becomes smaller towards the zero crossings and larger towards the extrema. Fig. 2.4a also shows this. Doing the same for phase noise only ($\alpha(t) = 0$), 2.4 is reduced to

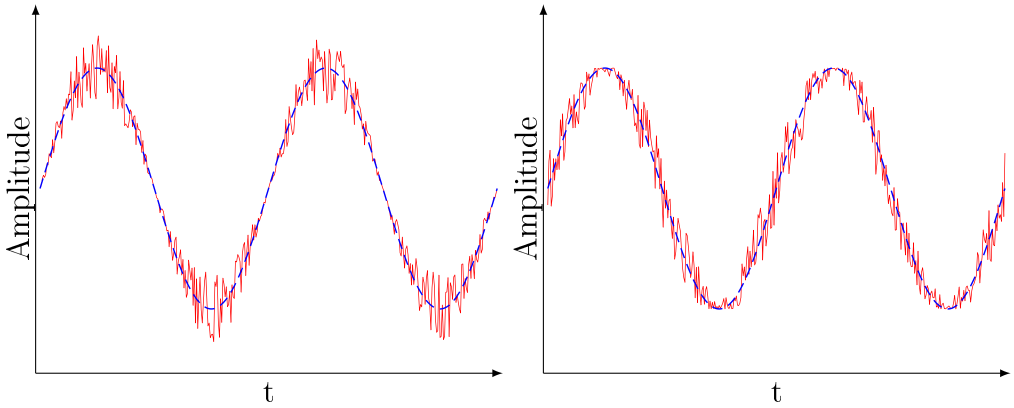

(a) Amplitude noise. (b) Phase noise.

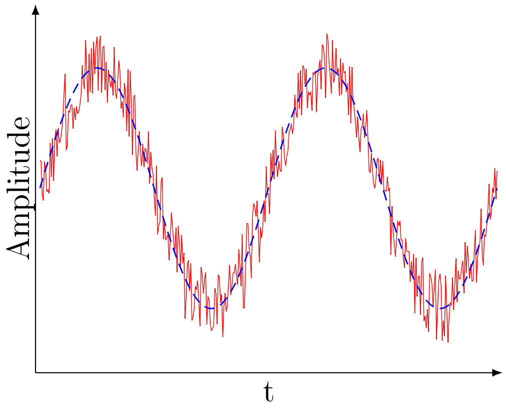

(c) Amplitude and phase noise.

Figure 2.4: A sinusoidal signal with added noise; blue: noiseless signal, red: noisy signal.

$$v(t) = V_0 \cos(\omega t + \varphi(t)). \tag{2.6}$$

Here, the noise is only affecting the phase and as such can never cause amplitudes larger than V_0. In contrast to amplitude noise, phase noise is stronger towards zero crossings and weaker towards the extrema. This can also be seen by looking at Fig. 2.4b, a small change in phase around a zero crossing can cause a much higher change of the amplitude since the gradient of a sine wave is highest at the zero crossings and zero at the extrema. For further analysis, it is assumed that both noise values are small compared to the original signal: $\frac{\alpha}{V} \ll 1$, $\varphi \approx 0$. For the phase noise, with $\sin(\varphi) \approx \varphi$, $\cos(\varphi) \approx 1$ and the sum identity, this means 2.6 can be written as

$$
\begin{aligned}
v(t) &= V_0(\cos(\omega t) - \varphi(t)\sin(\omega t)) \\
&= V_0\cos(\omega t) - V_0\varphi(t)\sin(\omega t). \qquad (2.7)
\end{aligned}
$$

Comparing 2.5 and 2.7 with $\alpha(t)$ and $\varphi(t)$ randomly distributed values, both equations show that noise causes modulation of the carrier towards both higher and lower frequencies. This is easier to see in the frequency domain. Using Fourier-analysis, a noiseless signal would be a single spike at the desired frequency ω_c (called carrier frequency) in the spectrum as shown in Fig. 2.5a. Introducing either amplitude or phase noise (or both), the spectrum looks as shown in Fig. 2.5b. Both noise types introduce a continuously distributed signal around the carrier frequency.

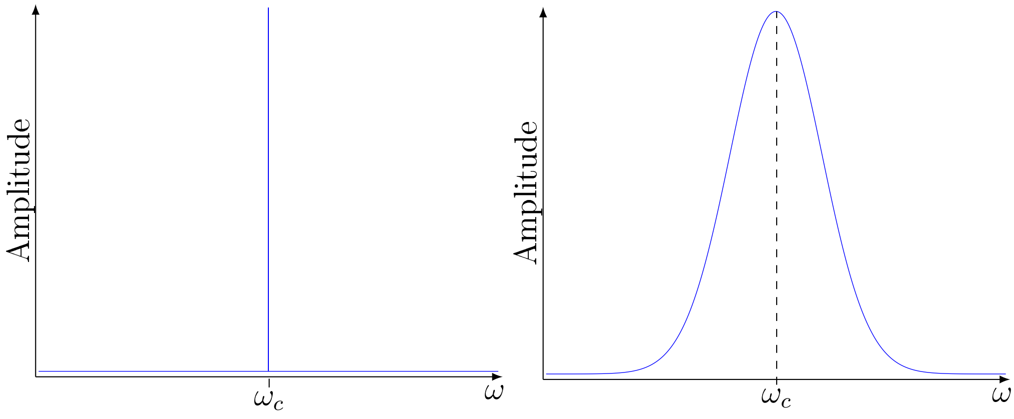

(a) Spectrum of a noiseless signal.

(b) Spectrum with noise.

Figure 2.5: Frequency spectra of sinusoidal signal, without and with added noise.

Since for this thesis, the phase noise is much more important than amplitude noise, the focus is laid on the former. Additional details can be found in the sources mentioned at the beginning of this section. Phase noise is usually measured as the average power spectral density (PSD) of a signal [10]

$$S_\varphi(f) = \langle|\Phi(f)|^2\rangle_m$$

with

- $\Phi(f)$: Fourier-transformation of the phase noise: $\mathcal{F}(\varphi(t))$
- f : Offset frequency from the carrier

- m : number of spectra

$S_\varphi(t)$ is the two-sided PSD of the phase noise. Since the distribution around the carrier frequency is symmetric, the phase noise is usually given as the single-sided PSD $\mathcal{L}(f)$ [7]

$$\mathcal{L}(f) = \frac{S_\varphi(t)}{2}.$$

For a better quantification of the phase noise, the root mean square (RMS) jitter is used. It is gained by integration of $\mathcal{L}(f)$ over the bandwidth of interest

$$\varphi_{\mathrm{RMS}} = \sqrt{\int\limits_{f_1}^{f_2} \mathcal{L}(f) df}.$$

From this, the RMS timing jitter can be derived which is used in this thesis to quantify phase noise

$$t_{RMS} = \frac{1}{\omega_c}\varphi_{\mathrm{RMS}} = \frac{1}{\omega_c}\sqrt{\int\limits_{f_1}^{f_2} \mathcal{L}(f) df}. \tag{2.8}$$

For a better differentiation between short-term and long-term behavior, we define short-term effects as *jitter* and long-term effects as *drift*.

2.2 Types of cavities

RF cavity resonators (also: RF cavities) are used in all kinds of particle accelerators and exist for various applications with different requirements. The most common use of cavities is to accelerate particles, but since there are many different types of accelerators, this led to various types of cavities all with different properties, e.g. superconducting and normal-conducting, pulsed and continuous wave (CW) operation or fixed and variable RF frequency. In this chapter, a comparison is made as a formal description of the different types with a focus on fixed RF frequency cavities as these are mainly used in current state-of-the-art free-electron lasers (FEL). For a more in-depth comparison see [11, 12]. The fact that multiple different kinds of technologies exist leads to the conclusion that there is no superior one and all of them have their advantages and disadvantages.

2.2.1 Normal- and superconducting cavities

When it comes to normal- and superconducting cavities, H. Podlech made a thorough comparison of both technologies in [13]. The most noticeable difference is the quality factor (*Q-factor* or Q), which is a parameter describing the dampening of a resonator. In other words, it is the quotient of the energy stored within the cavity divided by the energy dissipated in the cavity walls per oscillation cycle. While normal-conducting cavities usually have a Q in the range of 10^3 to 10^5, superconducting cavities lie between 10^7 to 10^{11} which in turn means that the surface resistance of normal-conducting cavities is typically five order of magnitude higher than that of superconducting ones. Out of this follows, that a normal-conducting cavity suffers more in terms of heat dissipation when operating under the same conditions. Ultimately, this can lead to temperatures so high, that the cavity is damaged and inoperational. Due to that, normal-conducting cavities are usually operated with pulsed RF. Contrary to that, with extremely low losses in the cavity walls, superconducting cavities are well-suited for CW operation, but in turn require a cryogenic plant and infrastructure to achieve the superconductivity. Additionally, the cavities become very sensitive to microphonics and inhomogeneities in the vacuum and the beam and require fast tuners with piezo elements to compensate this. Microphonics on the other side can be compensated by the LLRF system.

Another limiting factor is the fill time T_{fill}, describing the time an RF field needs to fill the cavity with power until it reaches a steady-state. It follows from

$$T_{fill} = \frac{Q}{\omega}$$

with Q the quality factor and ω the resonance angular frequency of the cavity. For a given ω, the fill time only depends on Q, thus normal-conducting cavities have a shorter fill time than superconducting ones. Typically, this is in the region of nano- to microseconds for normal-conducting and up to several hundreds of milliseconds for superconducting cavities, depending on the resonance frequency. For CW machines, this is not important as the RF field only needs to fill the cavity once and is kept inside permanently. For pulsed machines though, the RF field needs to fill the cavity, must be held at constant energy for the time the beam is passing through and then leaves the cavity. This repeats for every pulse, thus the repetition rate of the beam pulses is limited by the fill time of the cavity. As general rule of thumb, normal-conducting cavities are better suited when the machine is operated with low beam energy, a high beam current and pulsed mode, and vice versa for superconductive cavities.

However, this does not mean there are no superconducting cavities operated in pulsed mode. An example is the TeV-Energy Superconducting Linear Accelerator (*TESLA*) cavity [14]. It is used in the EuXFEL, FLASH and many other facilities, cooled down to superconductivity and operated in pulsed mode. It has a resonance frequency of 1.3 GHz, a loaded quality factor of about $3 \cdot 10^6$ resulting in a fill time of roughly 350 μs and can achieve an accelerating field of about 25 MV/m. At EuXFEL, along its length of about 3 km, this leads to very high beam energy, which excludes the usage of normal-conducting cavities due to the heat dissipation. But there are also preparations in progress to switch to CW operation as seen in [15].

2.2.2 Standing and traveling wave cavities

Apart from normal- and superconducting cavities, the way the RF inside the cavity is built up to interact with the beam can also differ. One can either use a standing wave (*SWS, standing wave structure*) or a traveling wave (*TWS, traveling wave structure*) pattern. Fig. 2.6 shows the theoretical setup for each of the different possibilities. SWS (Fig. 2.6a) usually require a single input coupler or antenna for the RF (red) in the cavity. The incoming wave then gets reflected back and forth from the cavity walls and thus creates a standing wave pattern. In order to accelerate particles, the timing needs to be such that when the beam (blue) travels through a cell of the cavity, the RF field points in the direction of the beam while it travels through it. For TWS (Fig. 2.6b), the RF is coupled in on one side of the cavity, travels through it once and is coupled out at the other end of the cavity to be then terminated in a load. For acceleration, the timing here needs to be such that the beam enters the cavity while the RF field is at its maximum. The beam velocity and the RF field phase velocity then need to be the same, such that the beam always sees the same phase of the RF field. Visually speaking, the beam "surfs" with the RF field.

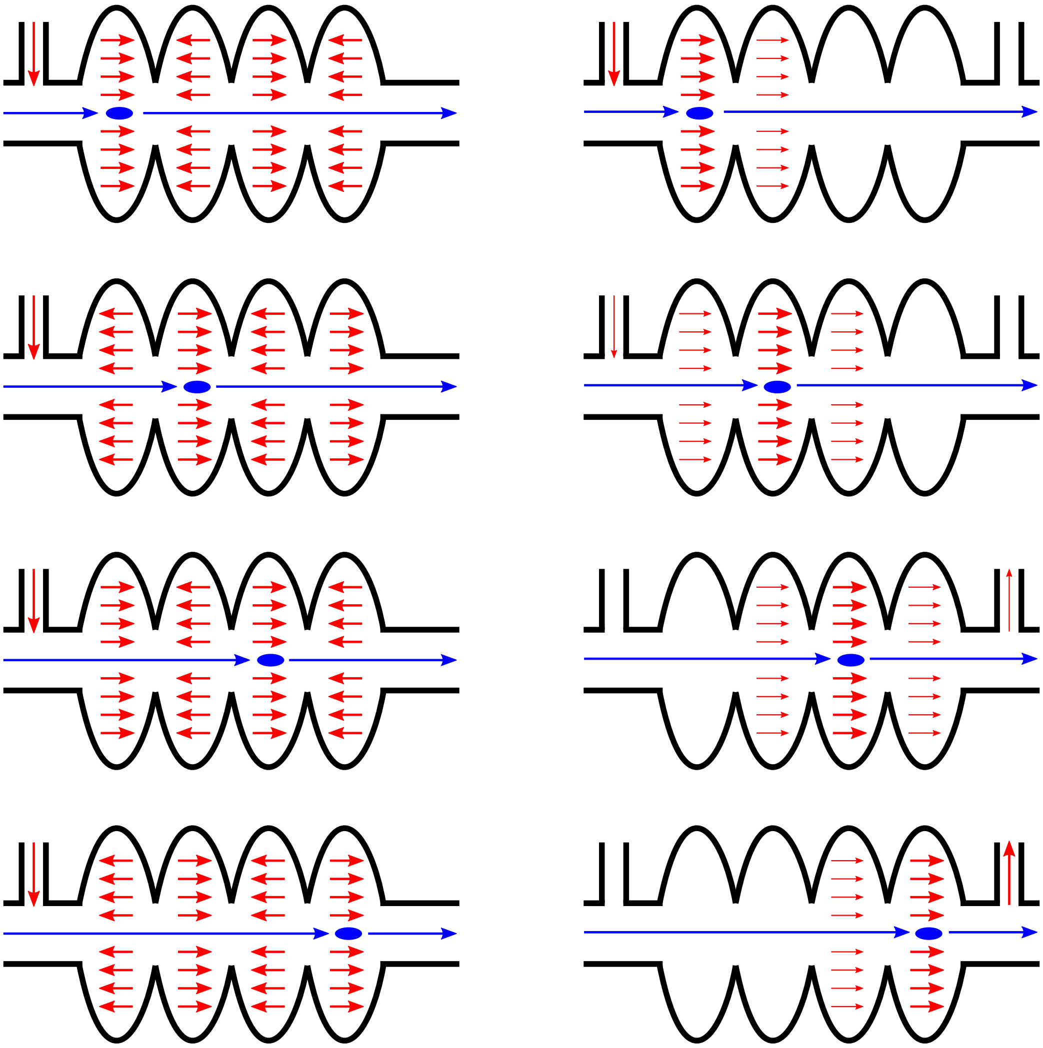

(a) Standing wave principle.

(b) Traveling wave principle.

Figure 2.6: Working principles of standing and traveling wave structures.

The fill time mentioned in the previous section also holds for both types of operation, yet in a standing wave cavity the RF needs to travel back and forth through the cavity in order to reach its maximum. In other words, it takes multiple times the fill time to actually reach the desired field strength, which in turn can be larger than in a TWS for similar given structural properties. TWS in turn can be run with shorter pulses and a higher repetition rate since it is not necessary to wait for the field to reach its desired strength. An operational difference exists for TWS, they can be run with either a forward or a backward traveling wave. The setup shown in Fig. 2.6b shows a forward TWS, the RF is coupled in on the same side as the beam and both travel through the cavity in the same direction. In backward TWS, the RF is coupled in on the opposite side of the beam entrance and fills the cavity in reverse. To understand the working prinicple of TWS, the difference between phase and group velocity is important, since only the phase velocity matters. A TWS is basically a hollow waveguide, where the phase velocity is always faster than the speed of light [16], but the beam and the phase of the RF need to propagate at the same speed. To solve this, so called *irises* are introduced which slow down the phase velocity to match that of the beam. For forward TWS, beam, group and phase velocity all travel in the same direction. In backward TWS, the phase velocity is negative but since it is coupled in from the opposite side of the beam, it travels in the same direction as the beam.

2.2.3 Transverse deflecting structures

RF cavities cannot only be used for accelerating particles, there exist various other applications. G. Burt gives a good overview in [17]. The important one for this thesis is deflection of a particle beam. This is mostly done in so called transverse deflecting structures (*TDS*). As the name suggests, they deflect the beam in the transverse plane instead of accelerating it. This can be interpreted as rotation of the beam without changing its direction and thus makes an analysis on the former longitudinal axis possible. This is usally done to measure the bunch length of the beam. K. Flöttmann and V. Paramonov give a very detailed insight to TDS in [18]. A schematic view of the principles of accelerating and deflecting structures is shown in Fig. 2.7. For acceleration, the timing is such that the beam (blue) sees a maximum of the electric field when traveling through the cavity. Since the beam is a bunch of particles with a certain length and the RF field has almost no change at a maximum, every part of the beam sees almost the same field and thus gains the same amount of energy. If this would not be the case, the beam would be distorted and/or deflected, which is used for TDS. Here, the timing is such that the beam is centered around a zero crossing of the RF field. Around the zero crossing, the field is almost linear which results in an increased amount of energy gained on the outer ends of the bunch resulting in a certain kick to the particles in it. Since on one side of the zero crossing the electric field is positive and on the other side it is negative, particles on each side get deflected in opposite directions with increasing strength towards the outer ends. This deflection is usually called *streaking* and ultimately leads to a rotation and stretching of the whole bunch, which then can be monitored on a screen to allow an analysis and characterization along the longitudinal axis as shown in Fig. 2.8. Usually, only one bunch of the bunch pattern (in multi-bunch machines) is extracted with kicker magnets to not interfere with the whole beam all the time.

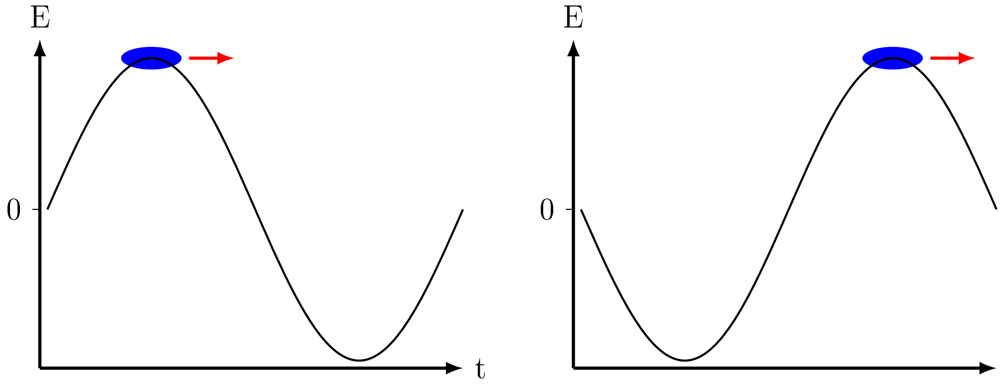

(a) Accelerating structures.

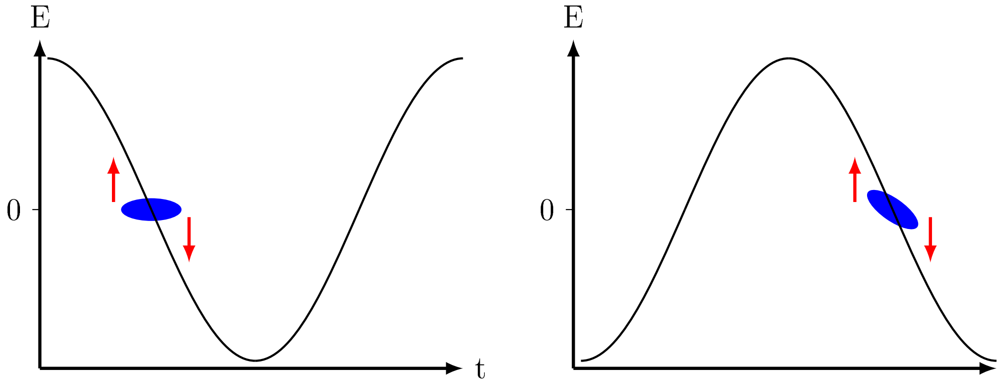

(b) Transverse deflecting structures.

Figure 2.7: Timing relation of RF field and beam in accelerating and transverse deflecting structures.

2.2.4 Polarizable X-band transverse deflecting structure

The polarizable X-band transverse deflecting structure (*PolariX TDS*) is a novel approach to the general concept of TDS. With the need for a TDS

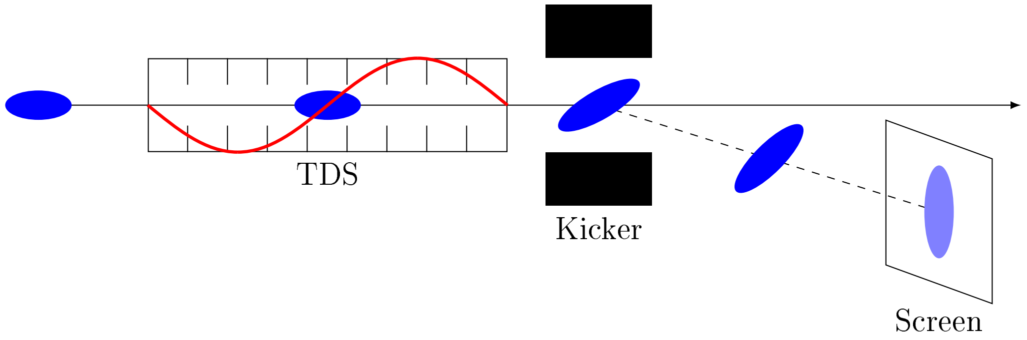

Figure 2.8: Principle of TDS, streaking the beam to allow an analysis along the longitudinal axis.

in the new plasma-wakefield accelerator FLASHForward at DESY [19] and other facilities (FLASH2, SINBAD, ATHOS (SwissFEL)), it has been decided to install the first prototype of the PolariX TDS at FLASHForward. From the technical side, the PolariX TDS is a normal-conducting backward traveling wave structure and, as the name suggests, it is working in the X-band at about 12 GHz. It consists of 96 cells over a length of about one meter. For a comparison, the aforementioned TESLA cavity is also about one meter long, but only consists of 9 cells over that length, working at 1.3 GHz. In a collaboration between DESY, PSI and CERN the first prototype of the PolariX TDS has been designed, produced and tested successfully in the FLASHForward beamline. A first introduction has been made in 2016 by B. Marchetti in [20] describing the idea and procedure of the development. A second paper by P. Craievich [21] from the International Particle Accelerator Conference (*IPAC*) 2018 gives a good overview of the subsequent development steps. The paper [22] then gives a detailed description of the whole system involved in running the PolariX TDS.

The novelty of the PolariX TDS is based on the variable polarization circular waveguide TE11 mode launcher introduced in [23]. It has two rectangular waveguide inputs and one circular output. When applying an RF field in either of the inputs, the resulting field in the circular port is a left or right rotating field as shown in Fig. 2.9a.

Observing the RF at the output along the longitudinal z-axis in Fig. 2.9a, the field can be modeled as a sine wave in x-direction and a 90° shifted one in the perpendicular y-axis. With V_x and V_y as the amplitude in either direction, the rotating fields V_1 and V_2 using only input 1 or 2, respectively, can be described as

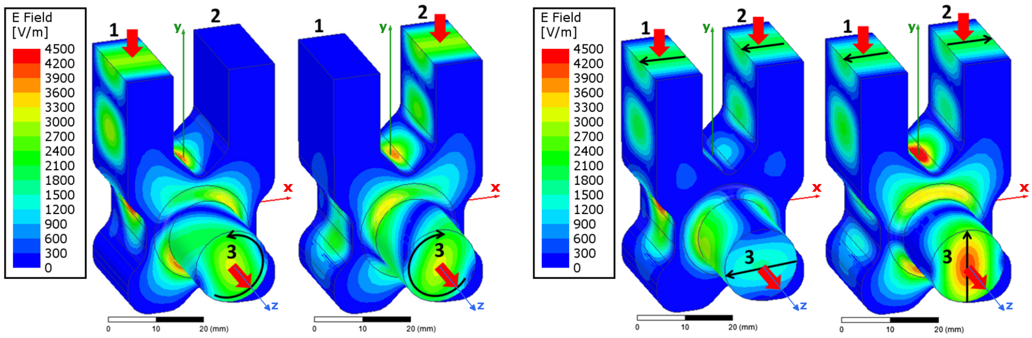

(a) TE11 mode launcher with RF applied in either of the inputs, resulting in a rotating field.

(b) TE11 mode launcher with RF applied in both of the inputs, resulting in a polarized field.

Figure 2.9: Simulation of the TE11 mode launcher showing the RF field strength inside when RF is applied at the inputs [22].

$$V_1 = V_x \sin(\omega t) + V_y \cos(\omega t) \tag{2.9}$$

$$V_2 = V_x \sin(\omega t) - V_y \cos(\omega t). \tag{2.10}$$

Applying both of these fields at the same time results in their addition

$$\begin{aligned} V_{\text{total}} &= V_1 + V_2 \\ &= 2V_x \sin(\omega t). \end{aligned} \tag{2.11}$$

However, the above equation is only true if the two input signals have the same phase. Introducing a phase difference $\Delta\varphi$ to the second input port changes 2.9 and 2.10 to the following

$$\begin{aligned} V_1 &= V_x \sin(\omega t) + V_y \cos(\omega t) \\ V_2 &= V_x \sin(\omega t + \Delta\varphi) - V_y \cos(\omega t + \Delta\varphi). \end{aligned}$$

With this, the total signal is

$$\begin{aligned} V_{\text{total}} &= V_1 + V_2 \\ &= V_x(\sin(\omega t) + \sin(\omega t + \Delta\varphi)) + V_y(\cos(\omega t) - \cos(\omega t + \Delta\varphi)) \\ &= 2V_x \sin(\omega t + \frac{\Delta\varphi}{2}) \cos(-\frac{\Delta\varphi}{2}) - 2V_y \sin(\omega t + \frac{\Delta\varphi}{2}) \sin(-\frac{\Delta\varphi}{2}) \\ &= (2\cos(\frac{\Delta\varphi}{2})V_x + 2\sin(\frac{\Delta\varphi}{2})V_y) \sin(\omega t + \frac{\Delta\varphi}{2}). \end{aligned} \tag{2.12}$$

With equal RF power, depending on the phase difference of the two input ports, the polarization at the output port varies. For a 0° difference as shown in Fig. 2.9b (left), the field is streaking vertically and for a 180° difference as shown in Fig. 2.9b (right) it is horizontally streaking, meaning the RF field is rotated by 90°. The phase difference must be twice as large as the desired rotation of the streaking term as seen in 2.12.

With a single RF source, both ports could be provided with an equal amount of power using an RF splitter. With a variable phase shifter in one of the paths as shown in Fig. 2.10, an arbitrary phase difference can be set which finally allows streaking in any arbitrary direction. Since the phase shifter is mechanically driven by a stepper motor, it is susceptible to uncertainties and later on should only be used if necessary. Since a total 360° phase rotation in the cavity would require a 720° phase shift, the range of the motor is limited to only 360° phase shift and thus 180° phase rotation. To still be able to rotate the beam in any arbitrary angle, the timing of beam and RF can be synchronized such that both different zero crossings of the RF can be used to deflect the beam, which is equal to doing a 180° rotation. With both, phase shifter and zero crossing selection, a full 360° phase rotation is still possible.

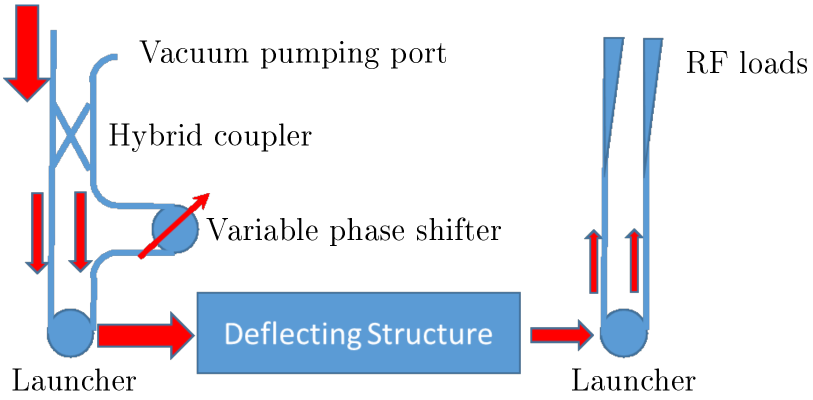

Figure 2.10: Setup concept of the variable polarization in the TDS.

With the ability to streak the beam at any arbitrary angle, it is possible to combine multiple of the resulting 2D images into a three dimensional charge density distribution profile using tomographic reconstruction techniques. At FLASHForward the driver and witness beams in the plasma-wakefield accelerator will be analyzed, FLASH2 will use the PolariX TDS for the measurement of the energy loss and spread induced by FEL lasing to reconstruct photon pulse and also for longitudinal phase space diagnostics. SINBAD uses the TDS to characterize the ultra-short electron bunches for the novel high gradient acceleration techniques. More information on this and the 3D tomographic reconstruction can be found in [24].

2.3 Summary

In this chapter, the necessary fundamentals for a general understanding for this thesis have been explained. This included RF electronics and the most important properties for mixers and amplifiers as well as an explanation of amplitude and phase noise. Also, a comparison of the different type of RF cavities has been given, showing the differences between normal- and superconducting and standing and traveling wave cavities. In the end, the special case of transverse deflecting structures was explained and the features of the novel PolariX TDS were stated.

Chapter 3

The X-band Low-Level RF system

This chapter presents the design of the X-band LLRF system and its realization. The first Section 3.1 explains the general approach on the layout and design of the LLRF system as it was installed in the FLASHForward beamline at DESY in summer 2019. This gives an overview of the whole system. In the following Section 3.2, a detailed description of the newly designed hardware is given. This covers the selection process of RF components, their characterization and comparison, as well as the integration on PCBs and packaging into 19" modules. In the end in Section 3.2.3, the modules are analyzed regarding their stability in phase.

3.1 Design concept

As the PolariX TDS is the first X-band structure installed on the DESY campus, there are no means available to measure, control and drive an RF field for it. Already existing LLRF systems are used to operate structures at 1.3 GHz (FLASH, EuXFEL) or 3 GHz (SINBAD, REGAE). At this point, there are two approaches to build up the new X-band LLRF system. Either, the existing systems are adapted to process X-band frequencies or the signals are adapted to be processed by the already existing systems. The latter approach has been chosen for the X-band LLRF system as it requires less development of new parts. Additionally, similar projects like the X-band linearizer at the FERMI@Elettra FEL have made a proof of the concept [25].

The following describes the general design concept that has been developed for the X-band LLRF system which is installed at the FLASHForward facility. Fig. 3.1 shows a block diagram of it. As described above, the general approach to build the X-band LLRF system is to reuse as many parts as possible from existing LLRF systems. These parts are the Universal Local Oscillator and Clock Generation Module (*UniLOGM*) and the S-band LLRF system already available in Micro Telecommunications Computing Architecture (*MicroTCA*) [26]. They are further described in Subsections 3.1.2 and 3.1.3, respectively. Additionally, the Frequency Generation Box (*FGB*) is needed, its use is described in Subsection 3.1.1.

The X-band Local Oscillator Generation Module (*XLOGM*), X-band Down-converter Module (*XDWCM*) and X-band Down-converter Module with Up-conversion (*XDWCM_UPC*) are designed, developed, and realized as part of this work. The process of selecting and characterizing the required RF components, design of PCBs and the packaging into 19" modules is further described in Subsection 3.2.

3.1.1 Frequency Generation Box

The X-band LLRF system is supposed to be installed at the FLASH and SINBAD facility. While FLASH has a reference signal at 1.3 GHz, SINBAD works with a 3 GHz RF reference. Due to this, a Frequency Generation Box (*FGB*) has already been developed at DESY. This box takes a 1.3 GHz input signal and generates a 2.9972 GHz output signal. For simplicity, 3 GHz is written instead. This arbitrary looking number is caused by the master oscillator (*MO*) of FLASH. As explained in [27], the main signal source is an oven controlled crystal oscillator (*OCXO*) operating at 9.0277775 MHz

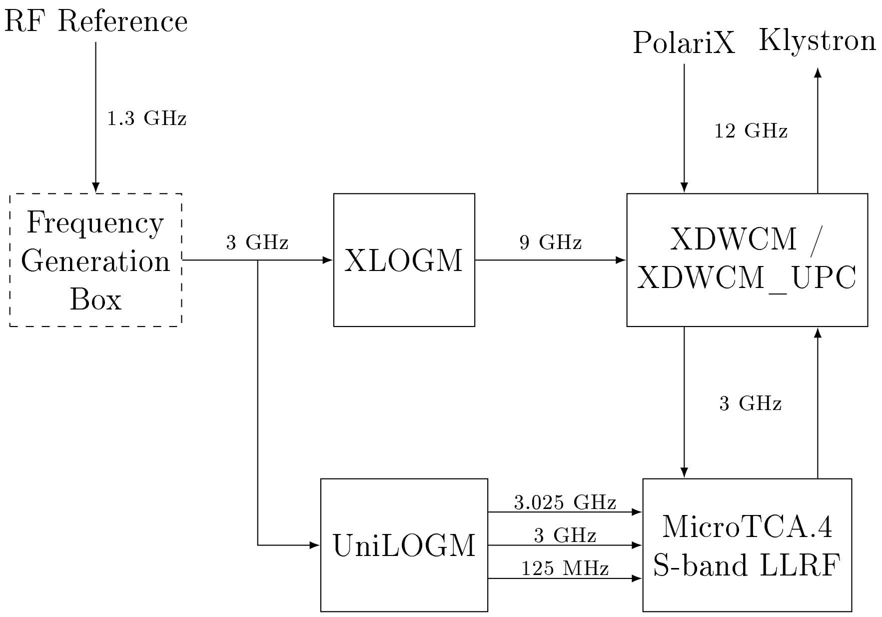

Figure 3.1: Block diagram of the general concept of the LLRF system.

which is then multiplied by a factor of 144 to obtain the reference frequency of 1299.99996 MHz, or short 1.3 GHz. To obtain the desired 3 GHz output, the 9 MHz MO signal has to be multiplied by 332.

$$9.0277775 \text{ MHz} * 332 = 2997.22213 \text{ MHz}.$$

As the 1.3 GHz signal has already been multiplied by 144 in the MO, a factor of $\frac{332}{144}$ or reduced $\frac{83}{36}$ would be needed. As frequency multipliers and dividers do not exist with such factors, the fraction is split into parts with smaller numbers as follows

$$\frac{83}{36} = 2 + \frac{11}{36} = 2 + \frac{1}{3} - \frac{1}{36} = 2 + \frac{1}{3} - \frac{1}{3 \cdot 3 \cdot 4} \tag{3.1}$$

$$= 2 + \frac{1}{3} \cdot (1 - \frac{1}{3 \cdot 4}). \tag{3.2}$$

Fig. 3.2 shows the signal flow of how this conversion is realized in the FGB. As seen in 3.1, $\frac{83}{36}$ can be split into 3 parts. First, the 1.3 GHz is split into two parts via an RF splitter. One output takes care of the integer part and includes a frequency doubler. The other output processes the remainder of $\frac{11}{36}$. As frequency dividers by a factor of three are commonly available and $\frac{11}{36}$ is only $\frac{1}{36}$ away from $\frac{1}{3}$, the part is split up into $\frac{1}{3}$ from which $\frac{1}{36}$ is then subtracted. 36 on the other hand is then split up into the smaller factors

$3 \cdot 3 \cdot 4$. Both fractional parts have a factor of $\frac{1}{3}$, which can be taken care of before further processing as seen in 3.2. This is realized by taking the second output of the RF splitter and dividing the frequency by three and then splitting it up again with another RF splitter, where one part stays unchanged and the other gets again divided by three followed by a frequency division of four to make up the factor of 36. These two signal frequencies are then applied to an RF mixer and everything except the subtraction of the two frequencies is filtered out. This frequency is then again processed by an RF mixer together with the doubled frequency, this time the sum frequency is filtered, which makes up the desired 3 GHz output.

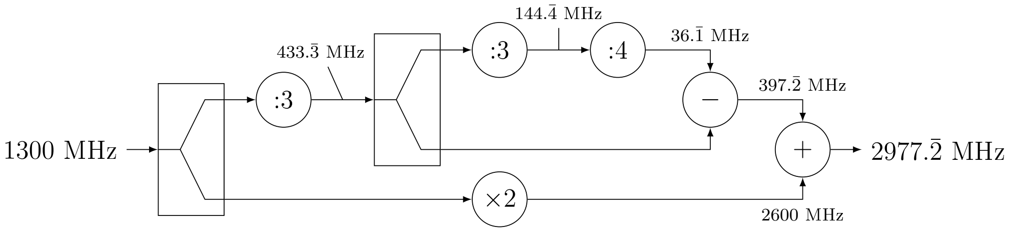

Figure 3.2: Signal flow of the Frequency Generation Box.

3.1.2 Universal Local Oscillator and Clock Generation Module

The Universal Local Oscillator and Clock Generation Module (*UniLOGM*) [28] is a 19" box that takes a reference frequency as input and produces LO and clock (*CLK*) signals depending on the configuration. It can be configured for various input frequencies (300 MHz - 6 GHz). For the present application it is configured for a reference frequency input of 3 GHz. The UniLOGM produces 3.025 GHz (LO), 3 GHz (Reference), and 125 MHz (CLK) output signals needed for further processing of the analog signals in the MicroTCA S-band LLRF system described in the next Subsection 3.1.3.

3.1.3 Micro Telecommunications Computing Architecture S-band LLRF system

The S-band MicroTCA.4 LLRF system is a copy of the system used for the SINBAD and Relativistic Electron Gun for Atomic Exploration (*REGAE*) facilities [29]. Based on the Advanced Telecommunication Computing Architecture (*ATCA*), MicroTCA in the subsidiary specification MicroTCA.4 features manageability, redundancy and a compact form factor [30]. The core of a MicroTCA.4 system is the crate, which holds Advanced Mezzanine Cards (*AMCs*) in the front and Rear-transistion modules (*RTMs*) in the back. Fig. 3.3 shows the general setup of this. Usually, the AMCs operate in the digital domain while the RTMs handle analog signals. Communication between the AMCs and RTMs is done over a connector called *Zone 3*. Also inside the crate is an AMC backplane which allows communication between AMCs and an RF backplane for the exchange of analog signals between RTMs and the distribution of clocks.

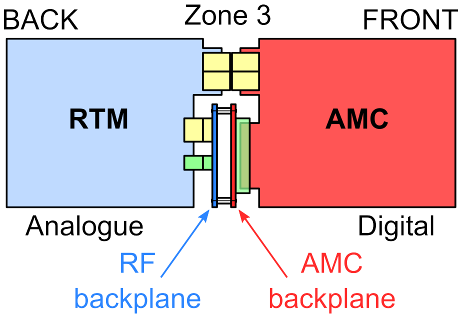

Figure 3.3: MicroTCA.4 crate setup with modules and backplanes [30].

The S-band LLRF system contains the double width Rear-transistion module DRTM-DWC8VM1 (in the following only "DWC8VM1") [31]. It provides an analog front-end for up to eight signals. In the present case, these signals have a frequency of 3 GHz. The DWC8VM1 down-converts these to an intermediate frequency of 25 MHz with an RF mixer and the 3.025 GHz LO signal from the UniLOGM. The down-converted signals are then sent via Zone 3 to the connected AMC. Additionally, it contains a vector modulator output to generate the drive signal for the klystron.

Connected to each DWC8VM1 is a SIS8300L2 AMC [32]. This is a digitizer and signal generator card based on a Xilinx Virtex6 FPGA containing ten analog-to-digital (*ADC*) and two digital-to-analog converters (*DACs*). Both, the converters and FPGA operate at a frequency of 125 MHz which is provided by the UniLOGM.

Additionally one x2timer AMC [33] is installed in the crate. The x2timer is a timing card, which generates clocks and trigger signals which are synchronized with other trigger signals across the whole facility.

3.1.4 X-band Down-converter Module

In order to process 3 GHz signals in the MicroTCA.4 LLRF system, the 12 GHz signals coming from the PolariX TDS need to be converted into the 3

GHz domain. This is done using RF mixers which are packaged into the 19" X-band Down-converter Module (*XDWCM*). Each of these boxes contains eight down-conversion channels. In order to convert 12 GHz down to 3 GHz, an LO signal of 9 GHz is needed. This is provided by the X-band Local Oscillator Generation Module (*XLOGM*) described below.

Additionally, the MicroTCA.4 LLRF system provides the 3 GHz drive signal for the klystron. This signal needs to be up-converted. For this, a variant of the XDWCM, the X-band Down-converter Module with Up-conversion (*XDWCM_UPC*), has been created. In this box, one down-conversion channel is replaced by an up-conversion channel, resulting in seven down-conversion and one up-conversion channel in this box. Providing the drive signal for the PolariX TDS, this box is mandatory for the setup. Depending on how many signals need to be measured, additional XDWCM boxes can be added.

3.1.5 X-band Local Oscillator Generation Module

In the X-band local oscillator generation module (*XLOGM*), an input reference signal at 3 GHz is processed by a frequency tripler to produce an output signal at 9 GHz, which is needed for further processing of the measured signals in the converter modules. As usually more channels are measured than the mandatory XDWCM_UPC provides, additional XDWCM boxes also need the 9 GHz signal. Therefore, the XLOGM provides four outputs.

3.2 Hardware modules

This section describes the building process of the newly developed 19" modules XDWCM, its variation XDWCM_UPC and the XLOGM. As the main focus of the X- to S-band conversion lays on the RF mixer, all other components need to be selected respecting its properties. Therefore, the first Subsection 3.2.1 covers the XDWCM (and XDWCM_UPC), including the RF component selection and characterization with respect to the properties introduced in Chapter 2. Also the development of PCBs, where most of the RF components are placed, is described in Subsection 3.2.1.3 as well as the packaging into housings and 19" modules in Subsection 3.2.1.4. The second Subsection 3.2.2 describes the development of the XLOGM with respect to the requirements of the XDWCM. This part is also divided into RF component selection and characterization, followed by PCB development in Subsection 3.2.2.1 and packaging in 3.2.2.3.

3.2.1 X-band Down-converter Module

As the DWC8VM1 offers eight input channels, it is convenient for the XDWCM to also provide eight channels. Keeping the box as simple as possible, the XDWCM is held completely passive and therefore does not require any power supplies, which results in less added noise. Each box has one 9 GHz LO signal input, eight 12 GHz X-band signal inputs and eight 3 GHz S-band signal outputs. Fig. 3.4 gives an overview of the XDWCM and its components as well as the required power levels of the signals which are explained in the following. The X-band down-converter PCB (*XDWC*) is also shown here, it is explained later in Subsection 3.2.1.3.

In order to reduce the number of input connectors, the LO is connected by one input channel and then split by an 8-way splitter. The chosen splitter is the ZN8PD-02183-S+ [34] by Mini-Circuits. It is sufficiently performant regarding isolation and amplitude unbalance between ports as well as return and insertion loss, which are shown in Table 3.1. The values are taken from the datasheet, but have also been confirmed with measurements. With the expected loss of 9 dB on each output port due to the splitting, less than 10 dB loss in total can be expected from the splitter, which is important for the power calculation needed for the LO.

3.2.1.1 Mixer

Main component of the X- to S-band conversion is an RF mixer. Being the most crucial part of the whole system, its selection and characterization must

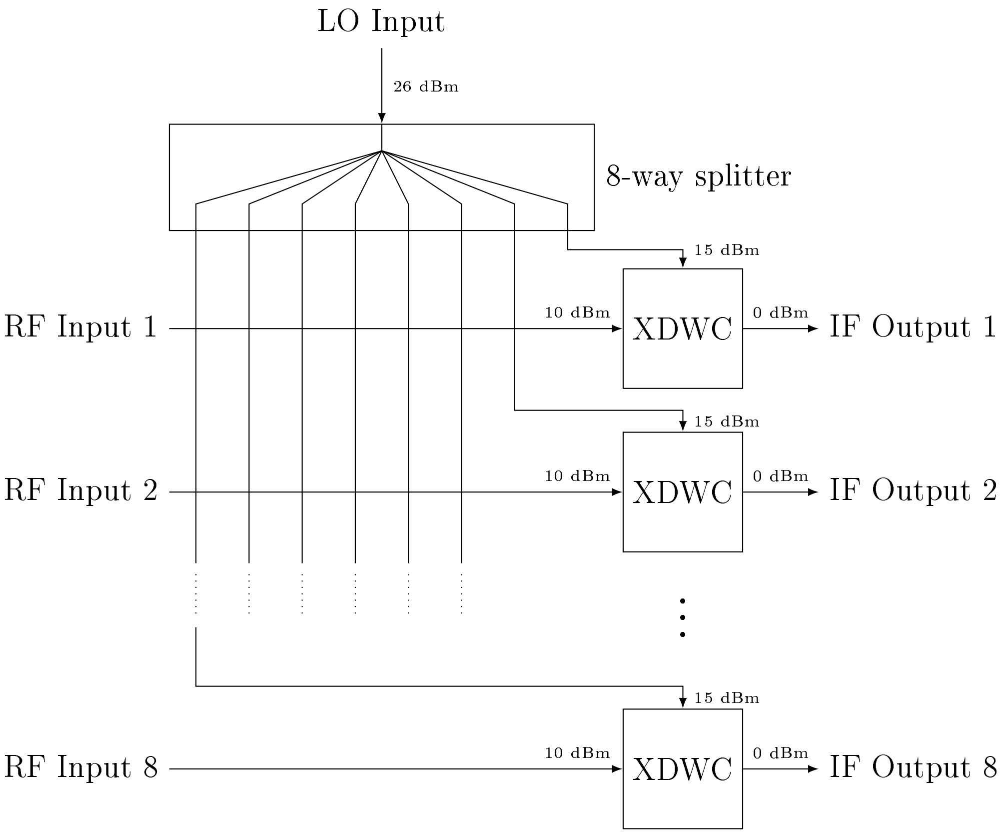

Figure 3.4: Schematic overview of the XDWCM.

be done carefully. With the knowledge of the most important properties of RF mixers described in Subsection 2.1.1, two candidates were selected for the X-band LLRF system: The SIM-193H+ [35] by Mini-Circuits and the CMD253C3 [36] by Custom MMIC. Both are double-balanced mixers built to be used for up- and down-conversion and are available in a surface mount package, which allows them to be placed on a PCB later. The mixer should

Isolation [dB]	≥ 28
Insertion Loss [dB]	≤ 1.5
Return Loss [dB]	≥ 17
Amplitude Unbalance [dB]	≤ 0.06
Phase Unbalance [deg]	≤ 2.75

Table 3.1: Electrical specifications of the ZN8PD-02183-S+ 8-way splitter at 12 GHz.

support an LO power level between 15 and 20 dBm and as much input power to have an output power of about 2 dBm when considering the conversion loss. The LO power is calculated from a maximum of 10 dBm input RF power, and thus the LO power should be at least 3 dB higher than that to not operate in saturation. In the end, the mixer CMD253C3 is chosen, as is explained in the following.

	CMD253C3	**SIM-193H+**
Conversion Loss RF-IF [dB]	**6.5**	7.5
Isolation LO-RF [dB]	**38**	37
Isolation LO-IF [dB]	**45**	15
Isolation RF-IF [dB]	**31**	30
LO power [dBm]	**15 - 23**	17 - 20
IIP3 [dBm]	**24**	23

Table 3.2: Specifications of the mixers CMD253C3 and SIM-193H+.

Table 3.2 shows the specifications for both mixers. From these, the CMD253C3 already has slightly better performance in conversion loss, IIP3 and isolation between the ports, especially for the LO to IF isolation. For the 1 dB compression and used LO power, the gain of both mixers was measured with the help of an evaluation board from the vendors. The measurements were taken doing conversions between 3 GHz and 12 GHz with a 9 GHz LO signal as shown in Fig. 3.5. The results are shown in Fig. 3.6. The mixer should work within the linear region at a reasonable LO power. What can be seen is the better conversion loss of the CMD253C3 as well as a slightly larger linear region. LO power of 15 dBm and a maximum input power of 10 dBm has been chosen for both conversion directions. 15 dBm has been chosen as it is still within the mixers specification while also providing the necessary output power. In addition, the XLOGM needs to provide the power for multiple channels, making higher levels harder to achieve. For up-conversion, the slightly worse linearity is not critical, as later on the drive signal power does not need to be that large.

3.2.1.2 Filter

Having 12 GHz and 9 GHz as inputs, harmonics are created as explained in Subsection 2.1.1 at every multiple of the difference of these two frequencies, in this case 3 GHz. As this is the lowest frequency and the desired result at the same time, low-pass filters can be used to get rid of the unwanted harmonics. When selecting the filter, one needs to consider, that most filter

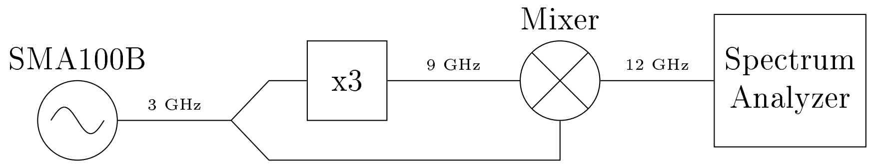

(a) Up-conversion Setup.

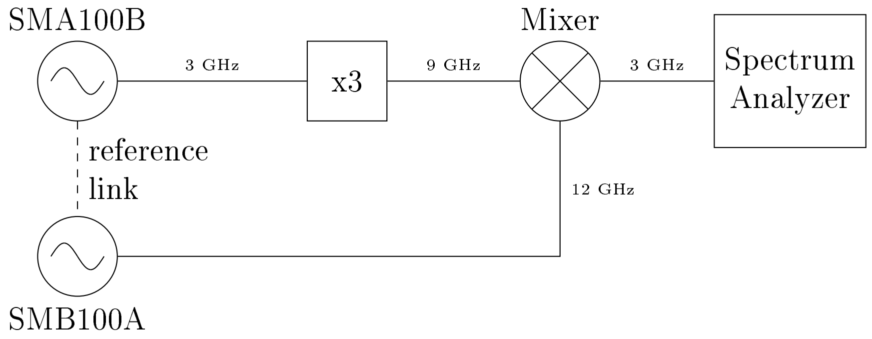

(b) Down-conversion Setup.

Figure 3.5: Setup of the mixer power sweep measurements.

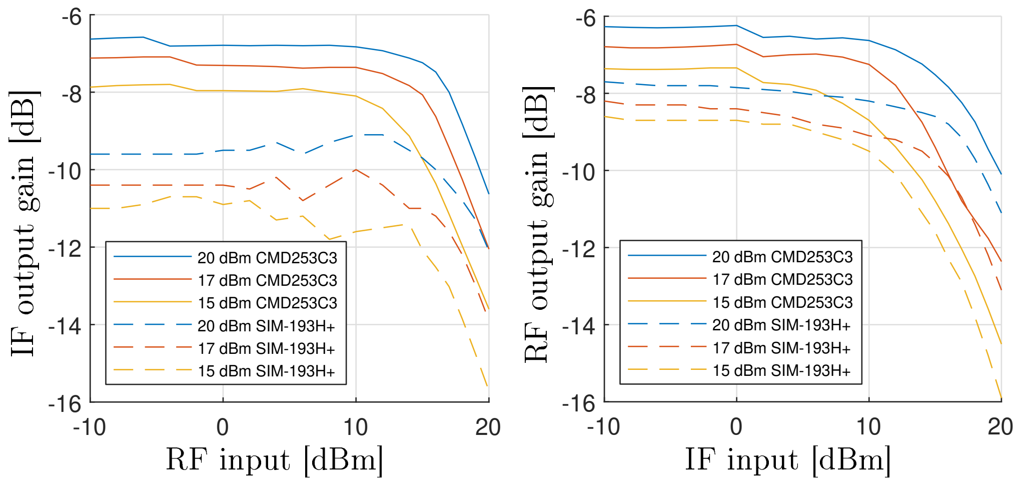

(a) Down-conversion. (b) Up-conversion.

Figure 3.6: Gain of the selected mixers in down- and up-conversion for various LO power levels.

types reflect stop-band signals back to its source. With the mixer being next to the filter, this would lead to all the filtered harmonics interfering with each other in the mixer. To prevent this, one needs to consider means to absorb the unwanted signals. The XLF-332+ [37] by Mini-Circuits is a low-pass filter that internally absorbs and terminates all stop-band signals, thus preventing them from getting back into the mixer. The downside of this approach is a slightly worse filtering performance. This can be solved by simply adding another filter behind the XLF-332+. For the second filter, the WE-LPF Multilayer Chip Low-Pass Filter[1] [38] by Würth Elektronik has been chosen. Table 3.3 shows the RF properties of these filters, highlighting the slightly worse performance of the XLF-332+. Although the WE-LPF is specified until 2.5 GHz, its performance at 3 GHz is still very acceptable with only 1 dB insertion loss compared to 0.5 dB it has at 2.5 GHz. The reason this filter has still been chosen becomes clear when explaining the PCB design in the next Subsection 3.2.1.3.

	XLF-332+	WE-LPF
Pass Band [MHz]	DC - 3250	DC - 2500
Attenuation @6 GHz [dB]	>15	>30
Insertion Loss @3 GHz [dB]	1.4	1

Table 3.3: Specifications of the filters XLF-332+ and WE-LPF 748125024.

Fig. 3.7 shows the spectra at each of the filtering stages. For better visual clarity, the spectra have been slightly shifted so each spike can be seen more clearly, the real values however are always at multiples of 3 GHz. Without any filter (shown in blue), all the harmonics from 6 GHz up to 24 GHz have relatively high power with up to -18 dBm at 9 GHz compared to 1 dBm power at the wanted 3 GHz. With the XLF-332+ filter (shown in red), the harmonics already get suppressed a bit down to -35 dBm at most. For better suppression, the WE-LPF filters the closer harmonics (6 to 12 GHz) down to -64 dBm and lower and only the higher harmonics (15 GHz and above) reach up to -60 dBm, which is a sufficient suppression.

In addition to the harmonic frequencies, a DC signal is also created in the mixing process. As some RF components may not be DC coupled and can be damaged when a DC signal is applied to them, it is better to also filter that out. As both filters mentioned above are DC coupled, the DC signal is not filtered by them. Instead they are blocked by a capacitor. For this, the 530Z [39] by American Technical Ceramics has been selected. Table 3.4 shows the

---

[1] There exist multiple form factors for this filter, for our application the filter with order code 748125024 was selected.

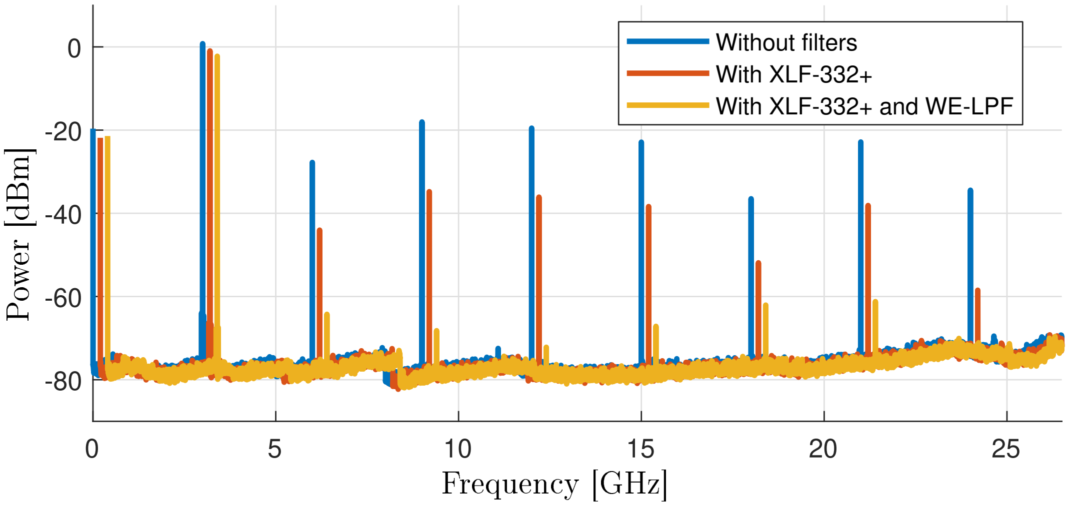

Figure 3.7: Spectra of the CMD253C3 after down-converting a 12 GHz signal down to 3 GHz with 9 GHz LO.

electrical properties of the capacitor. It is usable up to 20 GHz and uses low loss X5R dielectric which leads to an insertion loss of less than 0.1 dB at 3 GHz, about 0.1 dB at 9 GHz and about 0.2 dB at 12 GHz. Regarding the return loss, a value of less than -25 dB at 12 GHz and less than -35 dB at 9 and 3 GHz makes it a very good choice for the design. It is also available in the case size standard of the Electronic Industries Alliance (*EIA*) 0201, which is rather uncommon for this type of capacitor, but it becomes important for the PCB design.

	3 GHz	9 GHz	12 GHz
Insertion Loss [dB]	<0.1	0.1	0.2
Return Loss [dB]	-45	-33	-27

Table 3.4: Electrical properties of the ATC 530Z capacitor.

3.2.1.3 X-band Down-converter

First steps of designing the X-band Down-converter *XDWC* PCB are to select the substrate and materials to be used. As many other projects at DESY were done successfully using the RO4350B [40] substrate by Rogers Corporation, it is also used for the XDWC. As conductor material, copper and silver are the two candidates typically used for PCBs. Comparing the conductivity at room temperature, silver is slightly better with $6.3 \cdot 10^7$ S/m compared to

$5.9 \cdot 10^7$ S/m for copper. Taking into account the cost of these materials and the fabrication procedures, copper has been selected as conductor. In order to protect the copper, a surface finish must be applied to the PCB. As there exist many different finishes, each suitable for different applications, a comparison and selection must be done. The most critical requirements for the PCB are its Restriction of Hazardous Substances (*RoHS* [41]) compliance and the suitability for a relatively high frequency of 12 GHz. Additionally, its shelf life should be reasonably long. The most common finishes are listed in Table 3.5 with their main properties.

	Advantages	**Disadvantages**
HASL	• cheap • long shelf life	• uneven surface • contains lead
OSP	• cheap • lead free	• short shelf life
Immersion Tin	• flat surface • lead free • low losses	• short shelf life
Immersion Silver	• flat surface • lead free • low losses	• moderate shelf life
Hard Gold	• long shelf life • lead free • low losses	• expensive
ENIG	• lead free	• moderate shelf life • relatively expensive • high losses

Table 3.5: Most common surface finishes for PCBs.

Hot Air Solder Leveling (*HASL*) contains lead and has a very uneven surface resulting in high losses and Organic Solderability Preservative (*OSP*) as well as Immersion Tin have a very short shelf life of a maximum of six months, making storing and replacing broken PCBs impossible. Thus these finishes cannot be used. The other ones listed, Immersion Silver, Hard Gold and Electroless Nickel Immersion Gold (*ENIG*) all have a shelf life of at least six months, making them suitable regarding the shelf life. Hard Gold has been excluded from the candidates due to its cost compared with Immersion Silver and ENIG. Therefore, the two final candidates are Immersion Silver and ENIG. In [42], a thorough comparison of PCB finishes has been made regarding their frequency dependent performance. In conclusion, ENIG has much higher losses than Immersion Silver, which is why the latter has been chosen as surface finish.

With the materials given (RO4350B substrate, copper as conductor and Immersion Silver as finish), the next step is to layout the PCB. To maintain a good handling while keeping the PCB reasonably small, the outer dimensions were chosen to be 1"×1". The components have been chosen such that their pin width is (almost) the same at 0.3 mm, with the exception of the XLF-332+ at 0.23 mm. This has been done to reduce work, complexity and production cost of the conductor lines on the PCB, since for a too large difference from conductor line to pin width, the signal would see a huge jump in conductor width and as such would have a bad matching. Keeping all the pins at roughly the same size allows for a simple conductor line without changing its width towards the pins. With this in mind, a substrate thickness of 0.167 mm, conductor thickness of 1 oz and a conductor width of 0.33 mm are needed on the PCB to match a characteristic impedance of about 50 Ω at the three frequencies (3, 9 and 12 GHz) used on the PCB.

Fig. 3.8a shows the schematic of the XDWC, which can easily be realized on a single PCB layer. With each of the three ports processing a different frequency, one needs to consider the frequency dependence [43] of the losses on a PCB stripline: the higher the frequency, the higher the losses. Therefore, keeping the 12 GHz line short is one design rule. The final result of the PCB is shown in Fig. 3.8b.

As base layout, a standard two-layer microstrip PCB is chosen. The bottom layer is the uniform ground planes. On the top layer, in addition to the components and microstrip traces, ground planes are also placed with a large spacing to the traces to avoid interference. The planes are used to provide a better ground connection to the components compared to a connection with vias to the bottom layer. Looking closer at the mixer on the PCB as shown in Fig. 3.8c, the three outputs can be seen. To achieve a good isolation between the ports, two bridges are built from the top left and right edges of the mixer to the ground plane. To verify the design, a complete simulation with Ansys high-frequency structure simulator (*HFSS*, [44]) is performed. Focus of this is the matching and isolation of the mixer ports in a range from 1 to 20 GHz. The results can be seen in Fig. 3.9.

First of all, the S-parameters for the PCB input ports to the mixer inputs are simulated to validate the matching of the traces and components with the results shown in Fig. 3.9. The S-parameter plots show the return loss (S11 and S22) and the insertions loss (S21 and S12). In Fig. 3.9a the results show a very good matching for the RF input up to 18 GHz with more than 25 dB of return loss as well as less than 0.3 dB insertion loss at 12 GHz. Fig. 3.9b shows the S-parameters for the LO side. Also here a good matching up

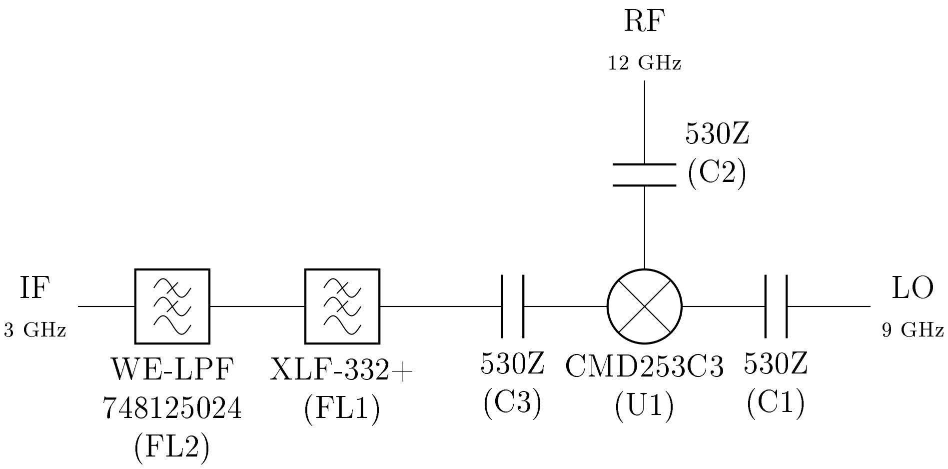

(a) Schematic of the XDWC.

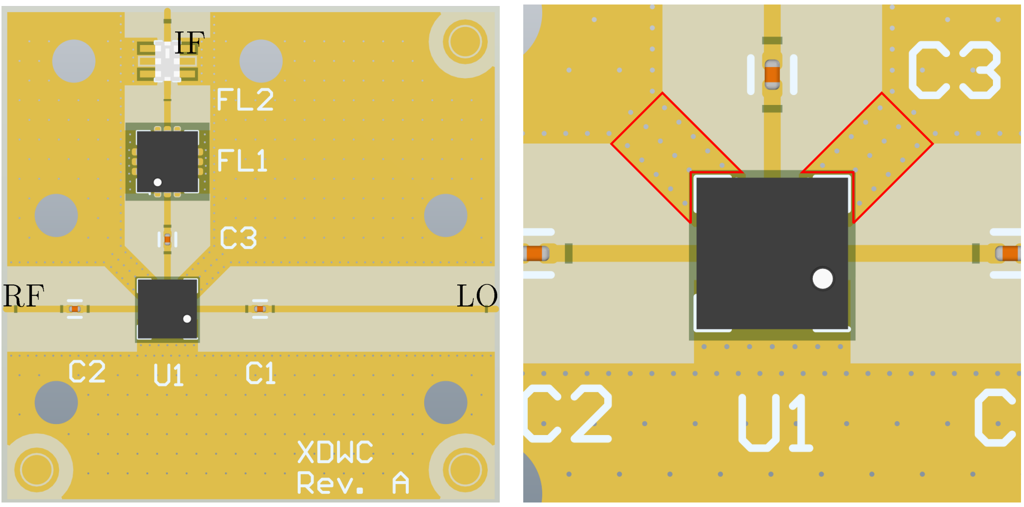

(b) Final design of the XDWC.

(c) Bridges (in red) near the CMD253C3.

Figure 3.8: Schematic and final PCB design of the XDWC.

to 18 GHz with less than 20 dB return loss and less than 0.3 dB insertion loss at 9 GHz is achieved. For the IF side shown in Fig. 3.9c, the filters are already included in the simulation. At 3 GHz, an insertion loss of 2.9 dB is achieved, this includes the losses of the filters. The return loss for both directions is less than 20 dB. At 6 GHz, the frequency of the first harmonic, an attenuation of 45 dB is already achieved. At 9 GHz and above, this is 57 dB or more. The S22-parameter for the IF side should be neglected, as the XLF-332+ is not unidirectional and as such disturbs the measurements. Fig. 3.9d shows the additional isolation due to the bridges to the ground plane. Compared to the isolation between RF and IF port of the mixer in the data sheet (31 dB), the design achieves 65 dB without and 66.5 dB with the bridges at 3 GHz. These values are 55 dB and 57 dB for 9 GHz and 54.5 dB and 56 dB for 12 GHz, respectively.

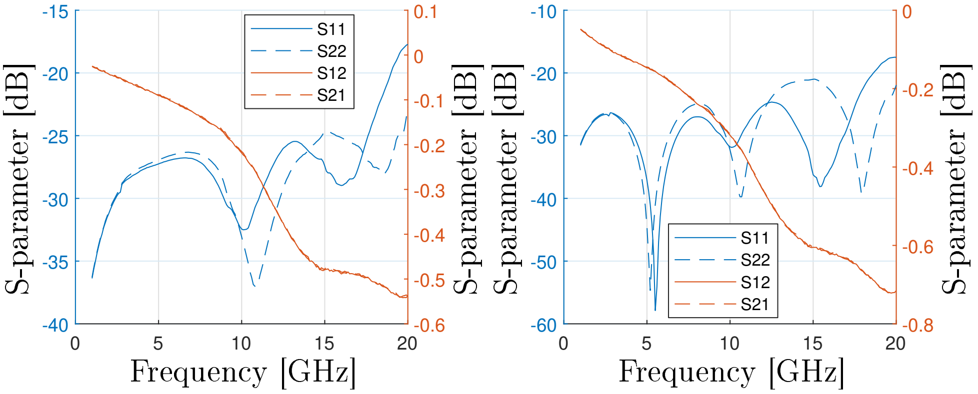

(a) RF input to mixer RF port.

(b) LO input to mixer LO port.

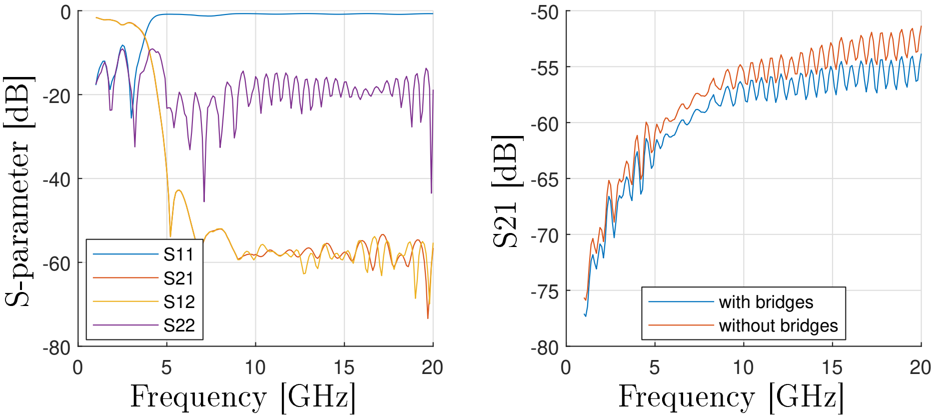

(c) IF input to mixer IF port.

(d) RF to IF coupling at the mixer ports.

Figure 3.9: HFSS simulations for the XDWC.

3.2.1.4 X-band Down-converter Module packaging

When installed at the accelerator, the whole system is to be put into a 19" rack. For this, everything needs to be packaged into fitting housings. For each of the eight PCBs in a module, a small, hermetically sealed housing is used to reduce the influence of temperature and humidity changes. This housing is shown together with the XDWC in Fig. 3.10a. Also shown are the three connectors (SMA864NLG-4.05-0.5 by Jyebao, [45]) which are mounted from the outside of the housing and then soldered to the PCB traces. These connectors are also hermetically sealed with a ring gasket to reduce air exchange over the connection hole. A rubber gasket is also laid onto the inner walls of the housing before mounting the cover to seal the top.

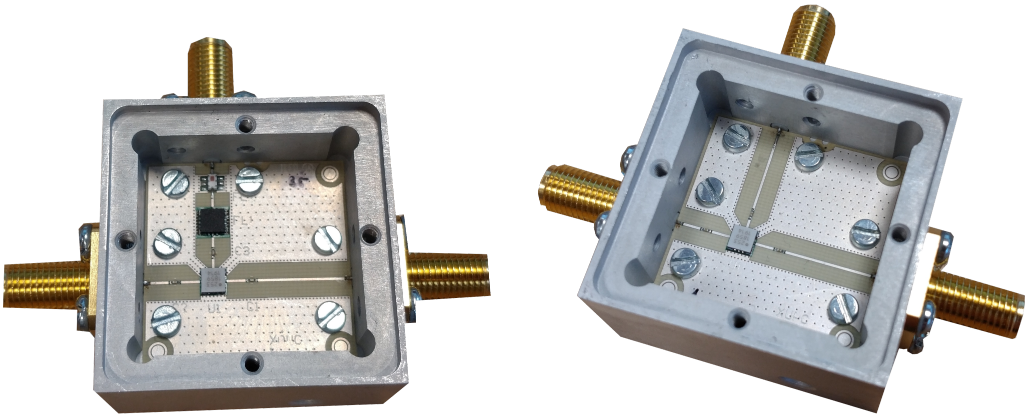

(a) XDWC in its open housing. (b) XUPC in its open housing.

Figure 3.10: XDWC and XUPC PCBs in their housing.

The eight XDWC in their housing are then packaged into a 19" module together with the 8-way splitter. To even further reduce the losses on the 12 GHz inputs, the connectors of the XDWC housings have been designed to fit through the connection holes in the 19" module. That way, no extra connector is needed for the 12 GHz inputs. The same has been done with the 9 GHz splitter input. Only the 3 GHz outputs require an additional connector on the 19" module. For this, the AD-A8A8-P4L [46] connector by Jyebao is used. The components were mounted and connected with A30A30-141HSA [47] semi-rigid SMA cables by Jyebao. The 19" module is called the X-band Down-converter Module (*XDWCM*).

3.2.1.5 X-band Down-converter Module with Up-conversion

As for now, the XDWCM can be used to down-convert 12 GHz to 3 GHz, which is used to measure incoming signals. As the LLRF system is also used to drive the RF field in the PolariX TDS, there needs to be a way to up-convert the 3 GHz signal to 12 GHz. As for this the same mixer as for down-conversion can be used, the X-band down-converter module with up-conversion (*XDWCM_UPC*) has been developed. It is a variant of the XDWCM which has one of the down-conversion channels replaced with an up-conversion channel. Fig. 3.11 shows the schematic overview of the XD-

WCM_UPC. One of the IF outputs now functions as input and instead of the XDWC PCB, the X-band up-converter (*XUPC*) is used.

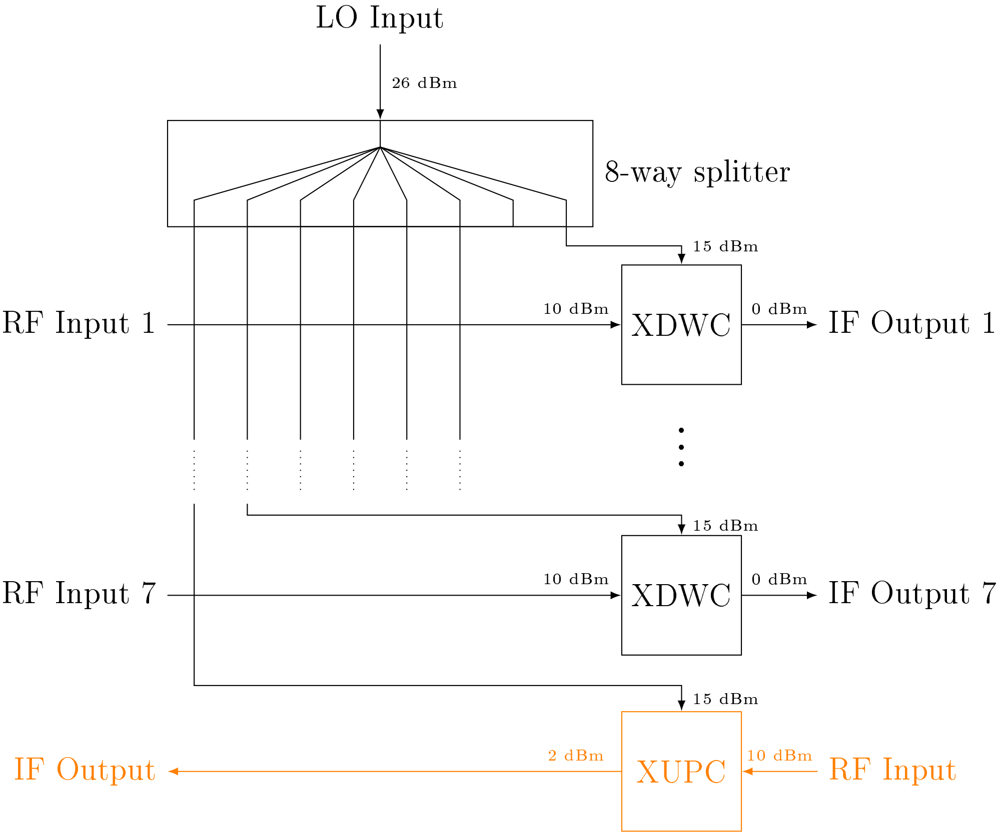

Figure 3.11: Schematic overview of the XDWCM_UPC.

The XUPC is basically the XDWC PCB, but without the 3 GHz low-pass filters. It is shown in Fig. 3.10b. Instead of 3 GHz low-pass filters on the PCB, a 12 GHz cavity band-pass filter (5IR10-12000/T1500-O/OP [48] by K&L) is used. This filter has a center frequency of 12 GHz, a 3 dB bandwidth of 1.5 GHz and an insertion loss of 0.6 dB. As it cannot be mounted on the PCB, it is later connected to the 12 GHz output. Fig. 3.12 shows the spectra of the RF output with and without the filter installed. The measurements are performed in the same way as for the down-conversion. A 15 dBm 9 GHz LO signal and a 10 dBm 3 GHz IF signal are used as inputs to the mixer and then up-converted to 12 GHz. 10 dBm input power is chosen as the DWC8VM1 can deliver up to 15 dBm, but considering the needed power inside the beam tunnel, 10 dBm is sufficient as explained in the next chapter. Compared to the filters on the XDWC, the cavity filter has a much higher attenuation in the stopband, leading to less than -70 dBm signal at all the harmonic frequencies. Except for the 9 GHz signal, which can be seen by a small margin, the noise floor of the measurement device (Rohde & Schwarz FSWP) is the limiting factor.

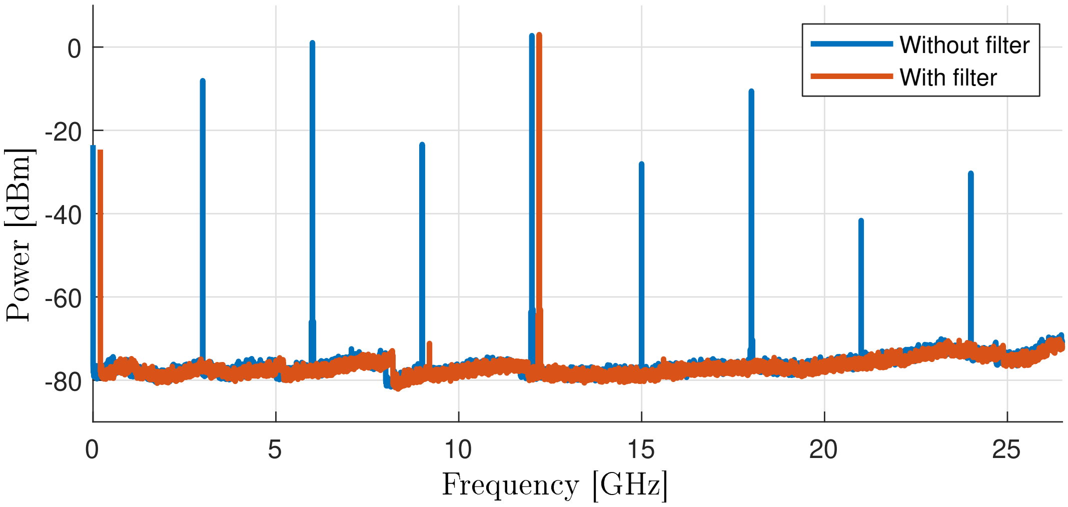

Figure 3.12: Spectra of the CMD253C3 after up-converting a 3 GHz signal to 12 GHz with 9 GHz LO.

The packaging for the XDWCM_UPC is the same as for the XDWCM, only the labels on the backpanel are different. As a comparison, the module is shown in Fig. 3.13 along with the front- and the two different backpanels of the XDWCM and XDWCM_UPC.

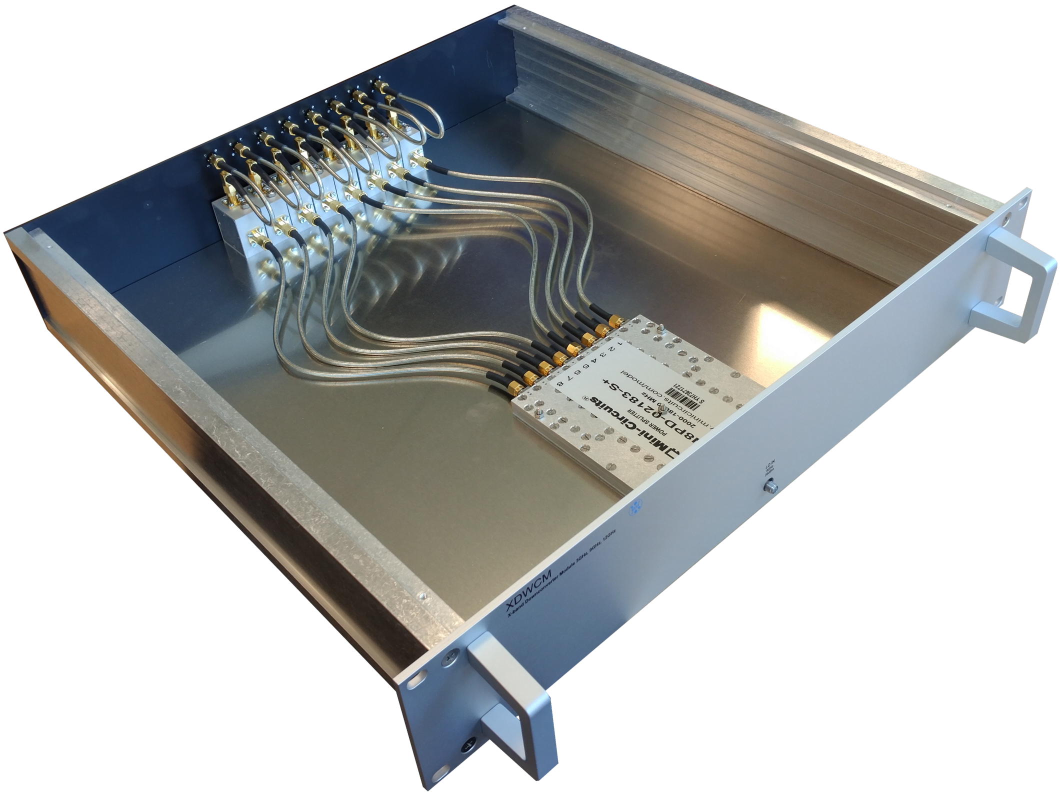

(a) XDWCM overview.

(b) XDWCM & XDWCM_UPC frontpanels (red).

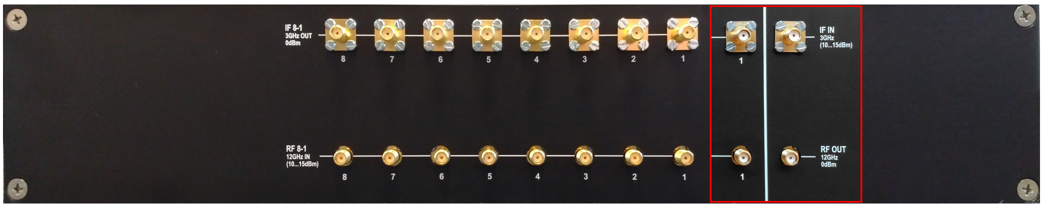

(c) XDWCM & XDWCM_UPC backpanels (red).

Figure 3.13: XDWCM overview and the front- and backpanels of the XDWCM and XDWCM_UPC (red).

3.2.2 X-band Local Oscillator Generation Module

As explained earlier, the mixers in the XDWCM need a 9 GHz LO signal with about 15 dBm power. With the reference signal of the whole system being 3 GHz, 9 GHz can be created by using a frequency multiplier. To supply multiple XDWCM with the LO signal, the X-band Local Oscillator Generation Module (*XLOGM*) uses a 4-way splitter to distribute it to up to four additional modules. As this requires a fairly high amount of power, the signal is amplified. As amplifiers are active components and to ensure a safe environment, control hardware is also built into the XLOGM. To avoid interference of power supply or control lines with the RF conducting parts, the XLOGM is split into two parts, one holding all the RF components and the other the control hardware. The first part consists of the frequency conversion as well as filtering, amplification and splitting of the resulting signal and is described in Subsection 3.2.2.1. The second (control) part is explained later in Subsection 3.2.2.2.

3.2.2.1 RF hardware

The RF part of the XLOGM needs to convert the incoming 3 GHz reference signal to 9 GHz that can then be used by the mixers in the XDWCM as LO signal. As usually eight channels that each XDWCM provides are not sufficient to operate a LLRF system, the XLOGM provides four outputs with enough power for the LO signal to support all of the eight channels per XDWCM for a maximum of 32 channels without additional hardware. For these steps, a dedicated, fixed frequency multiplier, filters, amplifiers and a 4-way splitter are used. The frequency multiplier, filters and amplifiers are explained in the following, for the splitter, the ZN4PD-02183-S+ [49] by Mini-Circuits has been chosen. It is similar to the 8-way splitter in the XDWCM and offers very similar electrical properties as shown in Table 3.6. Regarding the power levels, the 4-way splitter leads to a loss of about 7 dB. Including the 8-way splitter with about 10 dB loss, the total power output after amplification needs to be about 33 dBm to achieve 15 dBm power at the mixer input ports. A schematic overview of the RF part of the XLOGM is given in Fig. 3.14.

Frequency generation The frequency multiplier chosen is the RMK-3-123+ [50] by Mini-circuits. Fig. 3.15a shows the gain of said frequency multiplier. As can be seen, the linear region lies between 12 and 17 dBm input power. For the XLOGM, 13 dBm has been chosen as operating point marked by the black line. An overview of the important electrical properties

Isolation [dB]	≥ 25
Insertion Loss [dB]	≤ 1
Return Loss [dB]	≥ 19
Amplitude Unbalance [dB]	≤ 0.04
Phase Unbalance [deg]	≤ 0.75

Table 3.6: Electrical specifications of the ZN4PD-02183-S+ 4-way splitter at 9 GHz.

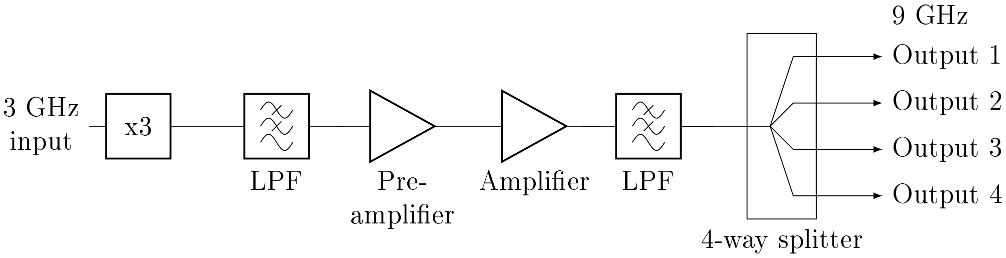

Figure 3.14: Schematic overview of the XLOGM's RF part.

is given in Table 3.7. Just as the mixer in the XDWCM, the multiplier creates various harmonic frequencies with different power. Especially the fundamental signal at 3 GHz is still very present with only 4.2 dB less than prior to the multiplication. The desired 9 GHz signal has a conversion loss of 15.5 dB. A band-pass filter is thus needed to get rid of the unwanted frequencies in the signal. For an easy production and packaging, the RMK-3-123+ is placed on a PCB with similar dimensions and materials as the XDWC and XUPC as shown in Fig. 3.15b called XLOG. For further protection, a DC-block of type BLK-18-S+ [51] by Mini-Circuits is installed at the input and output of the PCB.

Conversion Loss (9 GHz) [dB]	15.5
Harmonic Output (3 GHz) [-dBc]	4.2
Harmonic Output (6 GHz) [-dBc]	41.9
Harmonic Output (12 GHz) [-dBc]	52.0

Table 3.7: Electrical specifications of the RMK-3-123+ frequency multiplier at 3 GHz with 13 dBm input.

Filter To suppress the unwanted frequencies, a filter is installed. Similar to the XUPC, a cavity band-pass filter (TFWB-K-9G1.05G-SmSf [52] by

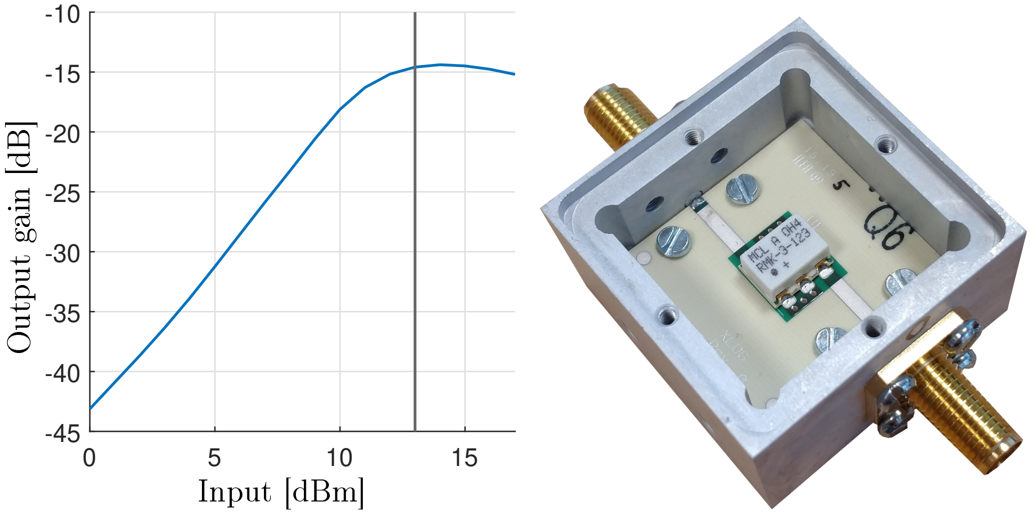

(a) Gain of the RMK-3-123+.

(b) XLOG in its housing.

Figure 3.15: Gain of the frequency tripler and the XLOG PCB in its housing.

Telemeter) with 9 GHz center frequency is used. It offers 1.05 GHz 3dB bandwidth and an insertion loss of at most 0.5 dB. In Fig. 3.16 the spectra of the RMK-3-123+ output with and without the filter are shown. The unwanted frequencies, especially the 3 GHz signal, is greatly suppressed down to less than -80 dBm while the 9 GHz signal looses almost no power. Only the 15 GHz harmonic is still present at about -40 dBm, which is handled later. The DC signal is filtered outside of the PCB by DC-block elements. As explained earlier, the LO port of each mixer in the XDWCM needs about 15 dBm power which results in about 33 dBm power needed for the 9 GHz signal which can only be achieved by using amplifiers.

Amplifier For the amplifying stage, a combination of low-noise pre-amplifier (A788) and low-noise power amplifier (A9G) from Laurin AG [2] is used. Fig. 3.17 shows the gain of each amplifier. For an output power of about 33 dBm, the A9G needs an input level of about 7 dBm. As the frequency multiplier and filter result in a power level of about -4 dBm, the pre-amplifier is needed and amplifies the input for the A9G to 7 dBm. On the downside, this amplification also results in higher levels of unwanted frequencies in the signal as shown in Fig. 3.18 in the blue line. The red line shows the spectrum after filtering showing no other signals than the 9 GHz. As explained before, the DC signal is taken care of by BLK-18-S+ DC-blocks.

---

[2] http://laurin-ag.com/

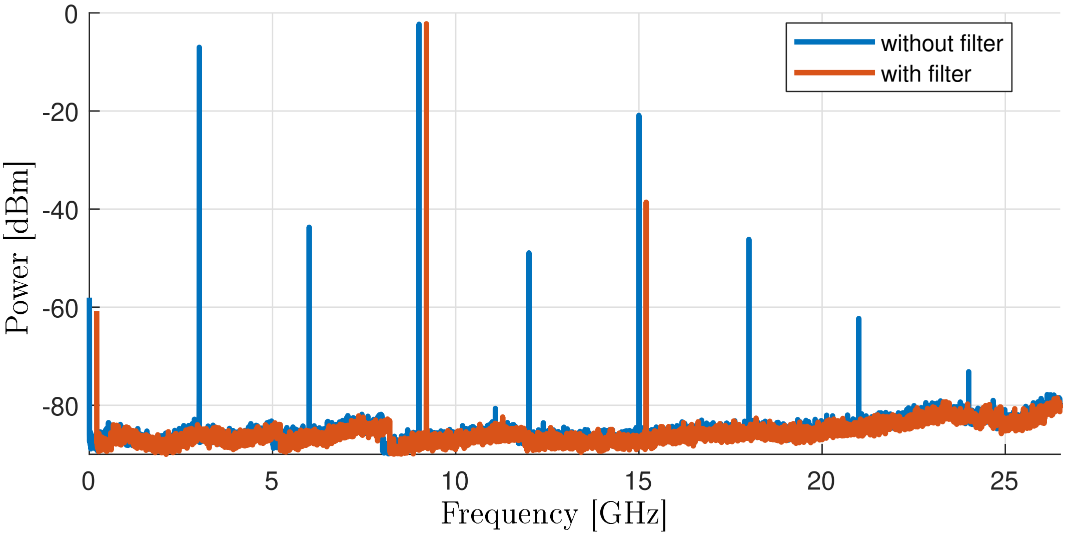

Figure 3.16: Spectra of the RMK-3-123+ before and after filtering.

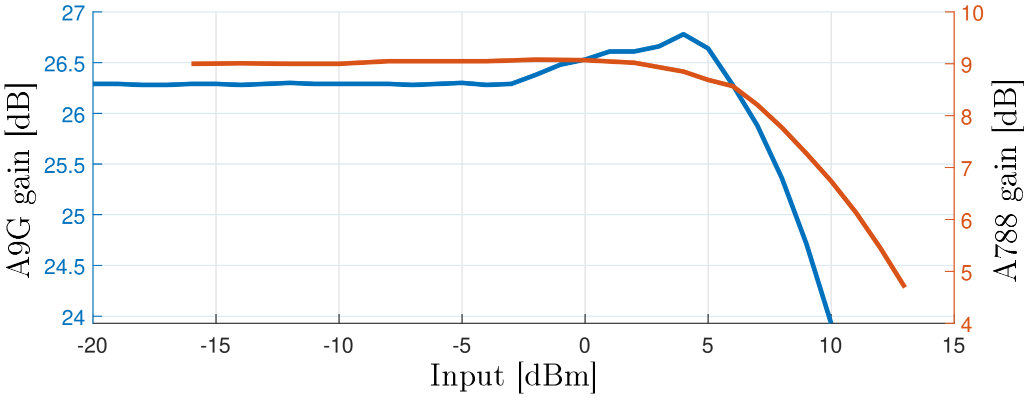

Figure 3.17: Gain of the amplifiers used in the XLOGM, blue: A9G, red: A788.

3.2.2.2 Control hardware

With a supply voltage of 15 V for both amplifiers and a power of up to 25 W, the ECL25US15-S [53] by XP Power handles the power supply of the A788 and A9G. Additionally, to avoid spikes of the power supply in voltage or current or other electromagnetic interference (*EMI*) related issues to have an impact on the RF signal, the Schaffner FN 2090 [54] EMI filter has been installed at the power supply's output. But as the amplifiers and with them the needed power supply are active components and the module should be able to run and restart itself autonomously in case of a power outage,

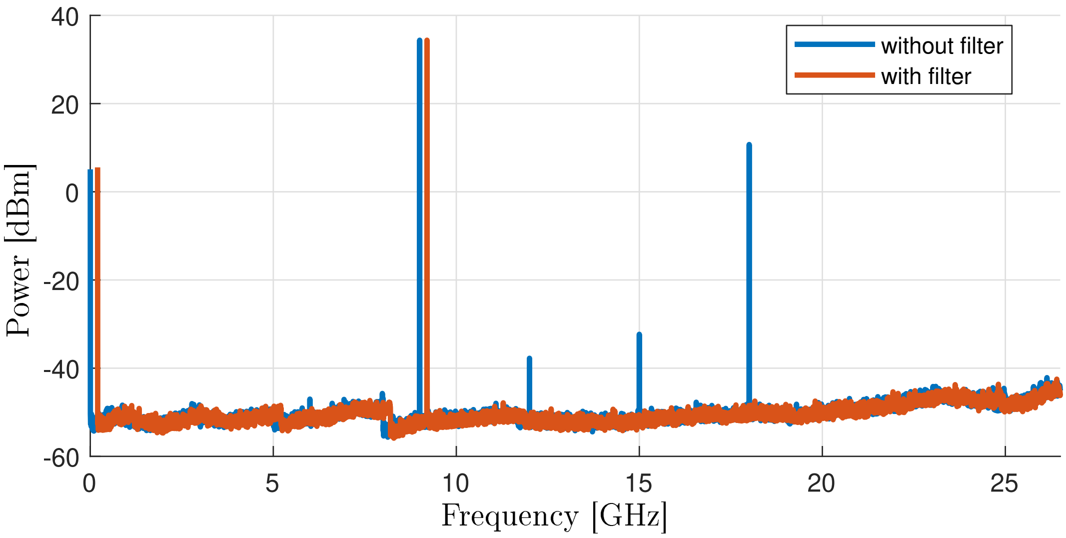

Figure 3.18: Spectra of the RMK-3-123+ with amplifiers before and after filtering.

additional hardware is required. For this purpose, the Fuse-Relay-Board (*FRED*, [55]) was developed at DESY. This board allows remote control and monitoring via Ethernet of up to eight DC voltages each with their own fuse and current limitation. Of these eight channels, only three are needed. One is for the 15 V of the amplifiers, the other two channels are used for the Temperature Monitor & Control Board (*TMCB*, [56]). This board is used for general purpose in various devices at DESY, providing 14 ADC, 10 DAC and 4 temperature read-outs as well as 20 GPIO channels. It requires a +15 V and -15 V power supply, for which the ECL30UD02-S [53] also by XP Power is taken. At this stage, the TMCB is not used in the XLOGM but has been built in for future updates of the system.

3.2.2.3 X-band Local Oscillator Generation Module Packaging

All the presented parts are then packaged into a 19" case which is split into an RF side and a control side as shown in Fig. 3.19a. The right side of the module contains the RF parts with the XLOG, DC-blocks, filters, amplifiers and the 4-way splitter. Similar to the XDWCM, the components are arranged in a way, that no further connectors on the module itself are needed. Instead, the connectors of the XLOG and splitter are fed through the case wall directly. All the components are placed on a single block heat sink, which is needed to dissipate the heat created by the amplifiers. For easier arrangement, the other components are also placed on it. The large heat sink also has the advantage in functioning as a temperature stabilizer, as a larger block takes longer to change its temperature. Separated by an aluminum wall for further EMI protection are the control parts on the left side of the module. These are the FRED mainboard on the backside, the two power supplies and the EMI filter in the middle as well as the TMCB and the FRED service board on the front side.

(a) XLOGM overview.

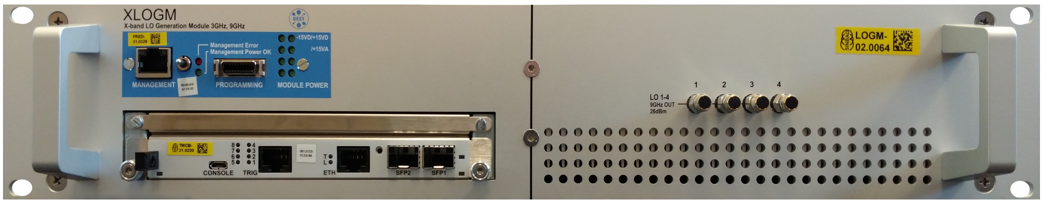

(b) XLOGM frontpanel.

(c) XLOGM backpanel.

Figure 3.19: XLOGM overview, the front- and backpanel.

3.2.3 Phase noise

To achieve the best results when operating the PolariX with an electron beam going through it, the phase of the RF field applied by the LLRF system needs to be as stable as possible. As explained in Subsection 2.2.3, an offset to the zero-crossing of the RF field would result in a kick of the beam instead of pure deflection. To verify the system, the phase noise of the modules has been measured. As the overall phase noise is heavily dependent on the quality of the source signal, the additive phase noise (APN, also known as residual phase noise) has been measured instead. Devices used for the measurements are the Rohde & Schwarz FSWP [57] for the phase noise and the Rohde & Schwarz SMA100B [58] and SMB100A [59] as signal generators. Two setups of the device under test (DUT) are needed for all measurements. One of the DUTs functions as reference generator for the FSWP while the other is the actually measured one. This is needed for the in-phase / quadrature (I/Q) mixers inside the FSWP used to create the IF frequencies processable by the ADCs inside the device. A more detailed explanation of that principle can be found in [60] and more details about the setup of the FSWP can be found in [61]. The setups for these measurements are shown in Fig. 3.20. For the XLOGM measurement shown in Fig. 3.20a, the SMA100B provides the 3 GHz signal which is then processed in both DUTs and then measured in the FSWP. The up-conversion channel is also measured with only the SMA100B and the FSWP as shown in Fig. 3.20b. Here, the SMA100B functions as a source for the XLOGM, which creates the needed 9 GHz LO, but also serves as incoming signal for the XUPC. The XDWC needs an additional 12 GHz signal for the down-conversion. This is created by the SMB100A which is linked with the SMA100B to use the same internal reference signal. This setup is shown in Fig. 3.20c.

3.2.3.1 Specifications

For the PolariX setup at FLASHForward, specifications have been discussed and calculated beforehand by the operation committee and are based on experience with the TDS installed in the EuXFEL [62]. A too large jittering of the RF phase would negatively impact any measurements performed by moving the beam or only parts of it back and forth off the imaging screen and would bias any calibrations done. Therefore a reasonable tolerance for the RF jitter must be defined respecting the size of the screens, the field of view and the maximum expected streak with regards to a certain beam length. At the FLASHForward beamline, the latter is set to about 250 fs while the screen size is 29x36.5 mm^2 and the field of view can be set to a maximum

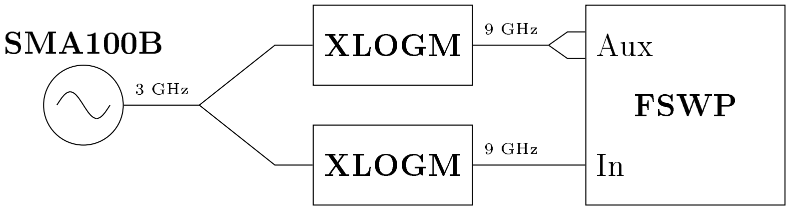

(a) XLOGM.

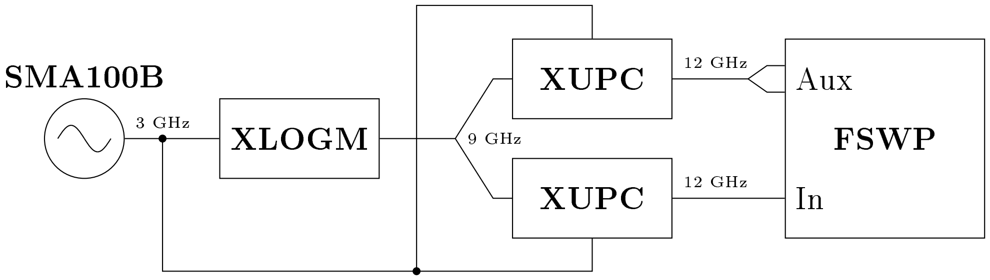

(b) XUPC.

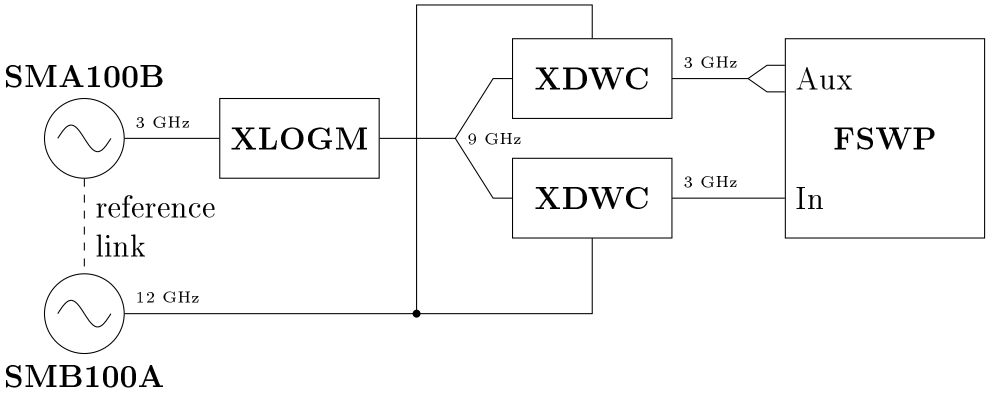

(c) XDWC.

Figure 3.20: Additive phase noise measurement setups for the XLOGM, XDWC and XUPC.

of 24x18 mm^2. With these parameters, 0.25° phase jitter was derived as a reasonable tolerance before severe biasing occurs. Since the PolariX TDS operates around the zero crossing of the RF phase, the amplitude noise is not a critical factor. However, a rough estimation for the amplitude noise has been made based on the typical stability of modulators on the market at that time, resulting in 1% requirements. An overview of the specifications is given in Table 3.8. For long-term phase stability, the noise can be a factor of ten worse, meaning 2.5° phase drift. Converting the phase values to the time domain related to 12 GHz, this would mean a short-term RMS jitter of about 58 fs and a long-term drift of about 580 fs is required.

	Phase		**Amplitude**
Short-term	0.25°	57.87 fs	1%
Long-term	2.5°	578.70 fs	1%

Table 3.8: Specifications for the stability of the PolariX TDS in FLASHForward as seen by the beam related to 12 GHz.

3.2.3.2 Measurements

As the PolariX runs at 12 GHz, all the phase noise values are related to this frequency. The result of the additive phase noise measurements can be seen in Fig. 3.21. From the measurements in Fig. 3.21b, the additive timing jitter can be calculated by integrating which is shown in Fig. 3.21a where the integration has been done from the right to the left. This results in the jitters listed in Table 3.9. When running the accelerator, these values do not take into account all the other components that are part of the actuator chain which contribute to the overall phase noise that the beam sees in the RF field inside the cavity. This is explained more thoroughly in the next section. However, these values can help to find unusual increases in overall noise, since it is known how much noise each individual part adds. Additionally, the 3 to 12 GHz conversion remains far below the specifications and does not take a critical role in the overall phase noise.

Module	Additive Timing Jitter [fs]	Additive Timing Jitter [m°]
XLOGM	1.434	6.195
XDWC	0.371	1.603
XUPC	0.278	1.201

Table 3.9: Additive phase noise of the modules related to 12 GHz.

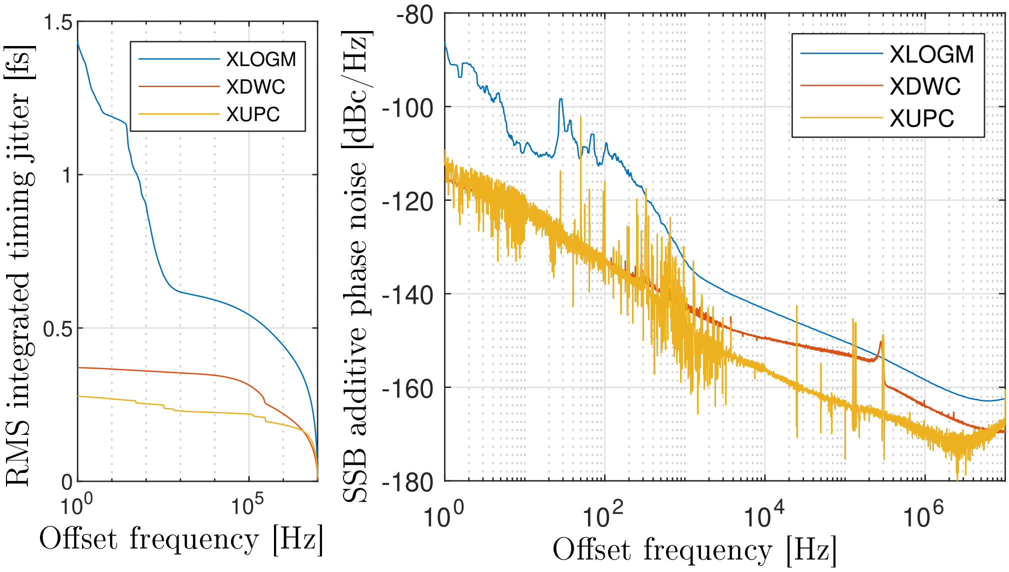

(a) Timing jitter.

(b) Additive phase noise.

Figure 3.21: Phase noise analysis of the XLOGM, XDWC and XUPC channels.

3.3 Summary

The design and setup of the X-band LLRF system for the PolariX TDS has been described in this chapter, including first measurements in the laboratory. The existing parts have been considered and explained. These were the UniLOGM, the MicroTCA.4 S-band LLRF system and the frequency generation box. Three new 19" modules have been developed, the X-band LO generation module XLOGM, the X-band down-conversion module XDWCM and the X-band down-conversion module with up-conversion XDWCM_UPC. The RF parts of these new modules were selected and characterized, especially regarding the phase noise, before being put together. As harmonics are created by RF mixers and frequency multipliers, filters were introduced to isolate the desired signal frequency. For the modules, new PCBs with the selected components have been designed, produced and packaged into housings. The measurements of the assembled modules showed an additive phase noise of 1.4 fs for the XLOGM, 0.37 fs for the down-conversion channel and 0.28 fs for the up-conversion.

Chapter 4

Commissioning

This section describes the setup for the PolariX prototype in the FLASHForward beamline with the goal to give an overview of the facility and beamline. The commissioning of the prototype setup is explained and first measurements are reported [63]. The measurements are used to verify the specifications and give a more in-depth understanding of the RF inside the cavity.

4.1 FLASH

Fig. 4.1 shows the FLASH facility with its three beamlines FLASH1, FLASH2 and FLASHForward. The PolariX TDS is positioned at the end of FLASH2 and FLASHForward. At first, only FLASHForward contains the PolariX prototype where it has been conditioned, successfully commissioned and is now in user operation. The setup in FLASH2 will be installed in the future and is explained later. Also included in the figure is the setup for both beamlines, the barrel-open cavity (*BOC*) and the RF switch, which is needed to operate both beamlines with the same RF source. The RF source, which is the LLRF system, and the modulator for the klystron are located in a corridor outside of the tunnel to have an easier access for maintenance and less problems due to radiation inside the tunnel. Other systems necessary to run the accelerator like the vacuum or water system have been left out as they are not part of this thesis.

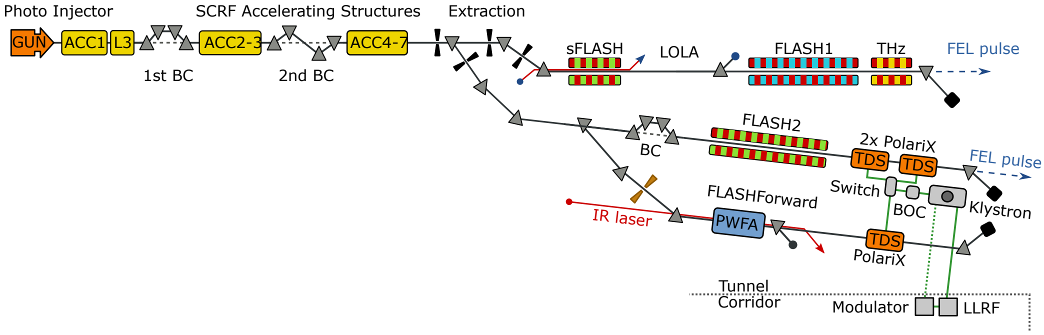

Figure 4.1: The FLASH facility including all three beamlines with PolariX TDS at the end of FLASHForward.

The first setup of the PolariX TDS is placed at FLASHForward and is installed towards the end of the beamline. The source of the 12 GHz RF that is applied to the cavity is the MicroTCA.4 LLRF system introduced in Chapter 3. The LLRF setup is shown in Fig. 4.2. The up-conversion channel from the XDWCM_UPC, which provides the drive signal, is connected to a pre-amplifier (AM61-12S-60-56PR [64]) followed by the klystron (E37113.A [65]). Following the klystron and connected via a waveguide system is the setup as explained before in Subsection 2.2.4 (Fig. 2.10). The RF is split into two parts, one going through a variable phase shifter and the other staying unchanged. Both of these parts are then recombined in the launcher, providing the variable rotation of the RF field in the PolariX cavity. The RF travels through the cavity and is then coupled out via another of the launchers and then dumped into loads.

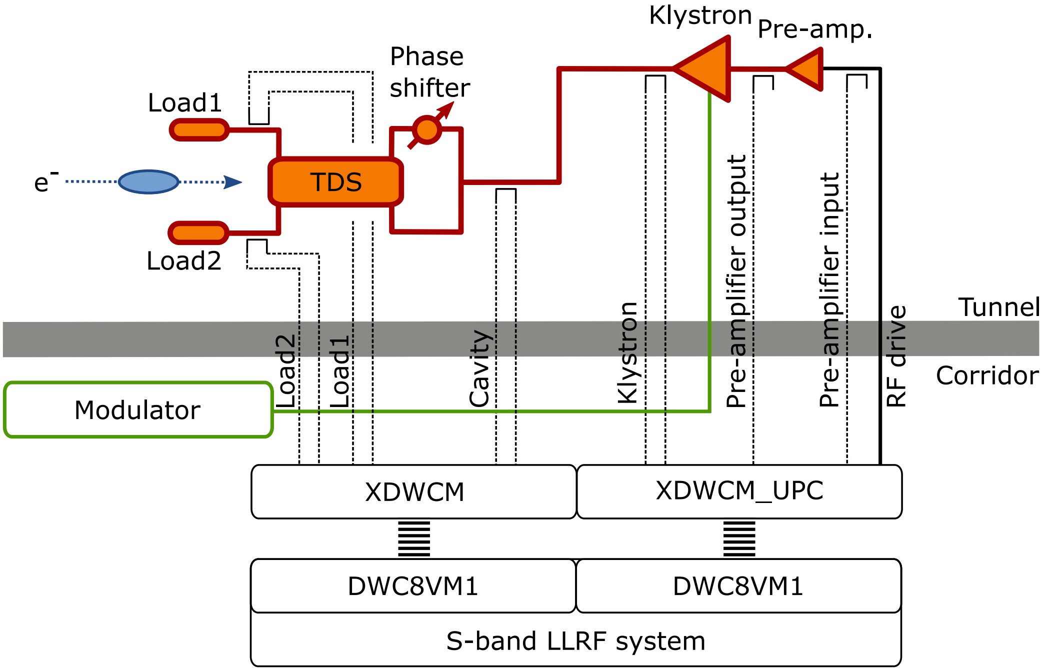

Figure 4.2: The LLRF system of the FLASHForward setup for PolariX.

Also shown in the figure are the couplers used to measure the 12 GHz RF signals of the actuator chain at various points in the system. These are before the pre-amplifier, before and after the klystron, before the splitter for the two launcher inputs as well as before each of the loads. To measure forward and reflected power, 12 down-conversion channels would be needed. For simplicity and almost no expected reflected power, the couplers before and after the pre-amplifier only provide the forward signal. The reflected signals are measured for monitoring false behavior, in case something breaks. The remaining signals are separated into a "source" section and a "cavity" section. The source section contains the four signal around the pre-amplifier and klystron and are connected to the XDWCM_UPC, as the drive signal can be seen as part of the source section. The signals in the cavity section are all those that are tied to the cavity: in front of the phase shifter and the loads. This is also shown in Table 4.1. This distribution has the advantage that each module has spare channels in case a channel breaks, but it is also modular. Adding more cavities, which is what happens when FLASH2 gets PolariX, the cavity section can be copied without changes from a hardware point of view. Only internally, the signals need to have unique names.

The measured signals need to be converted via the XDWCM or XDWCM_UPC and digitized by the S-band LLRF system to observe them and

	Source section	**Cavity section**
Connected to	XDWCM_UPC	XDWCM
Signals	• RF Drive (up-conversion) • Pre-amplifier input forward • Pre-amplifier output forward • Klystron forward • Klystron reflected	• Cavity forward • Cavity reflected • Load1 forward • Load1 reflected • Load2 forward • Load2 reflected

Table 4.1: Distribution of the measured 12 GHz signals in the LLRF system.

allow control algorithms to stabilize the drive signal. The MicroTCA.4 system is build such that each board (DWC8VM1 and SIS8300L2) supports up to eight channels, the same holds for the XDWCM and XDWCM_UPC. This means each conversion module requires one DWC8VM1 and SIS8300L2 to support all channels for the prototype setup.

4.2 Measurements

All measurements so far have been done in the laboratory with the isolated modules. Once the PolariX TDS and the required systems are installed, conditioned and successfully commissioned, measurements can be made at the accelerator. From an operators point of view, the stability in regards to what the electron beam sees is important. Large amplitude instabilities cause uncertainties in regards to the streaking strength, which ultimately can cause the beam to not hit the screen in its current field of view or go out of the screens borders. Phase jitter results in uncertainties of the streaking angle and cause a small kick to the beam, leading to large fluctuations of the image on the screen. Phase drift on the other side causes calibrations of the screens to be invalid after a short time, causing a lot of overhead work or even unusable results if the calibration is falsified too fast. To verify the stability of the RF and the beam, measurements have been taken and analyzed regarding the specifications discussed in Subsection 3.2.3.

In order to differentiate between short- and long-term effects, the data needs to be processed to get rid of the unwanted parts. For short-term analysis, the jitter is determined by calculating the standard deviation of the data. If long-term effects are still present, the calculation is biased due to the drift. Two algorithms for compensation have been applied and compared. For this, 22606 pulses have been recorded at FLASHForward over the course of about 40 minutes with a 10 Hz repetition rate. As data, the RF signal at the klystron output has been taken. The first algorithm is a 5th-order butterworth high-pass filter (HPF) with a cut-off frequency of 0.2 Hz. The transfer function of the resulting filter is

$$H(z) = \frac{B(z)}{A(z)} = \frac{b_1 + b_2 z^{-1} + ... + b_6 z^{-5}}{a_1 + a_2 z^{-1} + ... + a_6 z^{-5}}$$

with the coefficients listed in Table 4.2.

i	**1**	**2**	**3**	**4**	**5**	**6**
$\mathbf{b_i}$	0.8159	-4.0794	8.1588	-8.1588	4.0794	-0.8159
$\mathbf{a_i}$	1	-4.5934	8.4551	-7.7949	3.5989	-0.6657

Table 4.2: Filter coefficients for the 5th-order butterworth high-pass filter with cut-off frequency 0.2 Hz.

The second algorithm is a least-squares fit (LSF) of a piecewise linear function to the data with each part using 25 data points, which corresponds to the cut-off frequency of 0.2 Hz used for the filter. This functionality is implemented in the `detrend` function in MATLAB. Shown in Fig. 4.3a are the 22606 pulses at the klystron output as sampled by the LLRF system with 125 MHz. From each of these pulses, the mean over the stable flattop area of the pulse (between the vertical lines) has been taken and represents one point in Fig. 4.3b. For better comparison, the mean of the data has been subtracted from each data point.

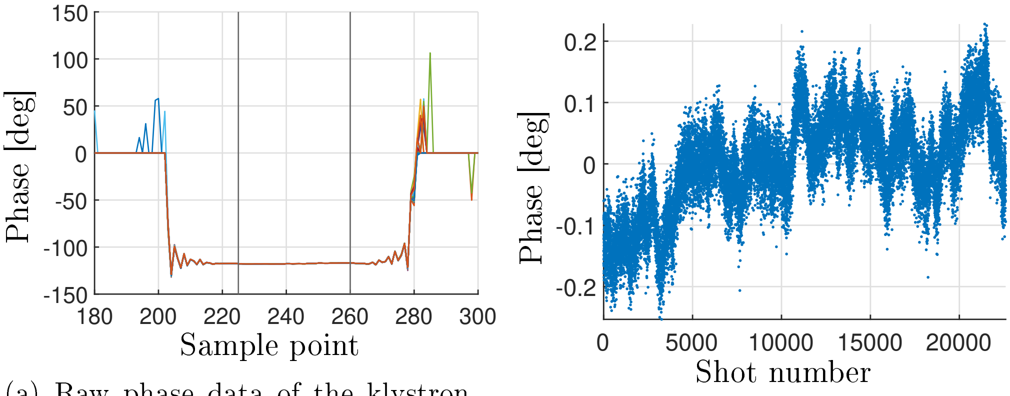

(a) Raw phase data of the klystron output measured in the LLRF system.

(b) Mean over the flattop of each pulse at 10 Hz repetition rate

Figure 4.3: RF pulse shape and region of interest with the derived mean over each pulse.

Seen are long-term effects that would distort the short-term jitter calculation over the whole dataset. In Fig. 4.4, both algorithms for compensation are shown, with the filter algorithm in Fig. 4.4a and the least-squares fit in Fig. 4.4b.

In the time domain, as shown here, no real difference can be seen and both algorithm produce almost the same result with no long-term effects noticable anymore. For a better insight, a comparison in the frequency domain has also been made. For this, the fast Fourier transformation (FFT) has been used and the power spectral density (PSD) calculated and plotted in Fig. 4.5.

As seen in Fig. 4.5, none of the algorithms has an influence on the signal above the cut-off frequency at 0.2 Hz. Below that, the high-pass filter (red) has a slightly steeper slope compared to the least-squares fit (yellow). As final means of comparison, the RMS phase jitter of the signals for both algorithms has been calculated as the standard deviation and is shown in Table 4.3.

The effect of the compensation methods which drastically reduces the calculated short-term jitter can be seen. The difference between the two methods though is negligible, however during the calculations it became clear

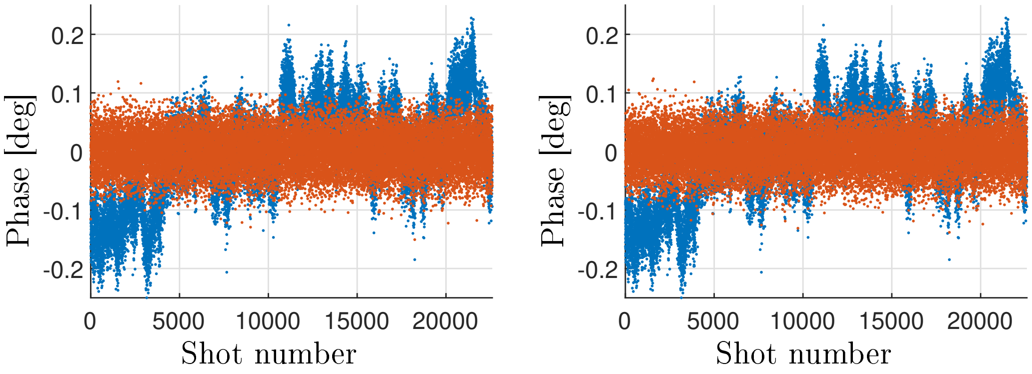

(a) High-pass filter.

(b) Least-squares fit.

Figure 4.4: Comparison of the long-term effect compensation algorithms in the time domain, blue: original data, red: compensated data.

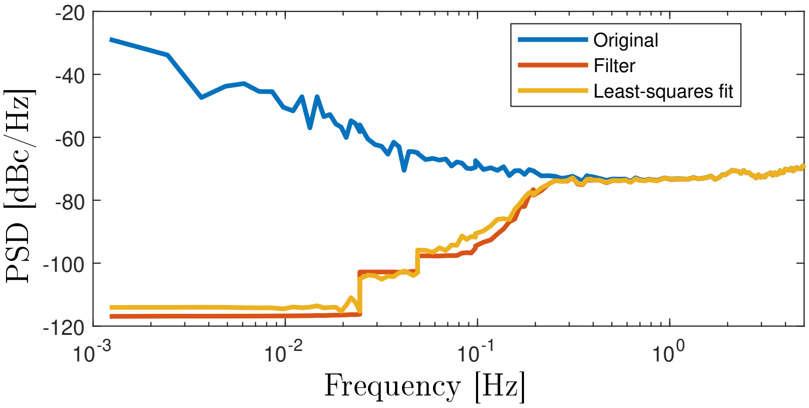

Figure 4.5: Comparison of the long-term effect compensation methods in the frequency domain.

	Phase jitter [m°]	Phase jitter [fs]
Raw	78.333	18.133
Filter	33.191	7.683
Least-squares	33.192	7.683

Table 4.3: Phase jitter comparison of both long-term effect compensation algorithms, related to 12 GHz.

that the filter is easier to apply and takes less time to calculate the result. Due to this, the filter method is taken in the following to analyze the results regarding the short-term behavior.

4.2.1 Actuator chain

At first, the most relevant RF signals are analyzed. These are the RF drive, pre-amplifier output and klystron output. In the current installation, the pre-amplifier input signal delivers too little signal power to be measured at all. This is explained by the output power of the RF drive signal, which comes from the vector modulator (VM) of the DWC8VM1 at 3 GHz and is then up-converted to 12 GHz and delivered to the pre-amplifier with about twelve meters of cable which contributes 9 dB attenuation. As the klystron reaches the desired output power of 6 MW (97.78 dBm) at 80 W (49.03 dBm) input power as shown in Fig. 4.6a, the pre-amplifier is only driven up to slightly more than 100 W (50 dBm), as from experience the amplitude noise is reduced when operating a klystron in saturation. According to the power sweep done with the pre-amplifier in Fig. 4.6b, a maximum of -22 dBm input power for the pre-amplifier fully saturates the klystron. For measurements, a 3-dB-splitter is installed in front of the pre-amplifiers input and with 9 dB additional attenuation, the maximum power the signal has back at the input of the XDWCM_UPC is -34 dBm. With about 10 dB conversion losses from the mixer and filters, only -44 dBm reach the DWC8VM1. Also, both the pre-amplifier and klystron do not show a linear behavior.

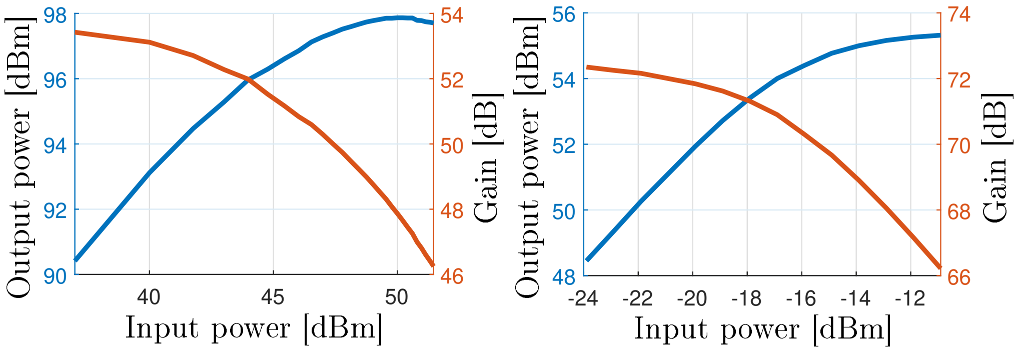

(a) Klystron. (b) Pre-amplifier.

Figure 4.6: Power sweep and gain of the E37113.A klystron and AM61-12S-60-56PR pre-amplifier.

Shown in Fig. 4.7 are the vector modulator (VM), pre-amplifier (PA) and klystron output signals. As described above, 22606 pulses were measured with a repetition rate of 10 Hz, sampled with 125 MHz and the mean over the flattop of each pulse represents one data point. The raw data is shown in blue. The same filter as above is applied to each of the signals and the result is plotted in red. The VM signal is measured internally by the MicroTCA.4 system while the other signals are sent over a cable into the XDWCM, down-converted and then digitized and measured. Even for the VM signal, a small phase drift can be seen (blue) which is compensated by the filter.

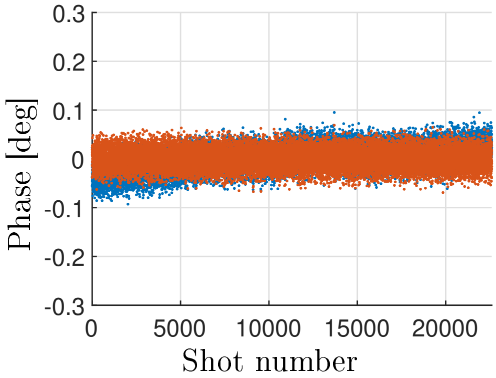

(a) Vector modulator.

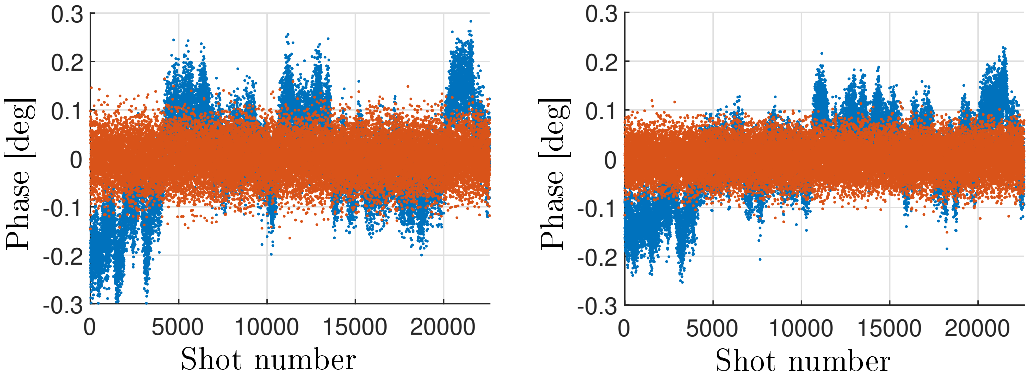

(b) Pre-amplifier output.

(c) Klystron output.

Figure 4.7: Phase signals of the vector modulator, pre-amplifier and klystron output, blue: original, red: filtered.

The increase of the spread of the data points compared to the VM signal can be seen in Fig. 4.7b and 4.7c. Also a slightly larger spread of the PA signal compared to the klystron can be seen. Calculating the RMS jitter as the standard deviation delivers the results in Table 4.4. While in the VM signal, only the small long-term drift needs to be compensated, the phase jitter value only slightly changes from 5.7 to 4.4 fs. At the PA and klystron signals, the need for the compensation can be seen. The PA signal's original phase jitter including long-term effects is 22.7 fs while the compensated value is only 9.3 fs. The same holds for the klystron signal, which decreases from 18.1 to 7.7 fs of phase jitter. While the jitter can only increase with more active components in the chain, the phase jitter at the klystron output is actually smaller than at the pre-amplifier, which leads to the conclusion that the PA values can only be taken as an upper boundary.

Signal	Phase jitter (filtered) [m°]	Phase jitter (filtered) [fs]	Phase jitter (original) [m°]	Phase jitter (original) [fs]
VM	18.959	4.389	24.590	5.692
PA	40.148	9.293	97.950	22.674
Klystron	33.191	7.683	78.333	18.133

Table 4.4: Phase jitter values of the actuator chain, with and without compensation, related to 12 GHz.

At first it seems unusual that the phase noise after the pre-amplifier is larger than after the klystron, as the klystron can only add more noise and not reduce it. Two possible sources of this are the ADCs in the LLRF system that might be driven with too little power and a difference in the bandwidth of the pre-amplifier and klystron.

4.2.1.1 ADC drive

The first idea for an explanation of this phenomenon was directed to the ADCs on the DWC8VM1 boards and the power levels at the inputs driving the ADCs. The signal after the pre-amplifier is coupled out with a 30 dB-coupler and passed to the XDWCM channel with a cable that causes about 9 dB additional attenuation. At 100% streaking strength, the output of the pre-amplifier is about 50 dBm as stated above, the 39 dB losses would reduce the power to 11 dBm at the XDWCM inputs. The down-conversion channels themselves each have a conversion loss of about 10 dB resulting in only 1 dBm at the DWC8VM1 inputs. At lower drive levels, this is even less. The measurements above were made at 60% streaking power. To verify the percentage at which the ADC is driven the measured amplitude is divided by the number of values the ADCs can represent, which is 2^{18}. As the numbers are represented in signed values, the actual range for positive values is $2^{17}-1$ and the drive can be calculated as

$$d_i = A_i * B/(2^{17} - 1) \tag{4.1}$$

with B being the bit scaling factor used in the LLRF system to scale the measured amplitudes. For these measurements, this was set to 1310 resulting in $1310/(2^{17}-1) = 0.01$ and as such the measured amplitude value represents the percentage the ADC is driven with. The results for all measured signals is listed in Table 4.5.

Signal	**Amplitude [arb. units]**[1]
VM	31.31
Pre-amplifier	10.70
Klystron	47.01
Cavity	63.38
Load1	32.89
Load2	29.66

Table 4.5: Amplitudes of the measured signals, representing the percentage at which the ADCs in the DWC8VM1 are driven.

The pre-amplifier signal strength is thus only 10% of the maximum drive for the ADCs while good practice says to be in the region of 70-90% to not overdrive the ADCs and have enough quantization steps for precise measurements. While lower values, as measured here, can still be used, quantization steps might distort the results. In order to verify the results, a second measurement has been done sweeping the setpoint for the klystrons output power from 20% to 100% in steps of 20%. As described above, the LLRF system measures the signals coming in from the RF couplers, it also measures the vector modulators output and has a channel to read the reference signal. The latter is implemented such that the ADC converting the signal is fully driven. As such, this channel does not suffer from too few quantization steps and can be used to measure a change of the noise contribution of other channels. To do this, the reference channel is set to the same amplitude of the to-be-measured channel with a variable attenuator. This principle is used in the above mentioned verification measurement and, from the measured signals, the coefficient of variation c_V can be calculated. c_V is a quantity to measure the scattering or dispersion of a signal and is calculated by dividing the standard deviation σ of a signal by its mean μ

$$c_V = \frac{\sigma}{\mu}. \tag{4.2}$$

---

[1] The amplitude values do not represent any physical quantity, thus it has an arbitrary unit.

Being standardized to the actual amplitude by dividing by the mean, an increase of c_V means the standard deviation or in case of the RF signals the RMS and as such the noise is also increasing. For the above mentioned measurement, a c_V in the same order of magnitude for all setpoints would mean the signals are driven equally well. The results are shown in Fig. 4.8.

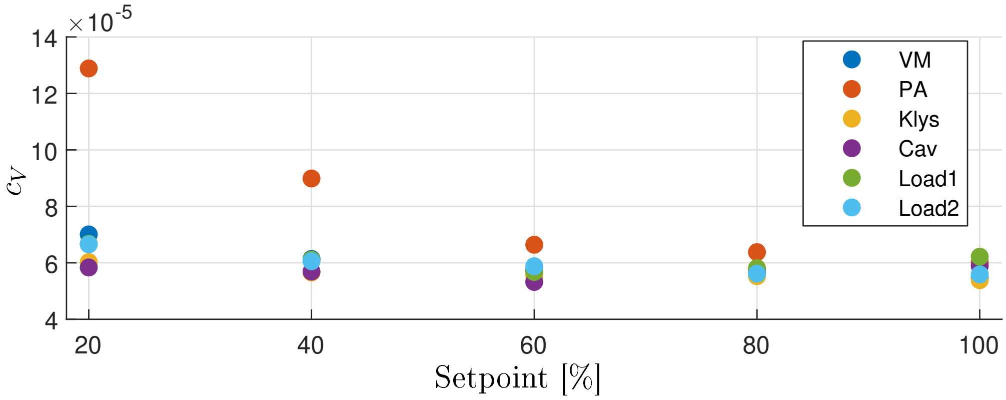

Figure 4.8: Coefficient of variation for the RF signals at various setpoints of the klystron output.

A steady c_V for all signals except for the pre-amplifier can be seen. At 20 and 40% amplitude setpoint, the $c_{V,\mathrm{PA}}$ differs from the others by a factor of about 2 and 1.5 respectively. Starting at 60%, $c_{V,\mathrm{PA}}$ only differs by a factor of 1.1 or less which can be interpreted as equally driven causing only marginal differences. On the other side, this measurement has disproved the first assumption, as the ADC for the pre-amplifier signal is driven well enough to deliver valid results and should only have a minor impact on the measured value.

Possible solutions to fix the issues with the power in both the input and the output signal of the pre-amplifier are already planned. For the input signal, a solution is to not pick the signal at the input of the pre-amplifier, but rather right at the LLRF system and feed it back into the measurement channel. That way, the losses of the cable would not come into account and a measurable signal would be present, although it would most likely still not fully drive the ADC. Another problem would be, that the signal cannot observe any disturbances that might happen on the way from the LLRF system to the pre-amplifier. For the output signal, a rather easy fix is to replace the 30 dB coupler by a 20 or 10 dB one and thus have more signal power at the LLRF system, which would be sufficient to fully drive the ADC.

4.2.1.2 Actuator bandwidth

The second approach for an explanation of the measured jitter values is found by looking into the specifications of the pre-amplifier and klystron. Here, a difference in bandwidth can be seen between the pre-amplifier (50 MHz) and the klystron (2 MHz). These are only the bandwidths as specified in the data sheets, the real bandwidth of both actuators are currently unknown. However, the specified bandwidths are used as an approximation of the real ones. Taking these bandwidths into account means the measured values in Table 4.4 are also related to that bandwidth. Calculating the difference of the bandwidths in dB yields

$$20 \cdot \log_{10}(\frac{\sqrt{50}}{\sqrt{2}}) = 14 \text{ dB}.$$

This means the different bandwidths cause a difference of about 14 dB in the measured noise. Assuming only white (broadband) noise and as such a flat power spectral density with amplitude A_N and bandwidth $\mathrm{BW} = f_2 - f_1$, the RMS jitter of a signal can be approximated by

$$\begin{aligned} \varphi_{\mathrm{RMS}} &= \sqrt{\int_{f_1}^{f_2} \mathcal{L}(f) df} \\ &= \sqrt{A_N \cdot \mathrm{BW}}. \end{aligned}$$

As non-white noise usually only occurs within a few hundred Hertz around the carrier, it can be assumed with 2 and 50 MHz respectively, that the majority of the contributing noise is actually white noise. With that, the measured jitter values from Table 4.4 can be compared to each other by dividing them by the square root of the bandwidth. In the logarithmic domain, this yields

$$20 \log_{10}(\frac{33.191}{\sqrt{2 \cdot 10^6}}) - 20 \log_{10}(\frac{40.148}{\sqrt{50 \cdot 10^6}}) = 12.33 \text{ dB}.$$

This 12.3 dB difference between the measured jitter values is relatively close to the 14 dB the difference in bandwidth alone is contributing to the overall noise. Hence it can be assumed the larger jitter value of the pre-amplifier compared to the klystron is caused by this.

4.2.1.3 Noise modeling

For a better understanding and traceability of errors, the additive noise values of each contributing part in the actuator chain is useful to know. The system can be modeled as shown in Fig. 4.9. The source signal of the model is the 3 GHz vector modulator output of the DWC8VM1. This is up-converted to 12 GHz in the XDWCM_UPC and then led to the pre-amplifier followed by the klystron. Each coupled-out 12 GHz signal also needs to be down-converted to 3 GHz in the XDWCM. Each actuator adds a certain amount of noise depicted by $\varphi_{\mathrm{X}}(s)$ in the model. The modeling is done in the s-domain by using the Laplace-transform. After the pre-amplifier and klystron, a low-pass filter is included which describes the limitation by the bandwidth. The vector modulator and converters all have several GHz of bandwidth which compared to the pre-amplifier and klystron can be neglected. The actual measurement points are indicated by the red circles. The VM signal ($\varphi_{\mathrm{VM}}(s)$) is measured internally and thus no noteworthy noise is added. The PA ($\varphi_{\mathrm{PA,out}}(s)$) and klystron ($\varphi_{\mathrm{Klys,out}}(s)$) signals however are each down-converted and thus have an additional noise source. The additive noise of the up- ($\varphi_{\varphi,\mathrm{UPC}}(s)$) and down-conversion ($\varphi_{\mathrm{DWC,1}}(s)$ and $\varphi_{\mathrm{DWC,2}}(s)$) channels have already been characterized in Subsection 3.2.3.2. The additive noise of the pre-amplifier ($\varphi_{\mathrm{PA}}(s)$) and klystron ($\varphi_{\mathrm{Klys}}(s)$) are the values of interest.

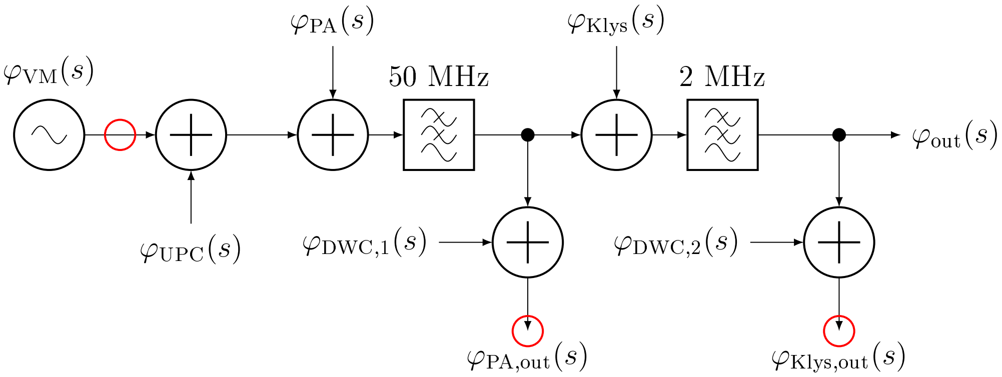

Figure 4.9: Model of the actuator chain noise sources.

The additive jitter is commonly calculated using the sum of zero-mean randomly distributed signals. For two zero-mean signals X and Y, the variance[2] of the sum (S) equals the sum of the variances plus twice a correlated

---

[2] Square of the standard deviation / RMS

term, the covariance $\mathrm{Cov}[X, Y]$

$$\begin{aligned}\sigma_\mathrm{S}^2 &= E[S^2] = E[(X+Y)^2] = E[X^2] + E[Y^2] + 2\mathrm{Cov}[X, Y] \\ &= \sigma_\mathrm{X}^2 + \sigma_\mathrm{Y}^2 + 2\sigma_\mathrm{XY}.\end{aligned}$$

For uncorrelated signals, the covariance σ_XY equals zero and from this, the RMS value of one of the signals could be calculated if the sum signal and one of the input signals is known

$$\sigma_\mathrm{Y} = \sqrt{\sigma_\mathrm{S}^2 - \sigma_\mathrm{X}^2}. \tag{4.3}$$

However, the signals measured with the LLRF system are not truly uncorrelated as they all originate from the same source and as such the additive noise cannot be directly calculated since the correlated term is unknown

$$\sigma_\mathrm{Y} = \sqrt{\sigma_\mathrm{S}^2 - \sigma_\mathrm{X}^2 - 2\sigma_\mathrm{XY}}. \tag{4.4}$$

As the correlated term cannot be measured or calculated, the above explanation cannot be used in this case. As a quantity for the amount of correlation, the Pearson correlation coefficient (PCC) [66] can be used. The PCC is a statistic that indicates the (linear) relation between two variables and can be calculated as the covariance of the variables divided by the product of their standard deviations

$$r_{XY} = \frac{\sigma_\mathrm{XY}}{\sigma_\mathrm{X}\sigma_\mathrm{Y}}. \tag{4.5}$$

The result is a value in the interval $[-1, 1]$, a positive value indicates a linear correlation. In the case of two measured signals this means both signals show the same behavior regarding increase and decrease of values with identical behavior when r_{XY} equals 1. Negative values are interpreted as opposite behavior, meaning if one signal rises, the other is falling. A value of 0 means both signals are completely uncorrelated. Although the PCC needs to be interpreted correctly and has different meaning for different scenarios as stated in [66], it is used in the following to interpret the measured values from Table 4.4. Table 4.6 shows the calculated correlation coefficients between the vector modulator, pre-amplifier and klystron signal. These were calculated using MATLAB's `corrcoef` function.

The PCC of the vector modulator and either the pre-amplifier or klystron signal is about 0.2. This value indicates only a small correlation between either signals. Also the PCC of the pre-amplifier and klystron is fairly low

r_{XY}	VM	PA	Klys
VM	1	0.19	0.18
PA	0.19	1	0.40
Klys	0.18	0.40	1

Table 4.6: Correlation coefficients calculated with MATLAB's `corrcoef` function using 4.5.

with 0.4. Interpreting these values as mean of dominating noise source, a PCC of 0.2 would mean the larger part of the noise measured in $S_{\varphi,\mathrm{PA,out}}$ is contributed by $S_{\varphi,\mathrm{PA}}$ rather than the input of $S_{\varphi,\mathrm{VM}}$ and $S_{\varphi,\mathrm{UPC}}$. In a similar way, the noise contribution to $S_{\varphi,\mathrm{Klys,out}}$ can be interpreted such that the noise added by the klystron $S_{\varphi,\mathrm{Klys}}$ is the dominating source of noise compared to the input of the klystron. However, it is not possible to derive absolute values for these quantities with this method. Also the noise added by pre-amplifier and klystron can be interpreted as uncorrelated as the main contributors to the noise are the power grid in case of the pre-amplifier and the high-voltage signal of the modulator for the klystron.

Taking the 7.7 fs of absolute jitter at the klystron output and comparing it to the specified overall acceptable phase noise of 58 fs, the absolute noise is roughly 13% of the specification. This measurement however does not show the jitter from the beam point of view, which is done in the next section.

4.2.2 Beam-based measurements

Taking the same measurement as before, but analyzing the screen data, the RF jitter can be calculated. The screen data is obtained through image analysis where the image of the streaked beam is taken and brought to a comparable state by processing the image data. Usually a pixel of an image does not relate to the same length in both axes. Also, with a different calibration of the screen, a pixel can relate to a different length. For compensation, the images are stretched and rotated, such that a pixel relates to the same length in all images. Knowing the equivalent size of a pixel, the centroid of the beam on the image can be calculated. For successive shots, the kick induced by phase jitter leads to a small offset of the centroid compared to the previous image. The offset captured in each shot represents one data point. For analysis, the whole data set is then processed by the same filter as before to get rid of the long-term effects. This is shown in Fig. 4.10. Shown in blue is the original and in red the filtered data. Instead of the absolute phase on the ordinate, the phase offset to the centroid of the bunch on the screen is shown. This measurement shows only 2000 shots, because the machine was operated with about 1 Hz repetition rate for the beam pulses while the LLRF system always captures data with 10 Hz and produces RF pulses at the same rate.

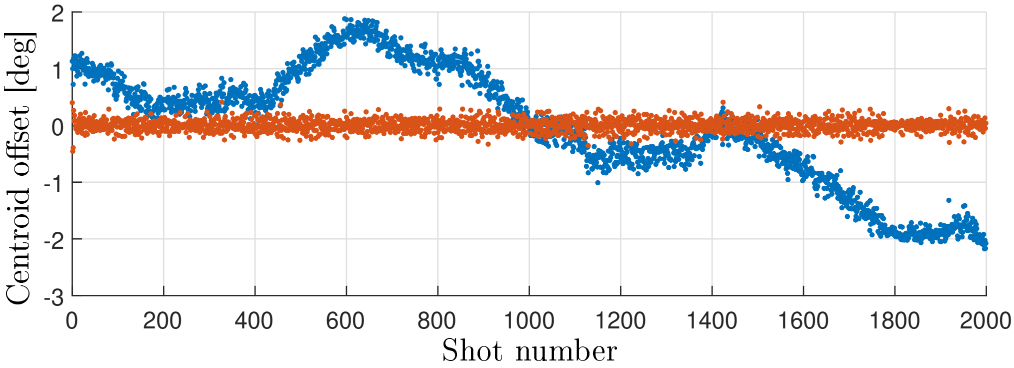

Figure 4.10: Jitter of the image on the screen, blue: original, red: filtered.

Calculating the jitter from this yields 0.089° or 20.6 fs phase noise when related to the 12 GHz of the PolariX TDS. This value is a lot better than the specification requires (35%) and may be an explanation for the stable image. The additional noise compared to the value of the RF only is caused by other external factors like the beam jitter itself, the kicker magnets and noise of the screens hardware. As these components are not part of this thesis, they are not further considered. What can be said from the performed measurements, is that the LLRF system and especially the newly developed conversion boxes do not significantly contribute to the noise within the whole system. Additionally, recent experiments with the machine showed an arrival time jitter of the beam of about 20 fs. A first conclusion can be made that the majority of the jitter seen by the beam, is caused by the beam itself.

4.2.3 Cavity measurements

Since there is no experience yet with the RF inside a system like the PolariX, the impact of the phase shifter on the RF is not clear. In an HFSS model of the cavity, a phase sweep is simulated by inserting a split wave into both inputs with a theoretical model of a phase shifter in one of the inputs. Ideally, the phase difference at the outputs is the same as at the inputs. The result shown in Fig. 4.11a however shows a small deviation of the output phase difference compared to the input. This deviation reaches from -2.68° to 2.63°.

To verify this behavior, a sweep of the phase shifter from 0° to 180° phase difference is made and the signals at the cavity input and both loads are

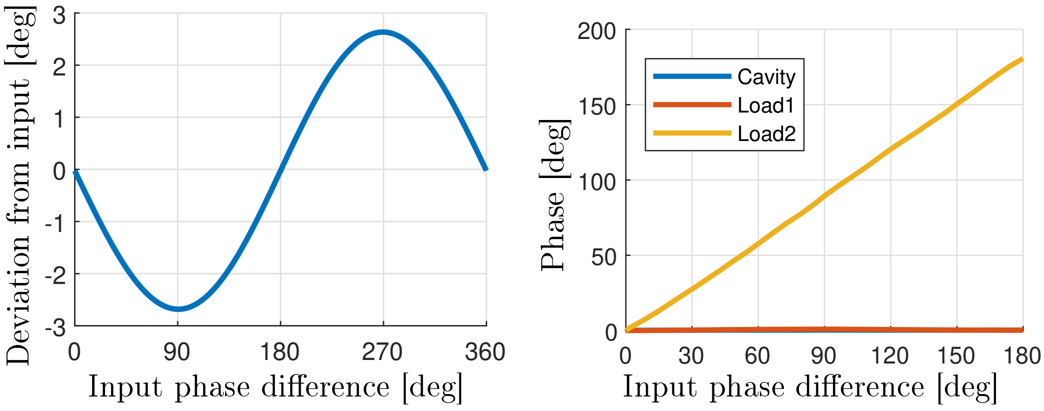

(a) HFSS simulation of the impact of the phase shifter on the phase difference.

(b) Phase shifter sweep measured at the cavity input and loads.

Figure 4.11: Phase shifter impact on the phase as HFSS simulation and measured in the system.

analyzed. As the cavity signal is measured before the RF is split into the two input parts (see Fig. 4.2) and the phase shifted RF is completely dumped into the second load, influences of the cavity on the RF can be measured in both signals and influences of the phase shifter can be measured only at the second load. The result of this sweep is shown in Fig. 4.11b. At this scale, only the impact of the phase shifter in the load2 signal (yellow) can be seen, the cavity input and load1 signals seem to be the same. In case of the cavity and load1 signals, this is (almost) 0°. In case of the load2 signal this is a linear increase from 0° to 180° corresponding to the phase shifter sweep. For better analysis, the difference to the ideal value is plotted in Fig. 4.12.

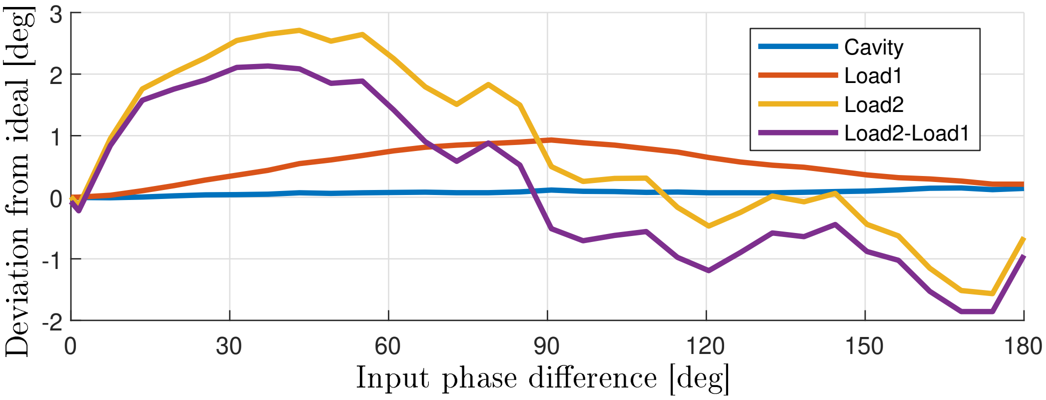

Figure 4.12: Analysis of the phase shifter sweep.

The cavity signal (blue) is almost constant with no significant changes with the phase shifter. As the signal is picked up before the phase shifter, this is expected but also shows there is no reflective influence. At the first load (red), an effect similar to the simulated sweep can be seen, but with a smaller deviation than simulated. However, the RF going through the phase shifter is not measured at the first load. As such, this effect seems to be caused by the cavity itself and not the phase shifter. The RF measured at the second load (yellow) contains any influence of the phase shifter to the RF but also of the cavity. The influence of the cavity is known in the first load, hence it can be subtracted from the second load to get only the effects of the phase shifter (purple).

The measurements show that the effect of the phase shifter simulated in Fig. 4.11a is caused by the cavity. The phase shifter itself alters the phase not only in a purely linear way, but also with a small deviation depending on the phase shifter position. Ranging from 2.1° to -1.8° this deviation is a bit larger than that of the cavity, which is going up to 0.93°. In a future update, this deviation can be integrated into the systems controls to counteract the effects of the offset.

4.2.4 Streaking kick

During the operation of the TDS, a problem occurred when streaking the beam. Instead of only observing the streak, a small kick of the beam could be observed on the screen as shown in Fig. 4.13.

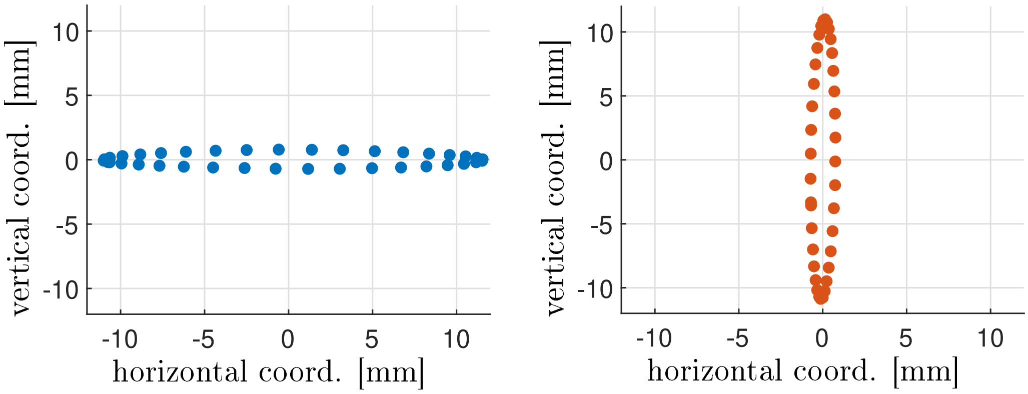

(a) Horizontal streak.

(b) Vertical streak.

Figure 4.13: Observed kick to the beam centroid measured by a beam position monitor (BPM) when streaking the beam in horizontal and vertical direction.

Independently of the polarization of the streaking, the beam seems to move in an elliptic pattern around the expected streak (x-axis in Fig. 4.13a and y-axis in Fig. 4.13b) when moving the phase shifter. This kick is caused by a power difference between the two inputs which is due to the different paths after the hybrid coupler (see Fig. 2.10). While the first path is a direct connection to the TE11 mode launcher, the second path includes the phase shifter, which causes different losses in the RF. As such, the polarization principle introduced in Subsection 2.2.4 with 2.12 is only partly true and needs to be expanded. V_1 and V_2 have different power in x and y direction with V_x and V_y, respectively,

$$\begin{aligned} V_1 &= V_{x_1}\sin(\omega t) + V_{y_1}\cos(\omega t) \\ V_2 &= V_{x_2}\sin(\omega t + \Delta\varphi) - V_{y_2}\cos(\omega t + \Delta\varphi). \end{aligned}$$

With this the total signal $V_1 + V_2$ becomes

$$\begin{aligned} V_{\text{total}} = &\quad V_1 + V_2 \\ = &\quad V_{x_1}\sin(\omega t) + V_{y_1}\cos(\omega t) + V_{x_2}\sin(\omega t + \Delta\varphi) - V_{y_2}\cos(\omega t + \Delta\varphi) \\ = &\quad V_{x_1}\sin(\omega t) + V_{y_1}\cos(\omega t) \\ &+ V_{x_2}(\sin(\omega t)\cos(\Delta\varphi) + \cos(\omega t)\sin(\Delta\varphi)) \\ &- V_{y_2}(\cos(\omega t)\cos(\Delta\varphi) - \sin(\omega t)\sin(\Delta\varphi)) \\ = &\quad \sin(\omega t)(V_{x_1} + V_{x_2}\cos(\Delta\varphi) + V_{y_2}\sin(\Delta\varphi)) \\ &+ \cos(\omega t)(V_{y_1} + V_{x_2}\sin(\Delta\varphi) - V_{y_2}\cos(\Delta\varphi)). \end{aligned}$$

As can be seen here, contrary to 2.12 where only a $\sin(\omega t)$ term was present, a $\cos(\omega t)$ term also contributes to the total signal. This superposition is a slightly rotating wave with an elliptic projection which has a decreasing eccentricity with an increase in power difference of the two inputs. Fig. 4.14 shows a MATLAB simulation of the modeled RF.

The two input waves (blue and red) are as described in Subsection 2.2.4 the two left- and rightwise rotating fields. With equal input power in both inputs (Fig. 4.14a and Fig. 4.14b), the superposition (yellow) is a plane wave that is rotated by half the phase difference between the two inputs. The projection in the longitudinal direction (traveling direction of the waves) of this superposition (purple) is a straight line and is the desired behavior of the PolariX TDS streak. However, due to a power imbalance, the superposition is a rotating field with an elliptic projection (Fig. 4.14c and Fig. 4.14d) which renders the observed behavior on the BPM.

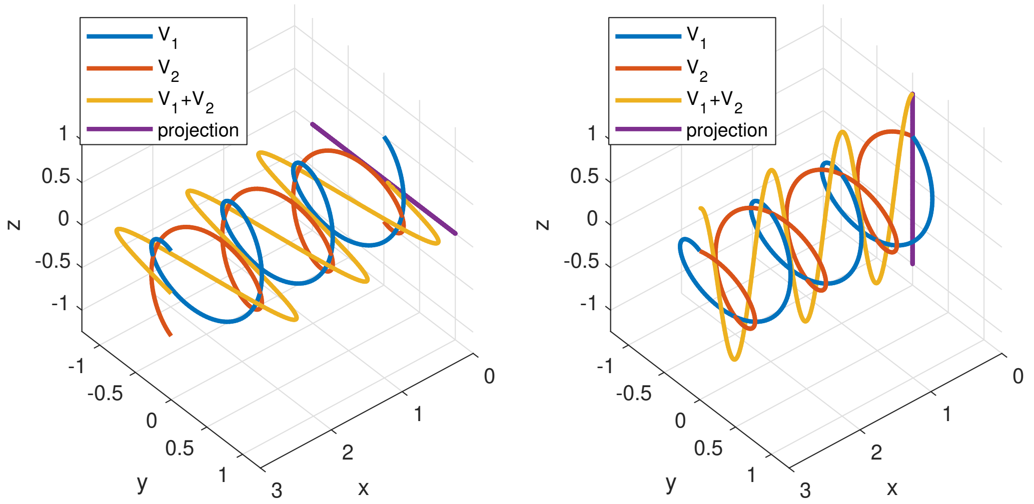

(a) Polarization with $\Delta\varphi = 0°$ and $V_{x_2} = V_{x_1}$.

(b) Polarization with $\Delta\varphi = 180°$ and $V_{x_2} = V_{x_1}$.

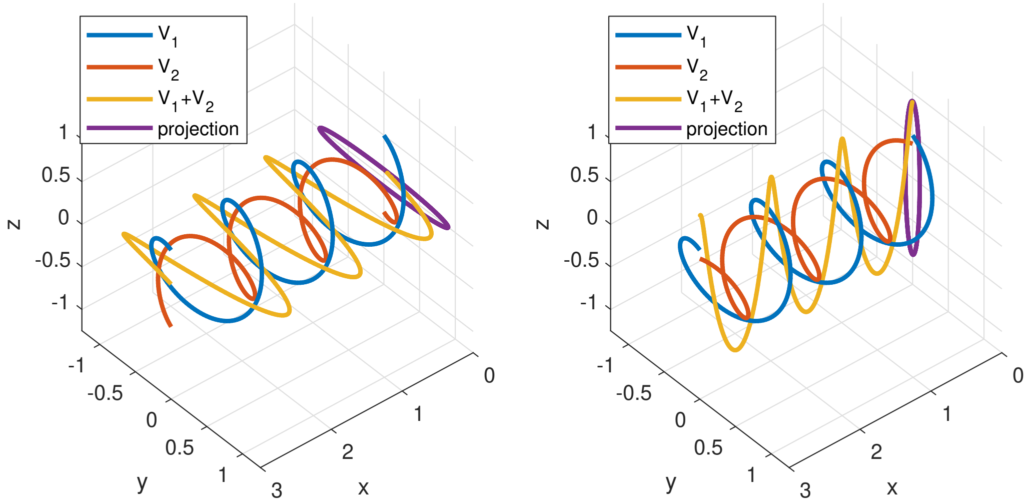

(c) Polarization with $\Delta\varphi = 0°$ and $V_{x_2} = 0.8 \cdot V_{x_1}$.

(d) Polarization with $\Delta\varphi = 180°$ and $V_{x_2} = 0.8 \cdot V_{x_1}$.

Figure 4.14: MATLAB model of the RF inside the PolariX TDS showing the polarization and offset when a power imbalance occurs.

Means to correct this are already in discussion. A first idea is to not split the power into the two input branches equally, but use a variable splitter and calibrate it such that the losses in the phase shifter are compensated and an equal amount of power is coupled into the PolariX.

4.2.5 Long-term behavior

An uncertainty has been observed during the operation of the TDS regarding the long-term behavior, where the image on the screen drifts a lot more over time than the RF does. This is shown in Fig. 4.15. The screen signal (blue) drifts away over time without changing any parameters of the machine a lot more compared to the RF signal (red). On the screen, the long-term drift of this measurement has a peak-to-peak value of 4.06°, while the RF drifts by only 0.43°. Additionally, the two signals do not show a similar behavior in up- and down slopes, which would be expected if the drift originated from the same source. The first assumption is that this is caused by the FGB, because all signals in the UniLOGM, MicroTCA.4 LLRF system, and conversion boxes are based on that. This assumption can be analyzed once the setup in SINBAD is running as that setup is not based on the FGB. A recent discovery showed that the reference signal cable was not properly placed and partly exposed to environmental effects which most likely contributes a huge portion to the measured drift.

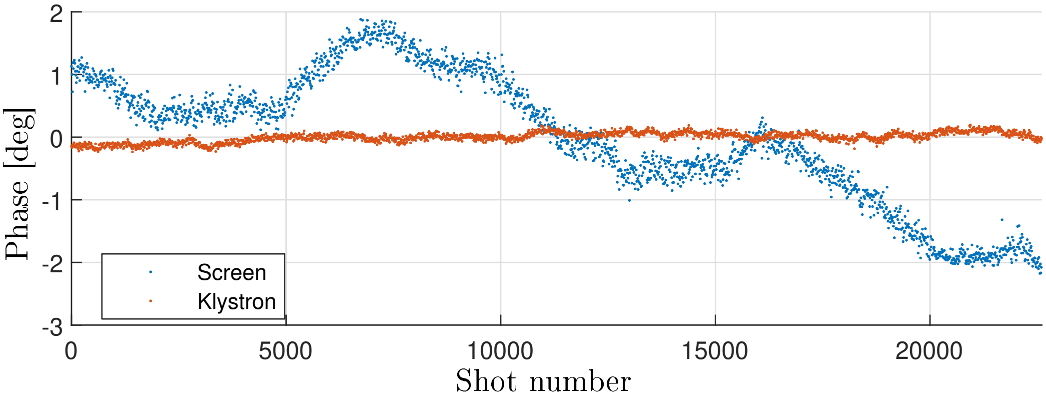

Figure 4.15: Long-term drift of the image on the screen compared to the RF.

4.2.6 Amplitude noise

The phase noise is more important for the PolariX TDS than the amplitude noise, as the latter tends towards zero in the zero crossings of the phase where the TDS is operated. A first measurement has been done by analyzing the correlation between the relative bunch length error and the streak amplitude of the bunch. This is done by taking various streak amplitudes and observing multiple bunches for each of them. The coefficient of variation as explained in Subsection 4.2.1 (eq. 4.2) of the observed bunch lengths at the screen is defined as the amplitude jitter. The result of the measurement is shown in Fig. 4.16a.

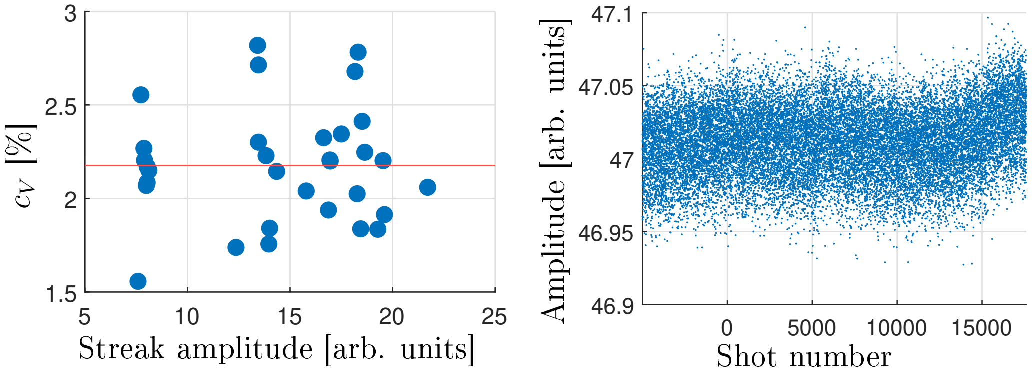

(a) c_V for multiple bunches taken with various streak amplitudes.

(b) RF amplitude measurement of the klystron output.

Figure 4.16: Amplitude noise measured with screens from the beam point of view and the RF.

The mean of these c_V values is 2.18% (red line). This result is more than twice as large as the specification of 1%. However, looking only at the RF, the result is a lot different. For this analysis, the same long-term measurement as for the phase analysis is taken, but the amplitude is measured at the klystron output. This is shown in Fig. 4.16b. From this, the amplitude noise of the RF signal can be determined as 0.051%. Where the difference in these measurements originates is currently unclear and still subject of research. There are several sources not measurable by the LLRF system which need to be analyzed in the future. These are calibration uncertainties of the screens, jitter of the beam itself and jitter of the reference signal.

4.3 Summary

This chapter describes the installation of the PolariX TDS and its LLRF system at the FLASHForward facility. First measurements with the live machine are reported and fitting means to analyze the results are discussed. The actuator chain is characterized, resulting in a measured phase timing jitter of 7.7 fs (33.2 m°) of the RF entering the TDS. However, due to the pulsed characteristic of the actuators and missing measurement equipment for pulsed systems, only an estimate of the real residual noise values can be made. When taking the data of the screens used to observe the pulse, a total phase jitter of 20.6 fs (0.089°) is measured which is only about 35% of the specified 57.9 fs of maximum allowed phase jitter. A small deviation of the RF phase is observed when using the phase shifter. In a future update, this information can be used to compensate the effects of the deviation. During these measurements a small kick of the beam has been observed instead of only a streak. The cause of this is a small power imbalance in both cavity inputs caused by the phase shifter. This kick is modeled mathematically with a good fit of the observed behavior. Uncertainties still exist regarding the long-term behavior and the amplitude noise. In both cases, the data taken by the screens show a larger value than what is measured by the LLRF system. The origin of these effects is currently not known and subject of ongoing research.

Chapter 5

Conclusion & Outlook

This chapter summarizes this thesis and draws conclusions from everything observed in the previous chapters in the first Section 5.1. The second Section 5.2 gives an outlook on already planned future work with the PolariX TDS in other facilities and also lists work that needs to be done for the running system in FLASHForward.

5.1 Conclusion

In this thesis, a complete LLRF system for the new PolariX TDS prototype has been developed, installed and commissioned in the FLASHForward beamline. In order to re-use the already existing MicroTCA.4 S-band LLRF system, three different 19" modules have been created, the XLOGM, XDWCM and XDWCM_UPC. The XLOGM takes a 3 GHz reference signal and multiplies it to 9 GHz. This signal is then used in the XDWCM and XDWCM_UPC as LO for the included RF mixers to convert between 12 and 3 GHz, so the existing S-band LLRF system can process the PolariX TDS signals.

For all of these modules, the necessary RF components have been selected and characterized. PCBs have been designed, simulated, produced and packaged into hermetically sealed housings to reduce the impact of environmental changes, before being put together into 19" cases. Measurements of these have been done in the laboratory to verify the suitability for the overall system to meet the specifications of at most 0.25° or 57.87 fs short-term phase noise at 12 GHz seen by the beam. The measurements have shown an additive phase noise of 0.0062° (1.4 fs) for the 9 GHz LO generation, 0.0016° (0.371 fs) for the down-conversion and 0.0012° (0.278 fs) for the up-conversion channel, making clear the conversion only adds a very small portion to the overall acceptable noise.

The system was then installed in the FLASHForward beamline and successfully commissioned. A short-term RF analysis has been made, measuring the actuator chain from the LLRF systems drive signal output up to the output of the klystron within the accelerator tunnel. For this, the long-term effects needed to be removed and viable means to do so have been discussed and compared. The result is a high-pass filter that has been applied to the taken data, which lead to 0.0273° (6.3 fs) additive noise.

The same analysis has been made from the beam point of view by calculating the jitter of the images on the screen, which quantifies the RF noise actually seen by the beam. Here, the result was 0.089° (20.617 fs) of short-term phase noise which is only about a third compared to the 0.25° (57 fs) phase noise specified as upper boundary. The overall stability on the screen, contrary to the experience with other TDS systems, does not require an additional control algorithm for short-term stability.

As another step to verify the RF behavior, the phase shifter installed to rotate the polarization of the streak has been analyzed. When changing the polarization angle, only one of the two cavity outputs should have changed in phase. This behavior could also be seen in the live machine.

In the future, the FLASH2 and Accelerator Research Experiment at SINBAD (*ARES*) beamline at SINBAD will also receive two PolariX TDS. These setups also includes a barrel-open cavity as a mean of pulse compression to further increase the streaking power.

5.2 Outlook

As already mentioned before, the PolariX in FLASHForward is the first to have ever been used in a live accelerator and was used as proof of concept and prototyping of a PolariX installation. FLASH2 and SINBAD are two other beamlines at DESY that are interested in the PolariX cavity and at the time of writing this thesis, the cavities are already in production. Both beamlines are supposed to get two PolariX cavities to further increase the possible streaking.

5.2.1 FLASH2

The setup in FLASH2 has already been shown in Fig. 4.1. In addition to the PolariX in FLASHForward, the pre-amplifier and klystron that are already installed, two additional PolariX will be installed in the FLASH2 beamline, both operated by the same klystron and LLRF system as FLASHForward. For this, a mechanical RF switch is installed to allow switching between the beamlines without the need to change the system by hand. As the deflecting voltage (V) is what matters in regards to the streaking strength, it needs to be increased to achieve better streaking. V is directly proportional to the length of the cavity (L) and the square root of the incoming power (P): $V \propto L\sqrt{P}$. By using the same klystron and a 3 dB splitter, but two cavities, the power is halved but the length doubled, thus the streaking voltage is increased by $\sqrt{2} = 1.414$.

For measurements, it is foreseen to install another two XDWCM and DWC8VM1 in the LLRF system with a copy of the cavity section of the signals for each of the cavities. As such, the whole FLASH facility PolariX LLRF system consists of one MicroTCA.4 crate including four DWC8VM1, four SIS8300L2 and one x2timer and additionally one XLOGM, one XDWCM_UPC and three XDWCM. Also planned is a barrel-open cavity, which is explained in the following section. An additional coupler is added to the waveguide system after the BOC to measure the signal. With everything installed in the FLASH facility, the LLRF system looks as shown in Fig. 5.1.

5.2.1.1 Barrel-open cavity

The barrel-open cavity (BOC) is a single open cavity in barrel form, used for pulse compression. Pulse compression in general is used to increase the peak power of a pulse, at the cost of duration. This is usually done by preserving power delivered by the klystron and re-introducing it such that a new, much higher pulse is formed. The currently most commonly used principles to

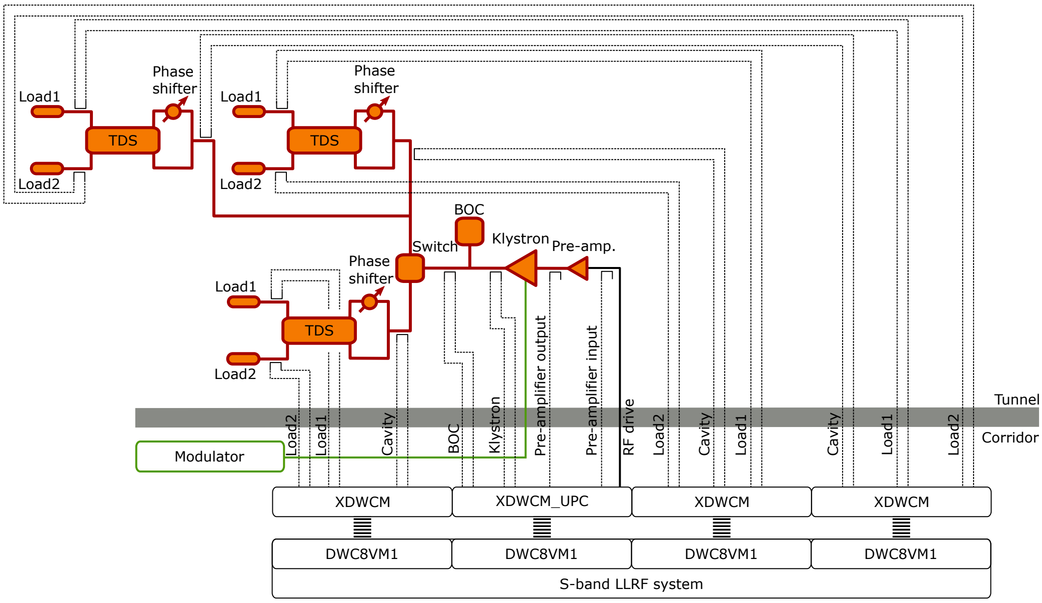

Figure 5.1: The LLRF system of the final setup at the FLASH facility.

increase the peak power of the RF pulse are those of the SLAC energy doubler (*SLED* [67]), where two cavities and a 3 dB coupler are used. However, this provides some problems for higher frequencies [68] where achieving the desired high quality factor can lead to distortion of the RF signal due to multiple RF modes interacting with each other. The other approach is to use a BOC, which only requires a single cavity and waveguide. In case of the PolariX, the latter is the better approach due to the mentioned possible problems and also from an economical point of view. The design of the X-band BOC (*XBOC*) adapted the design of the C-band BOC [22] currently in use in the SwissFEL linac [69]. It is shown in Fig. 5.2 as section view and live picture of the prototype. The principle is a circular waveguide around the cavity, with a traveling RF wave going through it. The waveguide and cavity are connected via multiple coupling slots, which are spaced $\lambda/4$ (quarter wavelength of the RF) of each other. This causes a so called *whispering gallery* mode. Each coupling slot radiates a forward and a backward traveling wave in the waveguide. While the forward traveling ones are all in phase and thus add up, the backward traveling waves experience cancellation. As such, the output of the BOC is the superposition of all the waves emitted from the cavity and the incoming traveling wave in the waveguide. If the phase of the incoming wave is reversed by 180° during one compressed pulse time, the stored energy can be released much faster and thus increases the peak power of the RF pulse at the cost of pulse duration [70]. However, the shape of the output pulse does not have a flat top anymore, usually in amplitude and phase. As this is required for a homogeneous interaction with the beam, this needs to be corrected.

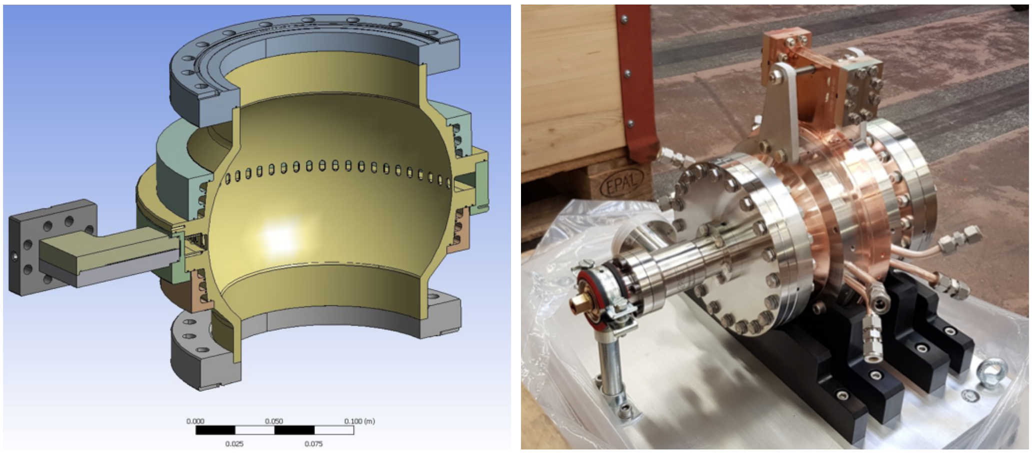

(a) Section view.

(b) XBOC prototype.

Figure 5.2: Section view and live picture of the XBOC prototype, source: [22].

One method to correct the shape has been introduced in [71] and [72] using a model-free iterative learning control scheme. This scheme is based on an optimization problem, varying a linear time-invariant finite impulse response filter with each iteration until a set maximum error is reached. Within about 20 iterations, the shape could be formed to have a stable flat top in amplitude and phase. This has been applied in the SwissFEL facility. As such, the scheme can also be applied to the FLASH and SINBAD facilities.

5.2.2 SINBAD

The Short Innovative Bunches and Accelerators at DESY (*SINBAD*) facility, or more precisely, the ARES beamline is also getting two PolariX TDS in the near future, equivalent to FLASH2. The planned general setup is shown in Fig. 5.3. Like at FLASH2, the two cavities will be placed behind each other to reach a higher streaking voltage. Contrary to FLASH2, though, both cavities will have their own LLRF system, modulator, klystron and BOC to reach even higher streaks, as no 3 dB splitter is needed to feed both cavities with RF [73]. As such, each LLRF system will be similar to that of the prototype setup in FLASHForward with the addition of a BOC, consisting of one XDWCM, one XDWCM_UPC and two DWC8VM1+SIS8300L2 in the MicroTCA.4 system as shown in Fig. 5.4. Also, no FGB is needed since the reference frequency of the facility is already 3 GHz.

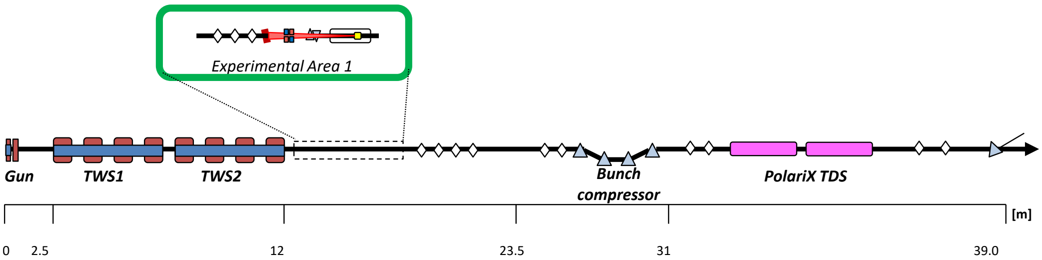

Figure 5.3: The SINBAD-ARES beamline with the 2x PolariX TDS towards the end.

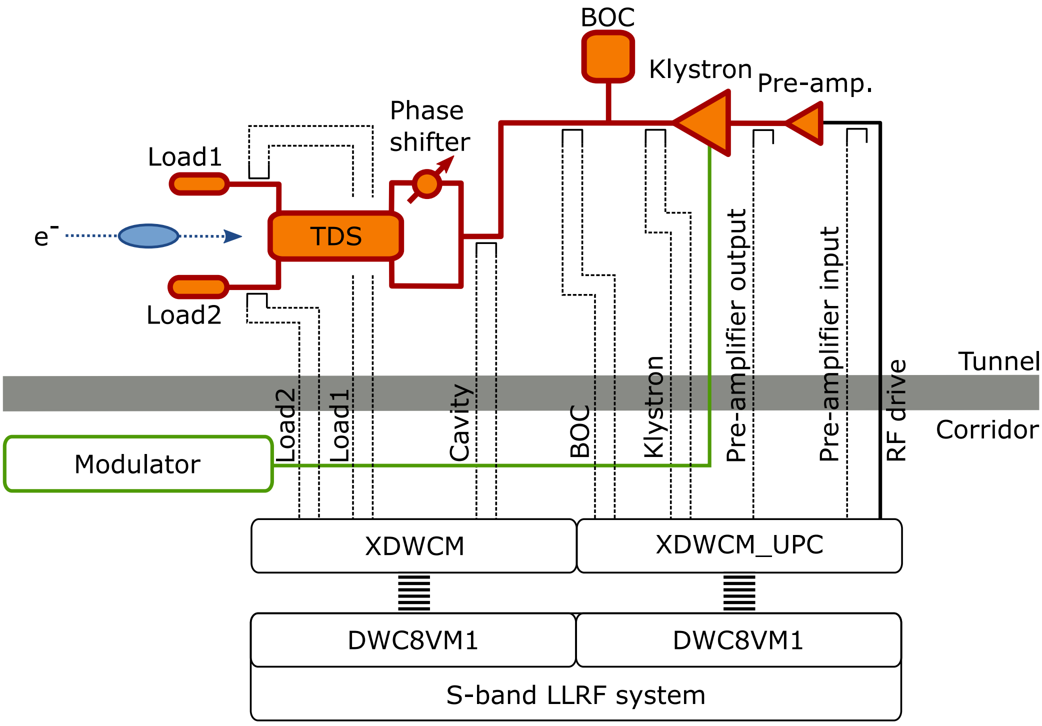

Figure 5.4: The LLRF system for each PolariX cavity at SINBAD.

5.2.3 Controls

As for now, no short-term control algorithm is needed in the LLRF system. To help with long-term drifts, an output vector correction algorithm (OVC) is implemented. It compares the phase of the klystron output to a set value and corrects the drive signal towards the set value if the measured signal drifts too far away from the set value. This though only allows to react from pulse to pulse or over the average of multiple pulses.

There are multiple observations ongoing on how to further stabilize the RF for more precise or easier measurements. In the current setup, moving the phase shifter has led to a small change in the zero-crossing phase which meant the measurements on the screens needed to be re-calibrated each time it was moved. A slow RF feedback is foreseen, which would correct this by analyzing the data shown on the screen and adapting the output accordingly.

For further phase stability, the TMCB as explained in Subsection 3.2.2.2 is already built into the XLOGM. With four temperature read-out channels and an FPGA mezzanine card (*FMC*) connector, where various boards can be connected to, it offers a good base for a temperature control system. This could be implemented in the XLOGM and conversion boxes with Peltier coolers to reduce the effects of temperature changes on the RF phase.

List of Figures

List of Tables

Bibliography

[1] P. Horowitz and W. Hill, *The Art Of Electronics*. Cambridge, New York: Cambridge University Press, 1989.

[2] A. Gallo, "Basics of RF electronics," in *Proceedings, CAS - CERN Accelerator School: RF for Accelerators, Ebeltoft, Denmark, 8 - 17 Jun 2010*, 2011.

[3] F. Ellinger, "RF Basics," *Radio Frequency Integrated Circuits and Technologies*, pp. 79–108, 2007.

[4] F. Marki and C. Marki, "Mixer Basics Primer: A Tutorial for RF & Microwave Mixers, Marki Microwave." `https://www.markimicrowave.com/assets/appnotes/mixer_basics_primer.pdf`, 2010.

[5] J. Karki, "Calculating noise figure and third-order intercept in ADCs," vol. Analog Applications Journal, 2003.

[6] K.-C. Chan, "IP3 and Intermodulation Guide." `https://pdfserv.maximintegrated.com/en/an/IP3_and_Intermodulation_Guide.pdf`, Aug. 2020.

[7] M. Hoffmann, *Development of a multichannel RF field detector for the low-level RF control of the free-electron laser at Hamburg*. PhD thesis, Deutsches Elektronen-Synchrotron DESY, Hamburg, Hamburg University of Technology TUHH, 2008.

[8] S. C. Cripps, *RF power amplifiers for wireless communications*. Artech House microwave library, Boston: Artech House, 2nd ed., 2006.

[9] J. J. Grobbelaar, *Phase noise measurement*. PhD thesis, University of Stellenbosch, 2011.

[10] E. Rubiola, "The Leeson effect - Phase noise in quasilinear oscillators," *arXiv preprint physics/0502143*, pp. 1–15, 2005.

[11] F. Gerigk, "Cavity Types," p. 23 p, Nov 2011. presented at the CERN Accelerator School CAS 2010: RF for accelerators, Ebeltoft, 8-17 June 2010; CERN-2011-007, pp. 277-298.

[12] R. H. Miller, "Comparison of Standing Wave and Traveling Wave Structures," in *13th International Linear Accelerator Conference*, pp. TU2–4, 1986.

[13] H. Podlech, "Superconducting versus normal conducting cavities," in *CERN Accelerator School on High Power Hadron Machines*, Mar. 2013.

[14] B. Aune, R. Bandelmann, D. Bloess, B. Bonin, A. Bosotti, M. Champion, C. Crawford, G. Deppe, B. Dwersteg, D. A. Edwards, *et al.*, "Superconducting TESLA cavities," *Physical Review Special Topics - Accelerators and Beams*, vol. 3, Sept. 2000.

[15] R. Brinkmann, E. Schneidmiller, J. Sekutowicz, and M. Yurkov, "Prospects for CW and LP operation of the European XFEL in hard X-ray regime," *Nuclear Instruments and Methods in Physics Research Section A: Accelerators, Spectrometers, Detectors and Associated Equipment*, vol. 768, p. 20–25, Dec. 2014.

[16] N. Pichoff, "Introduction to RF linear accelerators," in *CERN Accelerator School and DESY Zeuthen: Accelerator Physics*, pp. 105–128, Sept. 2003.

[17] G. Burt, "Transverse deflecting cavities," in *CERN Accelerator School: Course on RF for Accelerators*, Jan. 2012.

[18] K. Floettmann and V. V. Paramonov, "Beam dynamics in transverse deflecting RF structures," *Phys. Rev. ST Accel. Beams*, vol. 17, p. 024001, Feb. 2014.

[19] R. D'Arcy, V. Libov, and J. Osterhoff, "A Transverse Deflecting Structure for the Plasma Wakefield Accelerator Experiment, FLASHForward," vol. IBIC2016, 2017.

[20] K. Wittenburg, B. Marchetti, R. Assmann, B. Beutner, J. Branlard, F. Christie, R. D'Arcy, W. Decking, U. Dorda, J. Herrmann, M. Hoffmann, M. Hüning, O. Krebs, G. Kube, S. Lederer, F. Ludwig, F. Marutzky, D. Marx, J. Osterhoff, and W. Wuensch, "X-Band TDS Project," May 2017.

[21] P. Craievich *et al.*, "Status of the Polarix-TDS Project," in *Proc. 9th International Particle Accelerator Conference (IPAC'18), Vancouver, BC, Canada, April 29-May 4, 2018*, no. 9 in International Particle Accelerator Conference, (Geneva, Switzerland), pp. 3808–3811, JACoW Publishing, June 2018. https://doi.org/10.18429/JACoW-IPAC2018-THPAL068.

[22] P. Craievich, M. Bopp, H.-H. Braun, A. Citterio, R. Fortunati, R. Ganter, T. Kleeb, F. Marcellini, M. Pedrozzi, E. Prat, S. Reiche, K. Rolli, R. Sieber, A. Grudiev, W. L. Millar, N. Catalan-Lasheras, G. McMonagle, S. Pitman, V. d. P. Romano, K. T. Szypula, W. Wuensch, B. Marchetti, R. Assmann, F. Christie, B. Conrad, R. D'Arcy, M. Foese, P. G. Caminal, M. Hoffmann, M. Huening, R. Jonas, O. Krebs, S. Lederer, D. Marx, J. Osterhoff, M. Reukauff, H. Schlarb, S. Schreiber, G. Tews, M. Vogt, A. d. Z. Wagner, and S. Wesch, "Novel X-band transverse deflection structure with variable polarization," *Phys. Rev. Accel. Beams*, vol. 23, p. 112001, Nov. 2020.

[23] A. Grudiev, "Design of compact high power RF components at X-band," May 2016.

[24] D. Marx, R. Assmann, P. Craievich, U. Dorda, A. Grudiev, and B. Marchetti, "Reconstruction of the 3D charge distribution of an electron bunch using a novel variable-polarization transverse deflecting structure (TDS)," *Journal of Physics: Conference Series*, vol. 874, p. 012077, July 2017.

[25] G. D'Auria, "X-band technology applications at fermi@elettra fel project," *Nuclear Instruments and Methods in Physics Research Section A: Accelerators, Spectrometers, Detectors and Associated Equipment*, vol. 657, no. 1, pp. 150 – 155, 2011. X-Band Structures, Beam Dynamics and Sources Workshop (XB-10).

[26] "MicroTCA is a trademark of PICMG, MTCA.4 specifications source." http://www.picmg.org, Jan. 2020.

[27] B. Lorbeer, "Stability of the Master Oscillator for FLASH at DESY.," *TESLA Report*, 2006.

[28] M. Zukocinski, K. Czuba, M. Urbański, M. Hoffmann, F. Ludwig, and H. Schlarb, "Universal High-Performance LO and CLK Generation Module for LLRF System Receivers," June 2016.

[29] I. Rutkowski, L. Butkowski, M. Hoffmann, H. Schlarb, and C. Schmidt, "REGAE LLRF Control System Overview," in *Proceedings, 4th International Particle Accelerator Conference (IPAC 2013): Shanghai, China, May 12-17, 2013*, p. THPEA031, 2013.

[30] J. Branlard, G. Ayvazyan, V. Ayvazyan, M. Grecki, M. Hoffmann, T. Jeżyński, F. Ludwig, U. Mavrič, S. Pfeiffer, H. Schlarb, C. Schmidt, H. Weddig, B. Yang, P. Barmuta, S. B. Habib, L. Butkowski, K. Czuba, M. Grzegrzółka, E. Janas, J. Piekarski, I. Rutkowski, D. Sikora, L. Zembala, M. Żukociński, W. Cichalewski, W. Jałmużna, D. Makowski, A. Mielczarek, A. Napieralski, P. Perek, A. Piotrowski, T. Poźniak, K. Przygoda, G. Bołtruczyk, S. Korolczuk, M. Kudła, J. Szewiński, K. Oliwa, and W. Wierba, "MTCA.4 LLRF system for the European XFEL," in *Proceedings of the 20th International Conference Mixed Design of Integrated Circuits and Systems - MIXDES 2013*, pp. 109–112, June 2013.

[31] MicroTCA Technology Lab, "RTM 8 Channel Down-converter 1 Channel Up-Converter, DRTM-DWC8VM1." `https://techlab.desy.de/products/rtm/drtm_dwc8vm1/index_eng.html`, Jan. 2020.

[32] Struck Innovative Systems, "10 Cahnnel 125 MS/s 16-bit With Fast Feedback DACs, SIS8300-L2 MicroTCA.4 Digitizer." `https://www.struck.de/sis8300-l2.html`, Jan. 2020.

[33] MicroTCA Technology Lab, "AMC Fast Timing System, x2timer." `https://techlab.desy.de/products/amc/x2timer/index_eng.html`, Jan. 2020.

[34] Mini-Circuits, "8 Ways DC Pass Power Splitter, 2000 - 18000 MHz, 50 Ω, ZN8PD-02183-S+." `https://www.minicircuits.com/WebStore/dashboard.html?model=ZN8PD-02183-S%2B`, Feb. 2020.

[35] Mini-Circuits, "Level 17, SMT Double Balanced Mixer, RF/LO Freq 7300-19000 MHz, SIM-193H+." `https://www.minicircuits.com/WebStore/dashboard.html?model=SIM-193H%2B`, Apr. 2018.

[36] Custom MMIC, "6-14 GHz (C,X,Ku Band) High IP3 Double Balanced Mixer, CMD253C3." `https://www.custommmic.com/fundamental-mixer-cmd253c3/`, Apr. 2018.

[37] Mini-Circuits, "Reflectionless Low Pass Filter, DC - 3250 MHz, 50 Ω, XLF-332+." `https://www.minicircuits.com/WebStore/dashboard.html?model=XLF-332%2B`, Mar. 2020.

[38] Wuerth Elektronik, "WE-LPF Multilayer Chip Low-Pass Filter, 748125024." `https://www.we-online.de/katalog/de/WE-LPF/`, Mar. 2020.

[39] American Technical Ceramics, "Broadband Multilayer Capacitor, 530Z." `https://atceramics.com/userFiles/uploads/pdfs/530z.pdf`, Mar. 2020.

[40] Rogers Corporation, "High Frequency Circuit Materials, RO4350B." `https://rogerscorp.com/advanced-connectivity-solutions/ro4000-series-laminates/ro4350b-laminates`, Mar. 2020.

[41] Council of European Parliament, "Council regulation (EU) no 2011/65/EU," 2011.

[42] B. Curran, I. Ndip, and K. Lang, "A comparison of typical surface finishes on the high frequency performances of transmission lines in PCBs," in *2017 IEEE 21st Workshop on Signal and Power Integrity (SPI)*, pp. 1–3, May 2017.

[43] H. Li, C. Ra, G. Zhang, W. J. Yoo, K.-W. Lee, and J.-D. Kim, "Frequency and temperature dependence of the dielectric properties of a PCB substrate for advanced packaging applications," *Journal of the Korean Physical Society*, vol. 54, no. 3, pp. 1096–1099, 2009.

[44] Ansys, "High Frequency Structure Simulator HFSS." `https://www.ansys.com/Products/Electronics/ANSYS-HFSS`, Mar. 2020.

[45] Jyebao, "SMA Jack SQ 12.7mm 4 hole flange with round contact, SMA864NLG-4.05-0.5." `http://www.jyebao.com.tw/upload/SMA864NLG-4.05-0.5.pdf`, Mar. 2020.

[46] Jyebao, "SMA Jack to SMA Jack with 4 hole flange, AD-A8A8-P4L." `http://www.jyebao.com.tw/upload/AD-A8A8-P4L.pdf`, Mar. 2020.

[47] Jyebao, "SMA plug to SMA plug cable, A30A30-141HSA." `http://www.jyebao.com.tw/`, Mar. 2020.

[48] K & L Microwave, "Cavity Filter, 5IR10-12000/T1500-O/OP." `http://www.klfilterwizard.com/klfwpart.aspx?FWS=1012001&PN=5IR10-12000%2fT1500-O%2fOP`, Apr. 2020.

[49] Mini-Circuits, "4 Ways DC Pass Power Splitter, 2000 - 18000 MHz, 50 Ω, ZN4PD-02183-S+." `https://www.minicircuits.com/WebStore/dashboard.html?model=ZN4PD-02183-S%2B`, Apr. 2020.

[50] Mini-Circuits, “3X SMT Multiplier, Output Freq 6600 - 12000 MHz, RMK-3-123+.” https://www.minicircuits.com/WebStore/dashboard.html?model=RMK-3-123%2B, Apr. 2020.

[51] Mini-Circuits, “DC Block, SMA-F, SMA-M, RoHS, BLK-18-S+.” https://www.minicircuits.com/WebStore/dashboard.html?model=BLK-18-S%2B, May 2020.

[52] Telemeter Electronic, “Telepur Festwertfilter, TFWB-K-9G1.05G-SmSf.” https://telemeter.info/de/hf-mikrowellentechnik/hf-filter/telepur-festwertfilter/telepur-bandpassfilter, Apr. 2020.

[53] XP Power, “AC-DC Power Supply, ECL25US15.” https://www.xppower.com/product/ECL05-30-Series, May 2020.

[54] Schaffner, “Multi-stage AC/DC EMI Filter with Excellent Attenuation Performance, FN 2090.” https://www.schaffner.com/product-storage/datasheets/fn-2090/, May 2020.

[55] B. Szczepanski, J. Branlard, S. Chystiakov, M. Fenner, M. Killenberg, D. Kühn, F. Ludwig, F. Makowski, H. Schlarb, N. Shehzad, and G. Varghese, “Redundant and remote manageable power supply concept developed and deployed at the European XFEL,” in *Low Level Radio Frequency Workshop 2019*, 2019.

[56] H. Dinter, M. Czwalinna, C. Gerth, K. Przygoda, R. Rybaniec, H. Schlarb, and C. Sydlo, “Prototype of the Improved Electro-Optical Unit for the Bunch Arrival Time Monitors at FLASH and the European XFEL,” in *37th International Free Electron Laser Conference*, p. TUP049, 2015.

[57] Rohde & Schwarz, “FSWP Phase Noise Analyzer and VCO Tester.” https://www.rohde-schwarz.com/de/produkt/fswp-produkt-startseite_63493-120512.html, Apr. 2020.

[58] Rohde & Schwarz, “SMA100B RF and Microwave Signal Generator.” https://www.rohde-schwarz.com/de/produkt/sma100b-produkt-startseite_63493-427776.html, Apr. 2020.

[59] Rohde & Schwarz, “SMB100A Microwave Signal Generator.” https://www.rohde-schwarz.com/de/produkt/smb100a-produkt-startseite_63493-9379.html, Aug. 2020.

[60] D. Owen, "Good practice guide to phase noise measurement," pp. 21–27, 2004.

[61] Rohde & Schwarz, "Improving R&S FSWP Measurement Speed." https://www.rohde-schwarz.com/appnote/GFM354, Dec. 2020.

[62] R. D'Arcy, "FLASHForward Jitter Studies," *internal report*, 2017.

[63] B. Marchetti, A. Grudiev, P. Craievich, R. Assmann, H.-H. Braun, N. Catalan Lasheras, F. Christie, R. D'Arcy, R. Fortunati, R. Ganter, P. González Caminal, M. Hoffmann, M. Huening, S. M. Jaster-Merz, R. Jonas, F. Marcellini, D. Marx, G. McMonagle, J. Osterhoff, M. Pedrozzi, E. Prat Costa, S. Reiche, M. Reukauff, S. Schreiber, G. Tews, M. Vogt, S. Wesch, and W. Wuensch, "Experimental demonstration of novel beam characterization using a polarizable x-band transverse deflection structure," *Scientific Reports*, vol. 11, p. 3560, Feb 2021.

[64] Microwave Amps, "AM61-12S-60-56PR." https://microwaveamps.co.uk/rf-amplifier/product/8657, Sept. 2020.

[65] Y. Okubo and T. Tanaka, "Development of an X-band 6 MW pulsed klystron," Proceedings of the 11th annual meeting of Particle Accelerator Society of Japan, (Japan), 2014.

[66] J. L. Rodgers and W. A. Nicewander, "Thirteen Ways to Look at the Correlation Coefficient," *The American Statistician*, vol. 42, no. 1, pp. 59–66, 1988.

[67] Z. Farkas, H. Hoag, G. Loew, and P. B. Wilson, "SLED: A Method of Doubling SLAC's Energy.," in *9th International Conference on High-Energy Accelerators*, pp. 576–583, Jan. 1974.

[68] I. Syrachev, "The progress of X-band 'open' cavity RF pulse compression systems," *Conf. Proc. C*, vol. 940627, pp. 375–379, 1995.

[69] R. Zennaro, M. Bopp, A. Citterio, R. Reiser, T. Stapf, *et al.*, "C-band RF pulse compressor for SwissFEL," *Proc. IPAC*, pp. 2827–2829, 2013.

[70] G. Shu, Z. Feng-Li, and H. Xiang, "RF study of a C-band barrel open cavity pulse compressor," *Chinese Physics C*, vol. 39, May 2015.

[71] A. Rezaeizadeh, *Automatic Control Strategies for the Swiss Free Electron Laser*. PhD thesis, ETH Zurich, 2016.

[72] A. Rezaeizadeh, T. Schilcher, and R. Smith, “RF pulse flattening in the SwissFEL facility based on model-free iterative learning control,” in *Proceedings of the 36th International Free Electron Laser Conference (FEL2014)*, pp. 824–827, CERN, 2015.

[73] D. Marx, R. W. Assmann, P. Craievich, K. Floettmann, A. Grudiev, and B. Marchetti, “Simulation studies for characterizing ultrashort bunches using novel polarizable X-band transverse deflection structures,” *Scientific Reports*, vol. 9, no. 1, pp. 1–17, 2019.